Vibration Control Using Switchable Stiffness

by

Thai Tran

A Thesis

Presented to Lakehead University

in Partial Fulfillment of the Requirement for the Degree of

Master of Science

in

Control Engineering

Thunder Bay, Ontario, Canada

2014

Abstract

Over the last decade, the switchable stiffness (SS) control strategy has seen renewed academic interest due to the need for effective vibration control techniques. The SS control strategy involves switching the system's stiffness between at least two distinct states. The system switches to a high stiffness state when the mass is moving away from the equilibrium and a low stiffness state when the mass is moving towards the equilibrium. The SS strategy has been shown to be both theoretically and experimentally effective for shock isolation and residual vibration suppression. The research presented in this thesis investigates the theory and implementation of the SS control.

An experimental apparatus with an electromagnet (EM) actuator as a switchable stiffness spring is presented for the testing and implementation of the SS control. The non-linear dynamics, properties, and parameters are characterized through experimental identification. A detailed analytical dynamic model of the system is derived and verified.

A series of computer simulations reveal the mechanism, stability, and properties of the SS strategy. It is shown that potential energy is dissipated from the system through stiffness reduction. A relationship is developed between the stiffness ratio and the amplitude reduction. The simulations also show a possible instability problem due to time delays. A novel delayed SS strategy, involving the introduction of an intentional delay, is presented to overcome this problem. Simulations verify the effectiveness and limitations of the delayed SS strategy.

The SS control strategy is implemented in real-time. The experiments verify the instability due to time delays and the efficacy of the delayed SS strategies despite the system non-linearities. The performance of the system is, however, shown to be severely limited by the

dynamics of the EM. It is postulated that a SS actuator with low energy input, high stiffness variation, and fast-switching times will enhance the performance significantly.

The SS control strategy for 2DOF systems is investigated. A 2DOF system made up of two SDOF systems coupled by a beam is introduced. The generalized 2DOF system equations and models are derived. Preliminary simulations verify that the direct SS control strategy is effective at suppressing the vibrations of linear and non-linear 2DOF systems. Simulations also show that the delayed SS strategy is effective at suppressing vibrations for symmetrical 2DOF systems with time delays.

Acknowledgements

First and foremost, I would like to thank my supervisor, Dr. Kefu Liu, for his guidance, understanding, patience, and un-relenting encouragement. Thank you for helping me develop myself both personally and academically.

Secondly, I would like to thank all of my professors, technicians, and colleagues at Lakehead University for shaping my academic skills. Specifically, I would like to thank Dr. Xiaoping Liu for his insights, Dr. Wilson Wang for his kindness and power supply, and Mr. Kailash Bhatia for his help in the machine shop, Jerry Zhou for his guidance during my undergraduate NSERC summer, and Gianmarc Coppola for his friendship and academic help. Also, I would like to thank my co-supervisor, Dr. Deli Li, for his kind and generous support.

Thirdly, I would like to thank my friends, family, wife Rachel, and daughter Sophia. In life, we all have a time when our inner fire burns out. I am grateful for everyone who has helped me reignite my spirit, for now it burns stronger than ever.

Table of Contents

List of Figures

List of Tables

List of Acronyms and Symbols

Acronyms

2DOF	2-degree-of-freedom
C.G.	Center of gravity
DAQ	Data acquisition
EM	Electromagnet
EMF	Electromotive force
FFT	Fast Fourier transform
HP	Half period
MB	Mechanical beam
PM	Permanent magnet
PSU	Power supply unit
QP	Quarter period
SC	Steel core
SS	Switchable stiffness
SDOF	Single degree of freedom

Main Symbols

Alphanumeric

c	Damping constant
D	Electromagnet gap distance
E	Total energy
f_{corr}	Correction factor for the loss in permeability of the steel core due to current
f_n	Natural frequency
F_b	Restoring force of the mechanical beam
F_{pe}	Restoring force of the combined steel-core and electromagnet
F_{pf}	Restoring force of the electromagnet
h	Odd numbered multiple
i	Current
k	Stiffness
k_b	Stiffness of the mechanical beam
k_{pe}	Stiffness of the combined steel-core and electromagnet
k_{pf}	Stiffness of the electromagnet
k_v	Back electromotive force constant
l	Length
L	Inductance
m	mass
M	Linear polynomial constant
n	Whole number multiple
N	Non-linear polynomial constant
P	Potential energy
R	Resistance
R_s	Resistance of a 1 ohm power resistor
T	Kinetic Energy
T_n	Natural period
x	The translation coordinate
x_G	The translation coordinate of the 2DOF system at the center of gravity

Greek

α	Stiffness ratio
δ	Logarithmic decrement
Δ	Change
ε	Tolerance limit
ζ	Damping ratio
θ	The rotational coordinate of the 2DOF system at the center of gravity
ω_n	The natural frequency
τ_c	Intentional delay
τ_d	System time delay

Chapter 1 – Introduction

1.1 Vibration Fundamentals

Free mechanical vibration is the natural oscillatory phenomenon of mechanical systems as a result of the interplay between the kinetic and potential energies at the atomic level. Often, excessive vibration can be undesirable; it can cause discomfort to humans via noise and vibration, wear on industrial machinery, damage to sensitive equipment, and, in extreme cases, even destruction of entire civil structures due to wind, earthquakes, or tsunamis. On the other hand, mechanical vibrations can be desirable as well. Examples include music, the means of verbal and auditory communication, base shakers, devices used in medical applications, sorters, or vibratory conveyers for assembly lines [1]. Therefore, the study of vibrations, either the elimination or suppression of undesirable vibrations or the generation of necessary and useful vibrations, is crucial as technology and society becomes more sophisticated. In particular, the study of vibration isolation and control will be examined in detail.

In general, there are two types of vibration isolation problems: (1) displacement transmissibility problem where the vibrational source is in the base and isolation occurs between the base and the mass (2) force transmissibility problem where the vibrational source is in the mass and isolation occurs between the mass and the ground. The former is commonly referred to as base isolation and is concerned with the displacement transmitted from the base to the mass. The latter is concerned with how much force is transmitted from the mass to the ground. A popular example of the case (2) is the rotating unbalance problem [2]. The two systems are shown in Figure 1.1. Standard notations are used throughout; m, k, and c are the mass, stiffness, and damping constant of the system. $x(t)$, $y(t)$, and $F(t)$, are the mass displacement, base excitation, and applied force respectively.

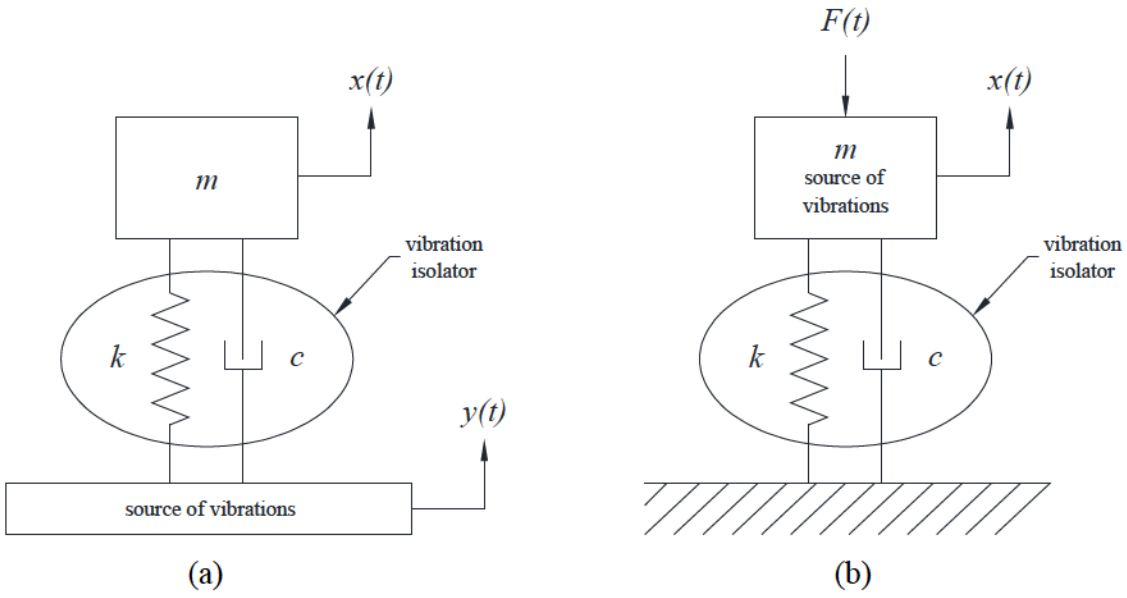

Figure 1.1 Spring mass damper model for (a) displacement transmissibility and (b) force transmissibility

Accompanying these two isolation problems are the concepts of transmissibility. The transmissibility ratio, *TR*, is defined as the ratio of system response amplitude (*X*) to base excitation amplitude (*Y*) for case (a) and the ratio of the transmitted force amplitude (F_T) to the applied force amplitude (F_0) for case (b). The frequency ratio is defined as $r = \omega / \omega_n$ where ω_n is the un-damped natural frequency of the system and is the ω exciting frequency. The damping ratio is defined as $\xi = c / 2\sqrt{km}$. The displacement transmissibility and force transmissibility equations are shown in equations (1.1) and (1.2) respectively.

$$\frac{X}{Y} = \left[\frac{1 + (2\zeta r)^2}{(1 - r^2)^2 + (2\zeta r)^2} \right]^{\frac{1}{2}} \tag{1.1}$$

$$\frac{F_T}{F_0} = \left[\frac{1 + (2\zeta r)^2}{(1 - r^2)^2 + (2\zeta r)^2} \right]^{\frac{1}{2}} \tag{1.2}$$

Equations (1.1) and (1.2) are plotted in Figure 1.2 as a function of the frequency ratio for different damping ratios. Vibration amplification occurs when *TR* is greater than 1. By contrast, when *TR* is less than 1, vibration isolation occurs because the system response amplitude is less than the exciting frequency/force. Therefore, the isolator is said to attenuate vibrations and

belong in the isolation region if $r > \sqrt{2}$ or $\omega > \sqrt{2}\omega_n$. From this concept, it should be noted that a decrease in natural frequency will increase the isolation region [2].

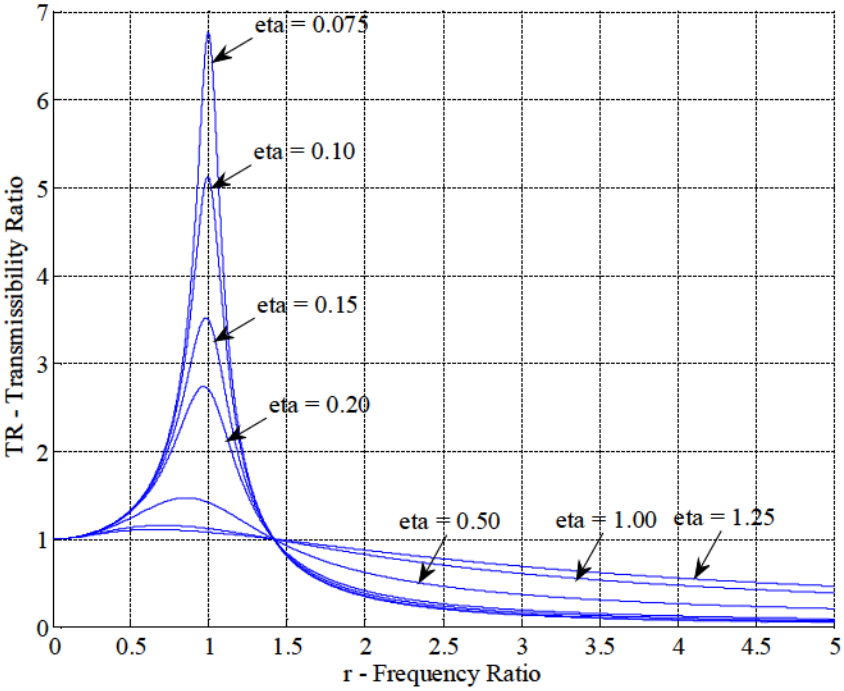

Figure 1.2 Transmissibility plot for different damping ratios

The comparison of the different damping ratios in Figure 1.2 shows that although higher damping is beneficial to the system at resonance, it is less effective at reducing the transmitted force or displacement in the isolation region. Therefore, in general, the performance of the vibration isolator can be improved by decreasing the natural frequency and its damping ratio [3]. Tuning the natural frequency can be accomplished indirectly by changing the system's mass or stiffness although the latter is more practical. A decrease in stiffness decreases the natural frequency but increases the damping ratio and causes a larger static deflection. This method of vibration suppression, by determining these properties, is known as passive vibration isolation and design.

1.2 Vibration Control

As industry and technology develops exponentially to meet consumer demand, anti-vibration technology has become ever more imperative. Commercial buildings, residential

appliances, consumer electronics, or industrial grade machines are constantly subject to shock and vibration. To control these vibrations, there are, in general, three methods based on the required energy input: passive control, active control, and semi-active control. The following subsections will offer a brief overview of these methodologies.

1.2.1 Passive Control

Passive vibration control involves the design and tuning of the system's inherent parameters such as mass, damping, or stiffness to achieve vibration isolation. Tuned mass dampers (TMD), vibration absorbers, and the methods discussed in Section 1.1 are examples of passive vibration control. These methods, by nature, are stable and require minimal energy input.

Unpredictable external disturbances such as high winds or earthquakes implore the urge for passive vibration absorbers, such as TMDs, to be adopted in skyscrapers, power lines, and other civil or mechanical structures. Generally, the TMD is a mass attached to the structure via spring and dashpot in order to absorb the vibrational energy of the primary structure through its relative motion. These absorbers can be seen atop the CN Tower in Toronto, the Millennium Bridge in London, and, the largest TMD, atop the Taipei 101. Through passive control, roughly 40% to 50% reduction in wind-induced response can be achieved [3]. However, the limitation of this method is that it cannot suppress resonant frequencies without more active methods.

Some researchers have used passive control design methods to suppress vibrations in the isolation region in conjunction with active control to suppress vibration at resonance. Zhou [4-5] used passive control methods to optimize the configuration of an electromagnet-permanent magnet spring mass damper assembly. The electromagnets were used in parallel to an existing mechanical spring in order soften the system stiffness. As a result, Zhou was able to successfully create a high static low dynamic stiffness (HSLDS) isolator for passive vibration control in the isolation region. In addition, Zhou uses fuzzy neural network based active controllers to suppress vibrations in the resonance region. Carrella and Kovacic [6-8] also apply different passive control optimizations to the HSLDS isolator using different stiffness configurations to achieve similar results.

1.2.2 Active Control

Without the use of more active control methods, passive vibration control systems, despite its proven merits, are still vulnerable to external disturbances beyond the frequencies of the isolation region. In cases, for example, where the disturbance frequency breaches into the vibration amplification region, there is little that passive control can do to mitigate the disturbance. Even with optimal design, passive control methods have significant limitation in applications where uncertain broadband disturbances are often encountered [8]. Active vibration control methods are able to compensate for these limitations. Active vibration control uses direct control forces to counter the vibrational motion of the system through a control loop of controllers, sensors, and actuators. Typically, there are two ways to construct these loops: open loop and closed loop. Firstly, open-loop (feed forward) control is where the disturbance signal is measured by sensors and fed through a controller which drives the actuators to suppress vibrations [9]. In this case, the relationship between the system model and disturbance should be well known and the disturbance input must be available to the sensor. The second category, closed-loop (feedback) control, is where the system output control variables are measured by the sensors and fed through a controller which drives the actuators to suppress vibrations. This type of active control is often more appropriate in cases where disturbances and parameters are time varying and uncertain. The two types of active control loops are illustrated in Figure 1.3.

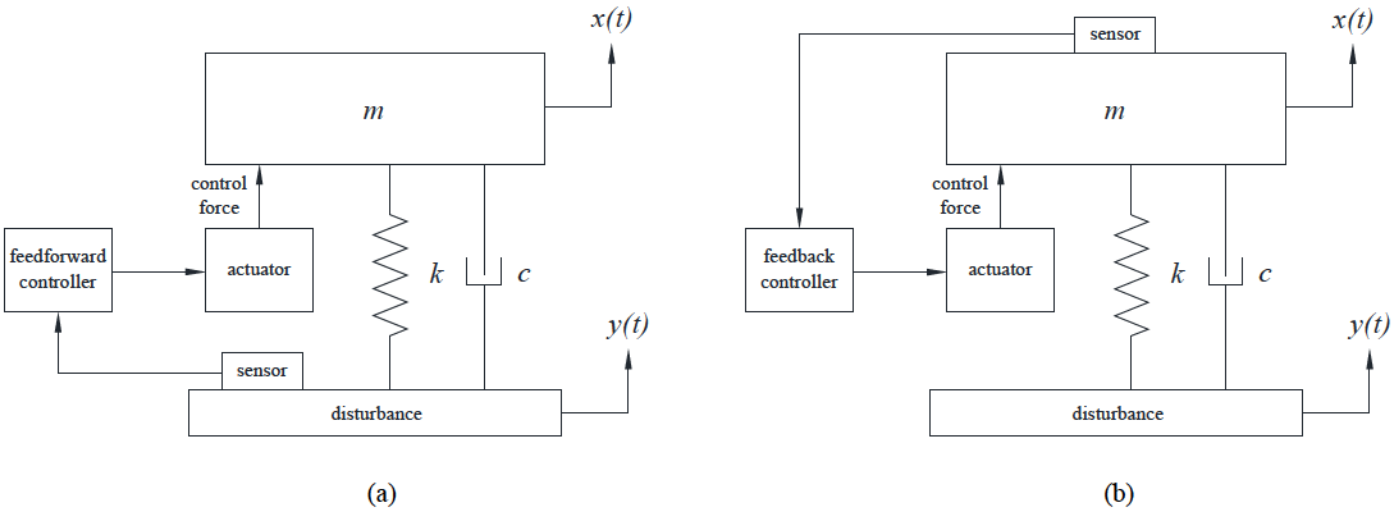

Figure 1.3 Schematic of (a) feed-forward active control (b) feedback active control

Active vibration control is an area of on-going research where novel and innovative ideas are constantly developed. Exponential growth in the development of computers and software has made active control development much more accessible to researchers. Coppola develops [10-11] active control techniques in additional to lag compensation mechanisms. Ji uses adaptive neural fuzzy controller techniques for active vibration suppression of 2DOF flexible structures [12]. Other novel active vibration methods can be seen in [13]. The applications for active-control are extensive. Some examples include active vibration control systems for aircraft, active engine mounts for automobiles, and adaptive vibration control for washing machines.

1.2.3 Semi-Active Control

Semi-active vibration control is achieved by tuning passive parameters such as damping and/or stiffness through a feedback system; it is the combination of both passive and active control. As such, semi-active control takes advantage of the reliability and low power consumption of passive systems with the broadband performance and versatility of active systems. Variable stiffness gives the system the flexibility to navigate the isolation and resonance regions by adapting to the sensor information and variable damping maximizes vibration attenuation whether the system is at resonance or isolation [14, 15]. Some applications of semi-active control include vehicle suspension (skyhook damper) and semi-active control devices for building retrofits.

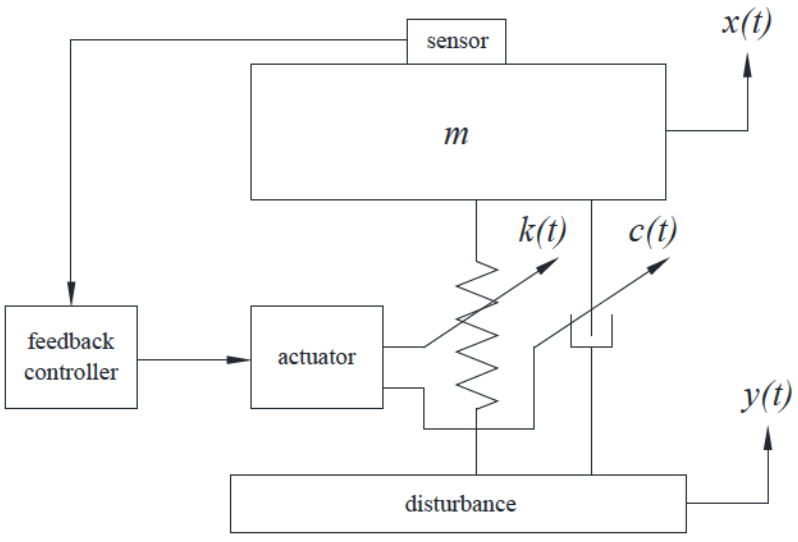

Figure 1.4 Schematic of semi-active feedback control concept

Smart materials can be used in semi-active control to vary the system parameters, in particular, the stiffness. Smart materials are materials with properties that are controllable through external stimuli [16]. For example, magnetorheological fluids (MRF) or magnetorheological elastomers (MRE) can effectively increase its viscosity or stiffness when exposed to a magnetic field. By principle, magnetorheological materials contain polarizable colloidal particles that are sensitive to magnetic stimuli. In sufficiently strong magnetic fields, the particles realign along the magnetic field lines in chains causing changes to effective viscosity or stiffness. Typically, MRFs are used with variable damping and MREs are used with variable stiffness. Although, MRFs used in the damper of a spring mass damper Zener model can change the effective stiffness [17-19]. A relatively new application of MRFs is the MR damper found in semi active control of primary vehicle suspension systems. Additionally, shape memory alloys (SMAs) are another smart structure used semi-active control. SMAs possess two primary states, each with different material properties: a high temperature austenitic state and a low temperature martensitic state. The change from martensitic to austenitic and back to martensitic will restore the SMA shape; this is known as the shape memory effect (SME). When used as actuators in a system, the heating and cooling of the SMAs between these two states allow the stiffness and damping of the overall structure to be tuned [20]. Piezoelectric materials, another smart material, exhibit strain when a voltage is applied. The reverse is also true. When used in a shunted circuit as a piezoelectric actuator, the stiffness of the material can be effectively tuned [21, 22].

1.3 Switchable Stiffness Control

This thesis focuses particularly on a type of variable stiffness semi-active vibration control termed switchable stiffness (SS). The SS control strategy employs the switching between at least two distinct stiffness states depending on the system position and velocity feedback in order to dissipate potential energy from the system. This strategy is able to suppress significant amounts of vibration simply by switching the stiffness [23]. The author is not aware of any other switchable stiffness control algorithm under the same abbreviation.

In the last decade, the SS control strategy has seen renewed interest. The SS concept was first pioneered in 1991 by Onoda [23-25]. Onoda suggested that the system should assume the

high stiffness state when it is moving away from the equilibrium position and a low stiffness state when it is moving towards the equilibrium position. The control law, mechanism, and other details are further elaborated in Section 3.1. Onoda demonstrates effective vibration attenuation of a cantilevered truss structure shown in Figure 1.5 (a). The stiffness switching mechanism was accomplished through a piezoelectric actuator that engaged or disengaged a member of the truss.

In 2002, Jabbari [26] explores the SS control strategy on a MDOF system using a resettable stiffness device. An experimental study was conducted on a 3 story structure using a pneumatic actuator as the resettable stiffness device. The results demonstrate excellent vibration suppression at low energy costs.

More recently, in 2005, a study by Ramaratnam and Jalili explores the SS control using a bi-helical spring with a mechanical arm that engages or disengages the spring coils [27-29] as shown in Figure 1.5 (b). Additionally, this study also introduces the use of an output feedback variable structure velocity observer developed in [30-31] for velocity measurements.

In 2011, Cunefare [32, 33] explored the idea of state switched semi-active vibration absorbers on cantilever beams through piezoelectric actuators. Duerr [34] used the state switched absorber strategy to develop a variable stiffness smart structure capable of mitigating seismic loads. Additionally, Azadi [35] applies the SS strategy to a variable stiffness spring mount made of piezoelectric actuators; the results show significant stiffness change in short times at low energy costs. The mount is shown in Figure 1.5 (c). In the same year, Chatterjee [36] used the inverted SS control to generate self-excited oscillations by parametric excitation [37].

One notable author, Ramirez, extensively explores the SS control for shock and residual vibration isolation [38-42]. This research uses electromagnetic actuators as the switchable stiffness spring as shown in Figure 1.5 (d) which is similar to the apparatus used in this Thesis. The results show effective suppression of shock and residual vibrations. Contrary to [38-42], this Thesis will also explore, in detail, the SS control for systems with significant time delays.

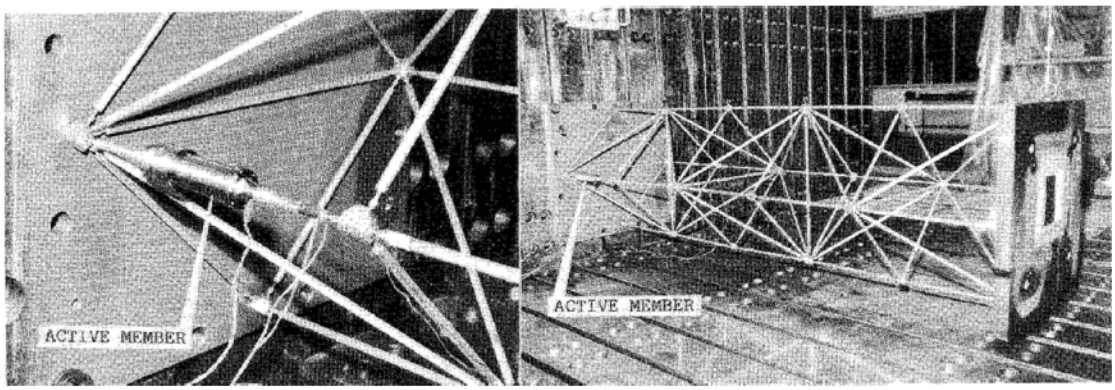

(a)

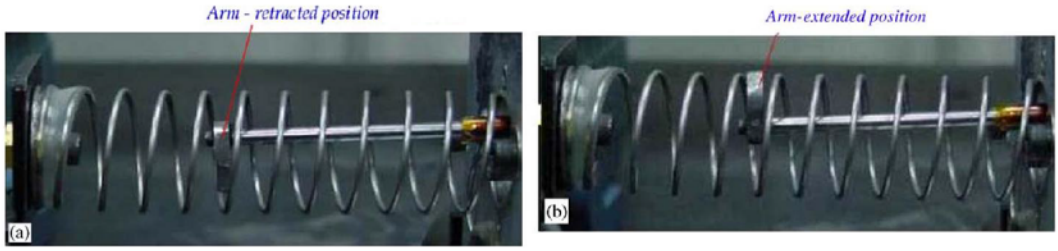

(b)

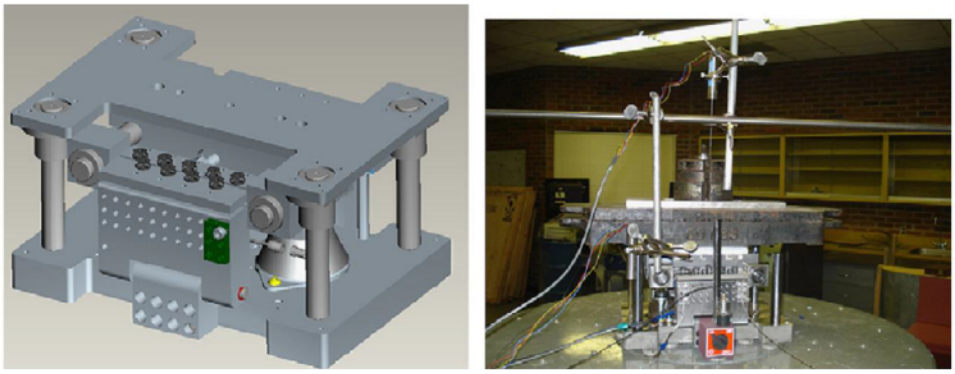

(c)

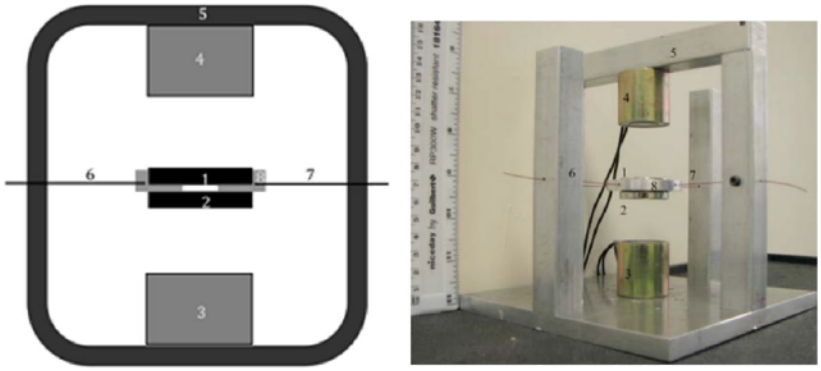

(d)

Figure 1.5 Experimental studies conducted by (a) Onoda [23] (b) Ramaratnam [27] (c) Azadi [35] (d) Ramirez [38]

1.4 Objectives

The main objective of the research in this thesis is to explore and realize the SS control strategy. The specific objectives are as follows:

(1) To characterize the dynamics and properties of the proposed single degree of freedom (SDOF) experimental apparatus through experimental identification.
(2) To explore and validate the control, stability, and mechanism of the SS strategy through simulations.
(3) To explore the effects of inherent time delays and to propose a strategy to overcome these effects.
(4) To explore and evaluate the electromagnets as a switchable stiffness spring.
(5) To explore and validate the SS control strategy through real-time implementation.
(6) To develop and explore the SS control strategy for a 2DOF system.

1.5 Thesis Outline

This thesis is structured in the following manner.

Chapter 2: the SDOF experimental apparatus and dynamic models for the SS control implementation are presented. The dynamic models and system properties are characterized through experimental identification.

Chapter 3: the mechanism, stability, and instability of the SS control strategy are investigated through theory and simulations. The effect of inherent time delays and EM dynamics are also examined. A novel method to overcome time-delays is presented.

Chapter 4: the performance of the SS and time-delay SS control strategies are investigated through real-time experiments.

Chapter 5: a 2DOF model is presented and its equations of motion are derived. Simulations of the SS control on the 2DOF system are presented.

Chapter 6: the conclusions are summarized and future works are discussed.

Chapter 2 – Modeling & Characterization

This chapter deals with the modeling and system characterization of SDOF experimental apparatus used for the testing and development of the switchable stiffness (SS) control strategy. Section 2.1 presents the experimental system components, parameters, and equivalent dynamic model. Sections 2.2 to 2.7 characterize the dynamic models and relevant properties of the system and its components through experimental identification.

2.1 Experimental Apparatus and Dynamic Model

The apparatus used in this study is a SDOF spring-mass system made up of four components labeled in Figure 2.1: the permanent magnet (PM) block (1), the mechanical beam (MB) (2), a set of electromagnets (EM) (3), and a set of steel cores (SC) (4).

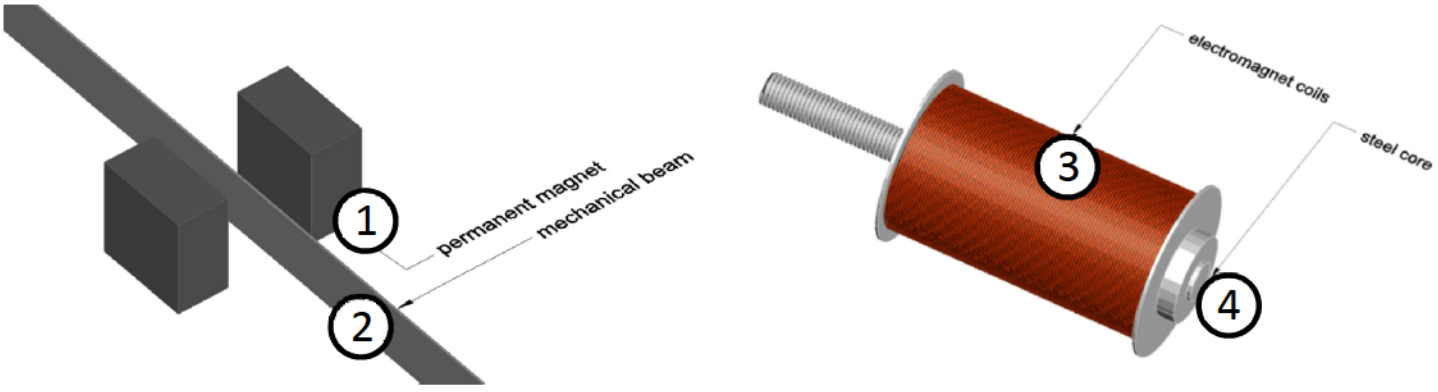

(a) (b)

Figure 2.1 (a) PM (1) and MB (2) (b) EM (3) and SC (4)

The assembly of the system is shown in Figure 2.2. The PM block (1) acts as the system mass. It is made up of two neodymium magnets clamped together at the center of the MB (2) by its own magnetic force. The MB is a stainless steel ruler fixed at both ends to the rigid frame (5) via nuts and bolts. The tension of the MB can be adjusted by turning the bolts at the ends (6). The fixed-fixed MB acts as a mechanical (PM-MB) spring laterally. The EMs (3) are placed in line with the PM block with their polarities setup to repel the PM. The EM cores, referred as the steel cores (SC) (4), are low carbon steel rods. The core extensions are threaded and fastened to the rigid frame. The gap distance between the EMs can be adjusted by sliding the core extensions through the holes in the rigid frame. The interaction between the EMs and PM block constitutes two springs: the magnetic (PM-SC) spring and the electromagnetic (PM-EM) spring. The PM-SC spring is due to the magnetic attraction between the PM and SCs. The PM-EM spring occurs when the EMs are energized. Table 2.1 lists the dimensions and parameters of the system components.

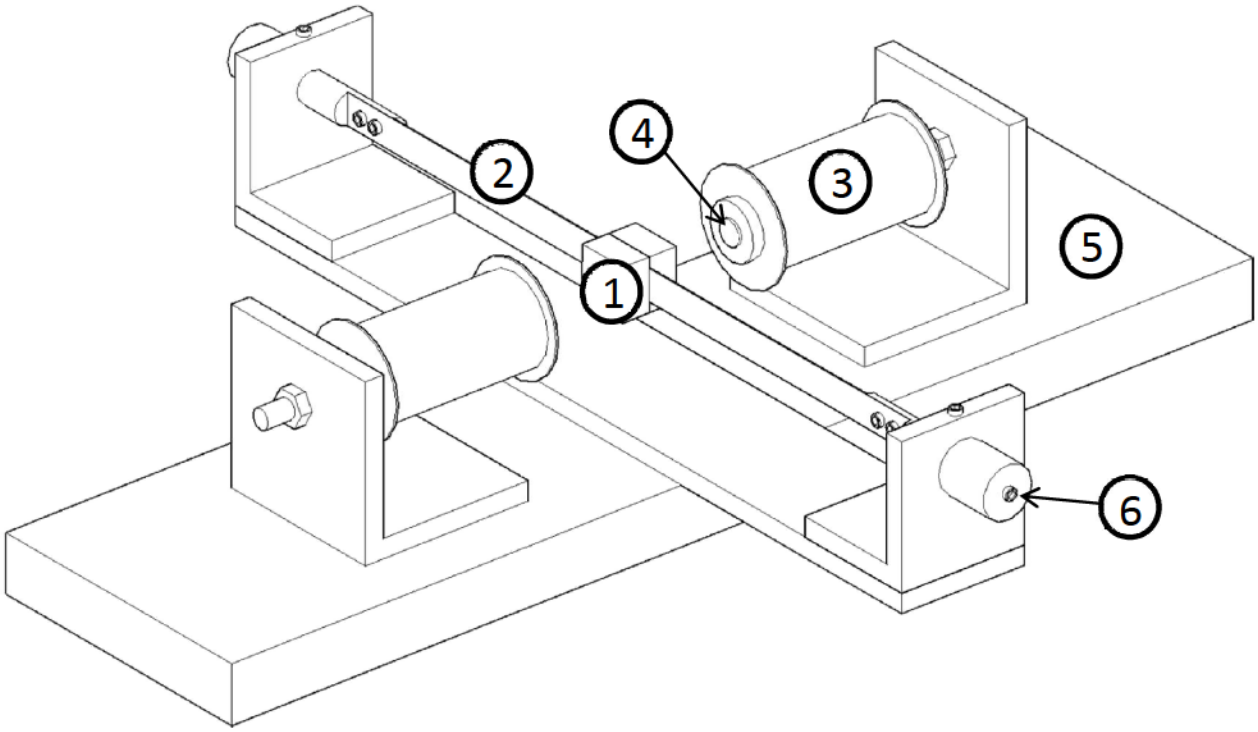

Figure 2.2 CAD model of experimental apparatus

Table 2.1 System Parameters

Symbol	Description	Value
Permanent Magnet (PM)		
l_{pm}	Length of PM	25.4 mm
w_{pm}	Width of PM	25.4 mm
h_{pm}	Height of PM	29.0 mm
m	Mass of the PM	0.13 kg
Mechanical Beam (MB)		
l_b	Length of MB	380.0 mm
w_b	Width of PM	0.5 mm
h_b	Height of PM	16.0 mm
Electromagnet (EM) Set A		
r_{iA}	Inner radius of EM coils	6.5 mm
r_{oA}	Outer radius of EM coils	23.3mm
l_{EMA}	Length of EM coils	88.0 mm
l_{SCA}	Length of steel cores	15.0 cm
d_{22}	Diameter of the EM gauge 22 coil wire	0.69 mm
N_A	Number of turns of the EM coils	3565
R_A	Resistance of the EM coil	13.0 Ω
Electromagnet (EM) Set B		
r_{iB}	Inner radius of EM coils	13.5 mm
r_{oB}	Outer radius of EM coils	27.0 mm
l_{EMB}	Length of EM coils	60 mm
l_{SCB}	Length of steel cores	16.0 cm
d_{22}	Diameter of the EM gauge 22 coil wire	0.69 mm
N_B	Number of turns of the EM coils	1210
R_B	Resistance of the EM coil	8.2 Ω

Figure 2.3 represents the dynamic force model and equivalent stiffness model of the experimental system. The mass of the system is denoted as m. The symbols F_{pc}, F_{pf}, and F_b represent the magnetic (PM-SC) force, the electromagnetic (PM-EM) force, and the MB restoring (PM-MB) force, respectively. These forces are functions of displacement and, thus, can be modeled as the forces of three non-linear springs in parallel [43]. The stiffness of the mechanical spring, magnetic spring, and electromagnetic spring are denoted as k_b, k_{pc}, and k_{pf} respectively. Also, the stiffness of the combined electromagnetic (PM-SC-EM) spring and the combined total system spring (PM-MB-SC-EM) are denoted as k_{pe} and k_t respectively. F_d represents the system damping force due to internal friction forces of the MB. For simplicity, the damping due to the induced back electromotive force (back EMF) of the EMs [44] and other forms of non-linear damping are not considered. Non-linear damping is a topic for future work and is beyond the scope of this Thesis. In this system, damping is modeled as viscous (directly proportional to the mass's velocity) with the damping constant denoted as c. The focus of the following sections is to identify these dynamic properties.

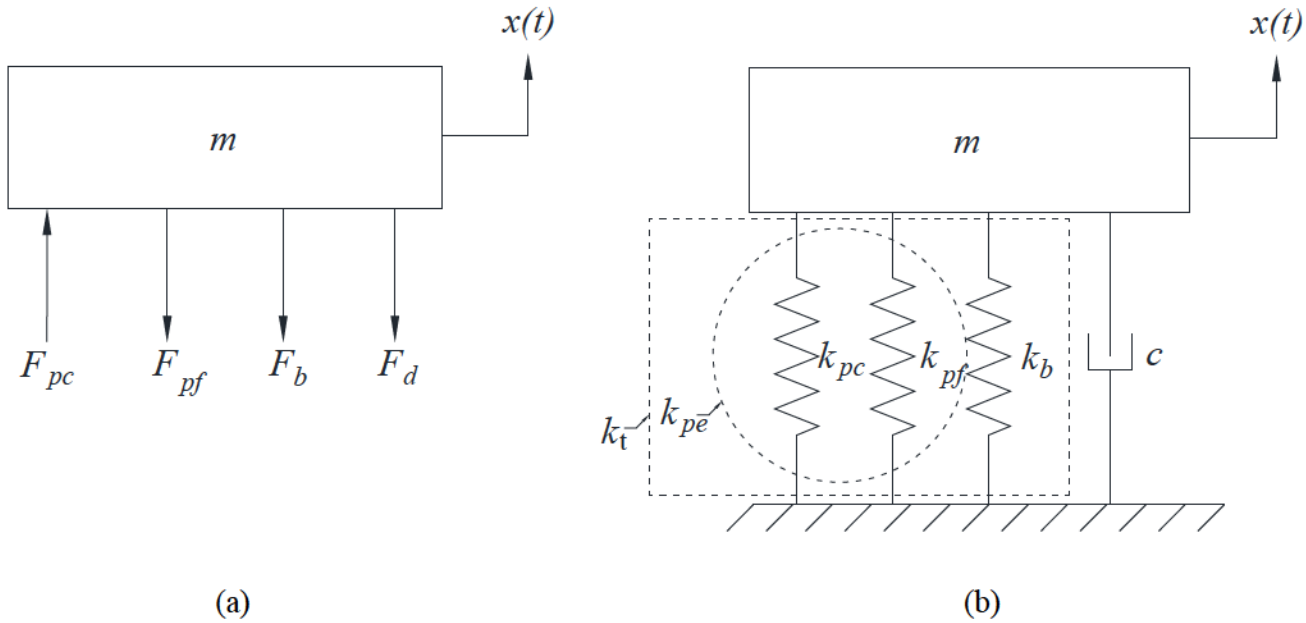

Figure 2.3 (a) combined system free body diagram (b) combined system equivalent stiffness and damping model

2.2 Characterization of the Mechanical Spring

The mechanical spring was characterized through two experiments: the force-displacement experiment and the free response experiment. From the force-displacement relationship, the restoring force of the MB was determined. From the free response experiment, the damping and natural frequency were determined. Two different MB tension cases were considered: case 1 – low tension and case 2 – medium tension.

2.2.1 Dynamic Model of the Mechanical Spring

The MB imparts a restoring force that opposes the displacement of the PM block. This dynamic restoring force can be modeled as a cubic polynomial:

$$F_b = c_1 x^3 + c_2 x \tag{2.1}$$

where F_b is the MB restoring force, x is the mass displacement, and c_1 and c_2 are the polynomial fitting constants. Note that the quadratic and constant term was omitted from equation (2.1) based on two assumptions: the MB has no lateral pre-bending and the beam is symmetrical about the equilibrium position (when $x = 0$). The stiffness model, k_b, was determined by differentiating equation (2.1) with respect to x [45]. The MB stiffness equation is shown in equation (2.2).

$$k_b = \frac{\mathrm{d}F_b}{\mathrm{d}x} = 3c_1 x^2 + c_2 \tag{2.2}$$

The stiffness model of the MB constitutes two parts: a linear term characterized by c_2, and a non-linear term characterized by c_1. The linear force is directly proportional to the displacement of the PM block; this linear relationship is known as Hooke's Law. When the force is differentiated with respect to the displacement, as shown in equation (2.2), c_2 becomes the linear stiffness of the system at equilibrium. The non-linear coefficient, c_1, introduces a stiffness variation when the system is not at equilibrium. In some cases where the displacement is sufficiently small, the non-linear term may be neglected.

2.2.2 Experimental Identification of the Mechanical Spring

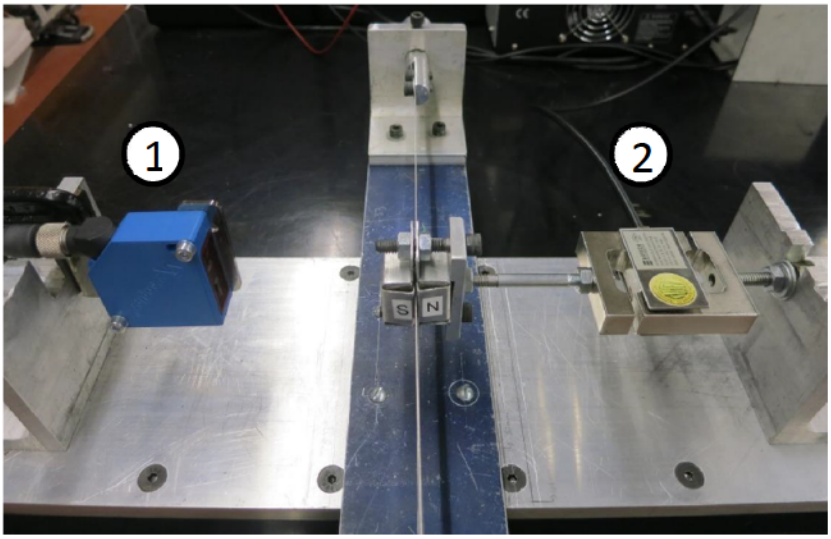

Figure 2.4 MB force-displacement experiment with (1) position sensor and (2) force sensor

A force-displacement experiment, as shown in Figure 2.4, was conducted to identify the constants in equation (2.1). The PM block was attached to a force sensor (2) through a rigid rod. The other end of the force sensor is threaded and was attached on the rigid frame through a set of bolts. The force applied to the PM block was varied by sliding the force sensor through the rigid frame via the bolts. The displacement was measured by the laser reflex sensor (1) while the corresponding force was measured by the force sensor. The data was collected by a data acquisition (DAQ) board (dSpace 1102). Control Desk (dSpace) and Matlab Simulink were used to interface the experiment. This experiment was executed for the two different MB tension cases. Matlab's least-squares based polynomial fitting function, '*polyfit*', was used to curve fit equation (2.1) with the experimental data. Figure 2.5 plots the analytical equation (2.1) with the experimental data. The fitting constants are listed in Table 2.2 for each tension case. In general, it is observed that increasing the MB tension has a twofold effect: it directly increases the linear stiffness (c_2 term) and slightly increases the non-linearity of the spring (c_1 term).

Table 2.2 MB fitting constants

Case	c_1	c_2
1 - Low tension	2.706×10^7	0.915×10^3
2 - Medium tension	2.878×10^7	1.647×10^3

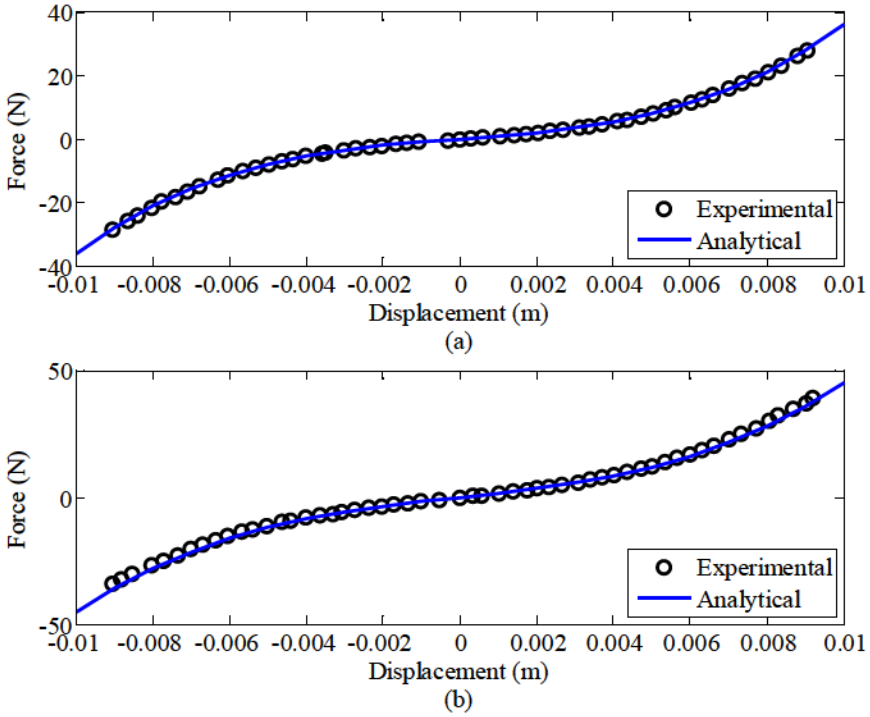

Figure 2.5 The MB force vs. PM block displacement: experimental results and the best fit curve by equation (2.2): (a) case 1 – low tension (b) case 2 – medium tension

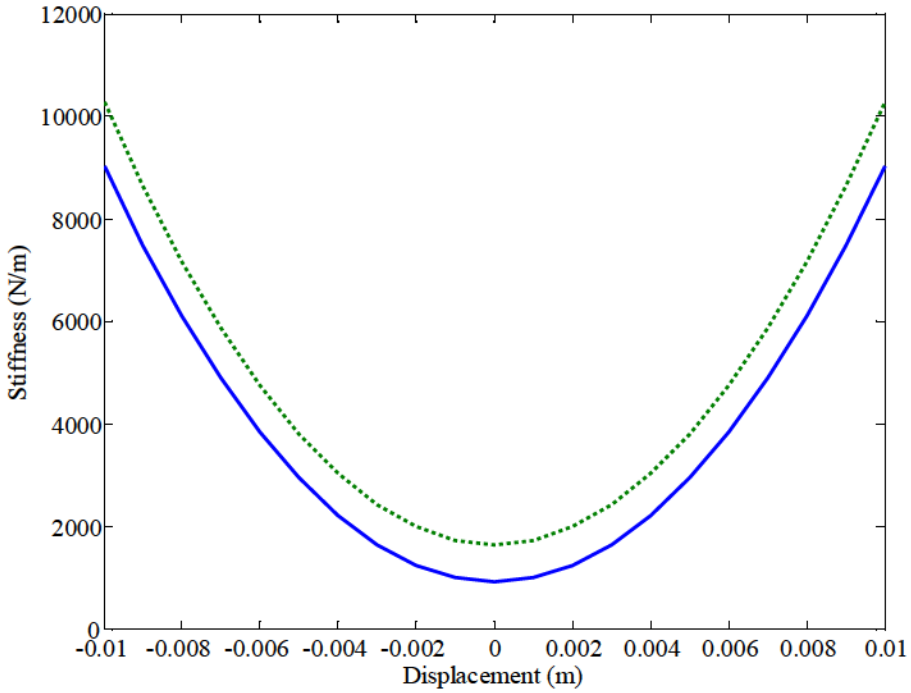

Figure 2.6 Stiffness of the MB: case 1 – blue solid line, case 2 – green dashed line

2.2.3 Natural Frequency and Damping of the Mechanical Spring

A free response experiment, as shown in Figure 2.7, was conducted to determine the natural frequency and damping characteristics of the mechanical spring. Free vibration of the system was induced by tapping the PM block. The free responses were measured by the laser reflex sensor. The signal from the sensor was collected by the DAQ system. Control Desk and Matlab Simulink were used to interface the experiment.

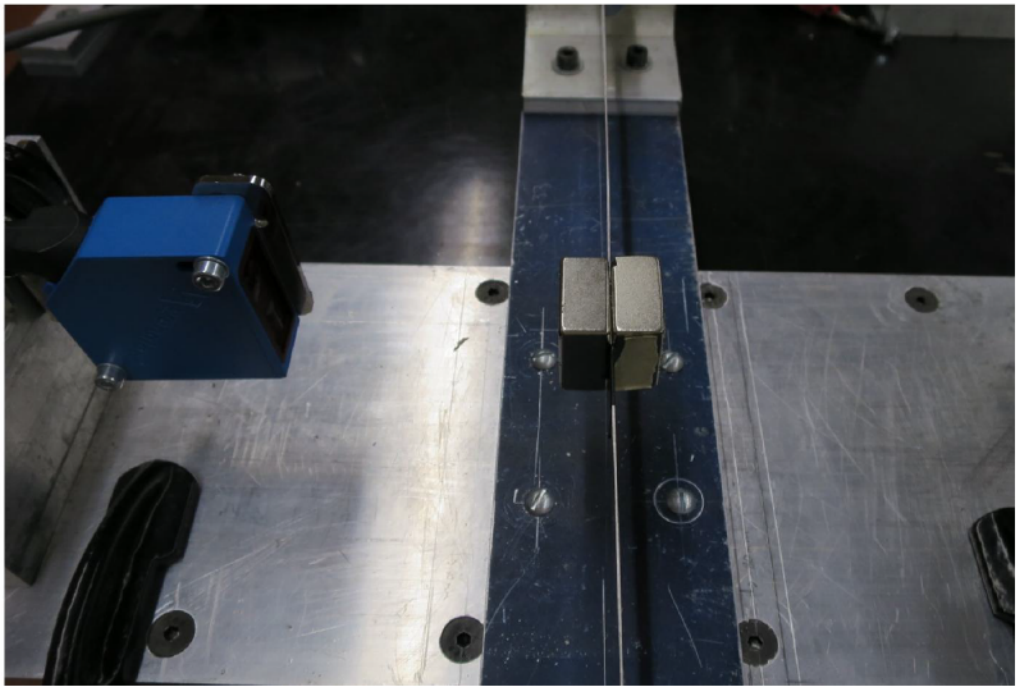

Figure 2.7 MB free response experiment

Figure 2.8 shows a typical unfiltered free response signal for each of the two cases. Applying Matlab's built in fast Fourier transform (FFT) function, '*fft*', to the free response data, the natural frequency of the system was found for each case. The natural frequency of each case can be identified from the FFT peaks shown in Figure 2.9. As expected, an increase in the MB tension will result in an increase in the natural frequency of the system.

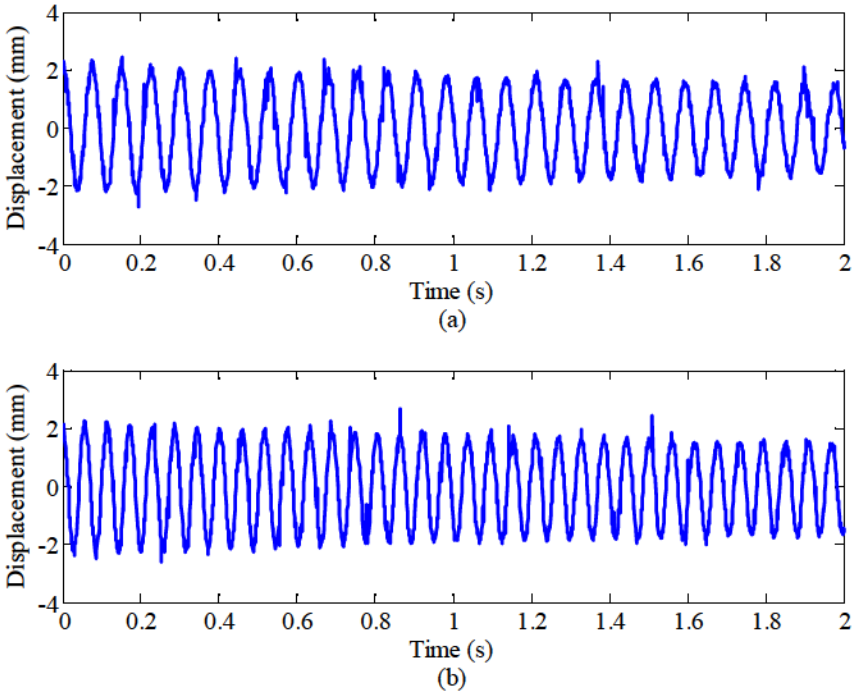

Figure 2.8 System free response: (a) case 1 – low tension (b) case 2 – medium tension

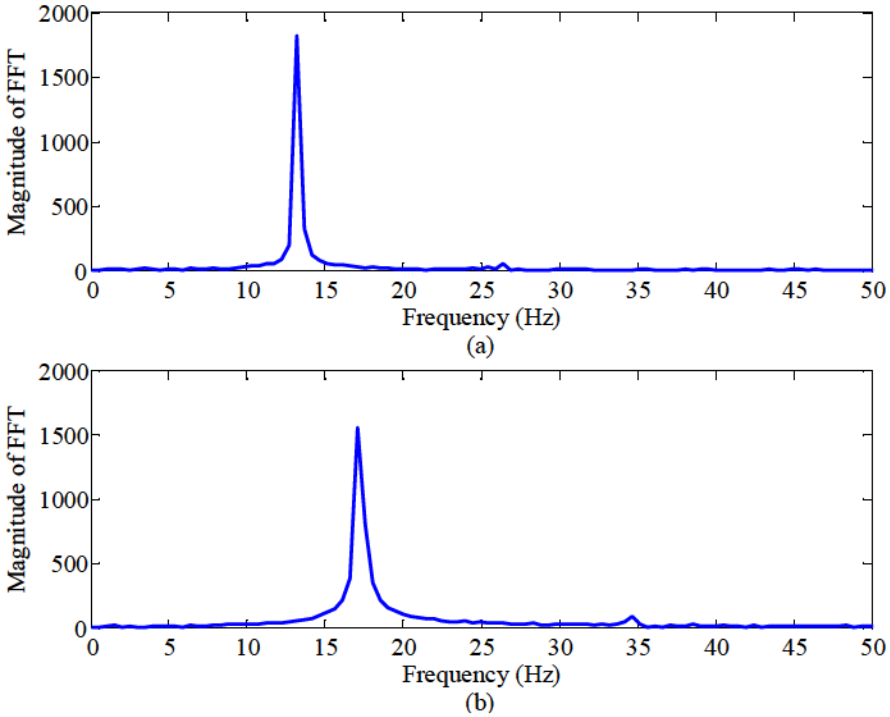

Figure 2.9 FFT magnitude of the system free response: (a) case 1 – low tension, (b) case 2 – medium tension

The natural frequency of the PM block and mechanical spring system can be determined using the equation

$$\omega_n = \sqrt{\frac{k}{m}} \tag{2.3}$$

where ω_n is the natural frequency, m is the mass, and k is the linear stiffness. Note that equation (2.3) is only valid for a linear stiffness. In order to use equation (2.3), equation (2.2) is linearized about the equilibrium position using the small displacement approximation ($x \cong 0$). The linearized MB stiffness model is shown in equation (2.4).

$$k = c_2 \tag{2.4}$$

Table 2.3 lists the natural frequencies identified from the free response experiment and calculated from equation (2.3) for the two MB tension cases. In general, the analytical and experimental natural frequencies show good agreement with small discrepancies.

Table 2.3 Natural frequencies of the mechanical spring

Case	**Experimental ω_n (Hz)**	**Analytical ω_n (Hz)**
1 – Low tension	13.18	13.35
2 – Medium tension	17.09	17.91

The damping ratio of the PM block and MB system was estimated by applying the logarithmic decrement method [2] to the free response data in Figure 2.8. The logarithmic decrement is given by

$$\delta = \frac{1}{n} ln \frac{x(t)}{x(t+nT)} \tag{2.5}$$

where $x(t)$ is the first displacement point, $x(t+nT)$ is the second displacement point, T is the period, and n is the number of periods between the first and second displacement points. The amplitude peaks were chosen as displacement points. Several sets of displacement peaks were

chosen to mitigate the effect of noise. The damping ratio was calculated using equation (2.6) and the damping coefficient was estimated using equation (2.7) with the experimental ω_n values.

$$\zeta = \frac{1}{\sqrt{1+\left(\frac{2\pi}{\delta}\right)^2}} \tag{2.6}$$

$$c = 2\zeta m\omega_n \tag{2.7}$$

$$\zeta = \frac{c}{2\sqrt{km}} \tag{2.8}$$

Table 2.4 lists the damping ratio and damping constant for each MB tension case. The results show that higher MB tension corresponds to slightly lower damping. This observation is consistent with the relationship between damping and stiffness shown in equation (2.8). In addition, the overall damping values of the system are very low. Therefore, the system's damped natural frequency can be approximated as the natural frequency $(\omega_d \cong \omega_n)$.

Table 2.4 Experimental damping ratio for three initial beam tension cases

Case	Damping Ratio	Damping Constant
1 – Low tension	0.001822	0.03923
2 – Medium tension	0.001759	0.04910

2.3 Characterization of the Magnetic Spring

2.3.1 Dynamic Model of the Magnetic Spring

There is a magnetic attraction force between the PM and the SC due to the magnetization of the PM and the iron content of the SC. Inspired by Coulomb's law [46], this magnetic force is assumed to be

$$F_{pc} = \frac{a_1}{(d + a_2)^4} \tag{2.9}$$

where F_{pc} is the attracting force and d is the air gap distance between the surface of the PM and surface of the SC. a_1 and a_2 are the fitting constants to be determined.

Figure 2.10 illustrates the forces of the SC on the PM where F_{pc1} is the force of SC_1 on the PM's south pole and F_{pc2} is the force of SC_2 on the PM's north pole. D is the gap distance between the two EM surfaces and h is the thickness of the PM block. The PM block's equilibrium position ($x = 0$) is centered between the two SCs.

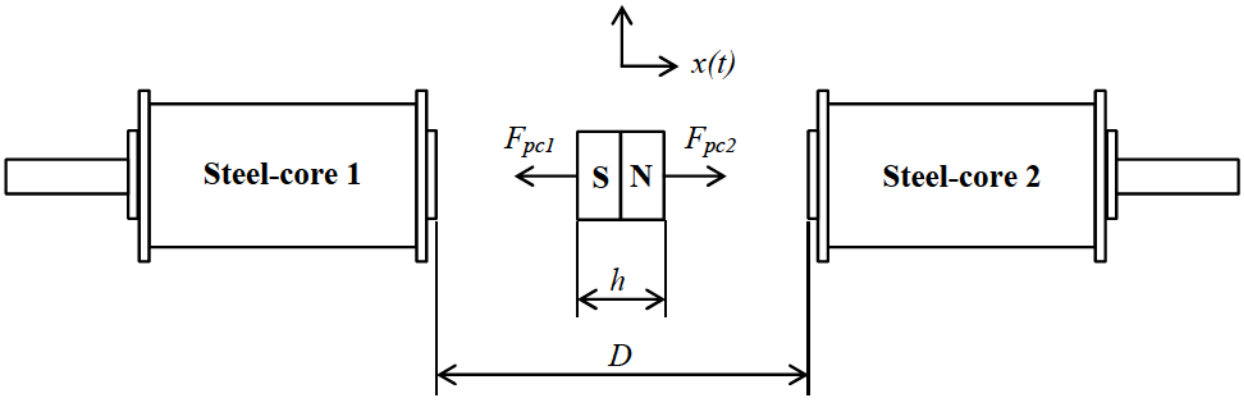

Figure 2.10 PM-SC interaction

Based on equation (2.9) and Figure 2.10, F_{pc1} and F_{pc2} are defined as:

$$F_{pc1} = \frac{a_{11}}{\left(d_1 + a_{21}\right)^4} \tag{2.10}$$

$$F_{pc2} = \frac{a_{12}}{\left(d_2 + a_{22}\right)^4} \tag{2.11}$$

where d_1 and d_2 are the distances between the surfaces of the respective SCs and PM. Without loss of generality, d_1 and d_2 can be transformed in terms of the x coordinate.

$$d_1 = \frac{D-h}{2} + x \tag{2.12}$$

$$d_2 = \frac{D-h}{2} - x \tag{2.13}$$

The net force acting on the PM block is

$$\Delta F_{pc} = F_{pc2} - F_{pc1} = \frac{a_{12}}{\left(q_{12} - x\right)^4} - \frac{a_{11}}{\left(q_{11} + x\right)^4} \tag{2.14}$$

where q_{11} and q_{12} are defined as

$$q_{11} = \frac{D-h}{2} + a_{21} \tag{2.15}$$

$$q_{12} = \frac{D-h}{2} + a_{22} \tag{2.16}$$

The net force in equation (2.14) can be considered as a restoring force exerted by the magnetic spring. Note that Hooke's requires a negative sign if the force is a restoring force. Therefore, differentiating equation (2.14) with respect to displacement and applying Hooke's law sign convention yields the stiffness of the PM-SC spring:

$$k_{pc} = -\frac{\mathrm{d}\Delta F_{pc}}{\mathrm{d}x} = -4\left[\frac{a_{12}}{(q_{12}-x)^5} + \frac{a_{11}}{(q_{11}+x)^5}\right] \tag{2.17}$$

In the special case where both steel cores are identical, the constants can be further simplified to

$$\begin{aligned} a_1 &= a_{11} = a_{12} \\ a_2 &= a_{21} = a_{22} \\ q_1 &= q_{11} = q_{12} = \frac{D-h}{2} + a_2 \end{aligned} \tag{2.18}$$

and, thus, the stiffness and force equations can be simplified to

$$\Delta F_{pc} = 8a_1q_1\frac{x\left(q_1^{\,2}+x^2\right)}{\left(q_1^{\,2}-x^2\right)^4} \tag{2.19}$$

$$k_{pc} = -8a_1q_1\frac{\left(5x^4+10q_1^2x^2+q_1^4\right)}{\left(q_1^{\,2}-x^2\right)^5} \tag{2.20}$$

2.3.2 Experimental Identification of the Magnetic Spring

An experiment was conducted to find the curve fitting constants, a_{11}, a_{12}, a_{21}, and a_{22} in equations (2.14). Figure 2.11 shows the experimental setup. The clamped PM-MB assembly was detached from the rigid frame and attached to the force sensor (1) by the PM's own magnetic force. The MB was intentionally left between the magnet halves to include the influence of the MB on the magnetic flux. The distance between the PM and SC (2) was varied incrementally and the corresponding magnetic attraction force was measured by the force sensor. The distance between the PM and SC was measured by a micro-caliper. The experiment was done for SC_1 facing the south pole of the PM and SC_2 facing the north pole of the PM.

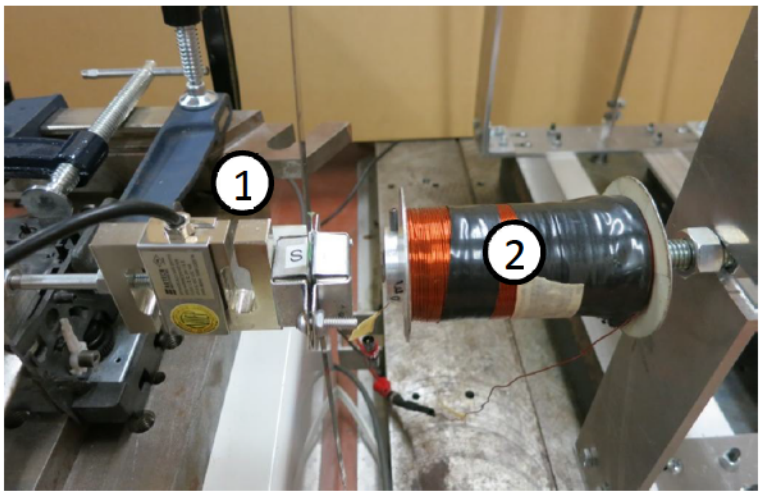

Figure 2.11 SC attraction force-displacement experiment

The sequential simplex algorithm [4,47] was used to curve-fit the experimental data with equations (2.10) and (2.11). Table 2.5 lists the obtained constants and Figure 2.12 compares the experimental and analytical results. The data strongly confirms that SCs are identical. For simplicity, equation (2.18) is applied for both SCs. The average of each fitting constant between the two SCs is calculated and denoted a_1 and a_2 in accordance to equation (2.18).

Table 2.5 Experimental fitting constants for equation (2.10) and (2.11)

Constants	**EM_1**	**EM_2**	**$EM_{average}$**
a_1 (10^{-6})	4.145	4.227	4.186
a_2 (10^{-2})	1.312	1.344	1.328

Figure 2.13 shows the magnetic spring stiffness determined by equation (2.20) for 60, 70, 80, and 90 mm SC gap distances. The negative parabolic-like curves indicate that the magnetic spring has a negative stiffness; when placed in parallel within the system, this spring will reduce the overall stiffness of the total system. For smaller SC gap distances, the non-linearity and softening effects are much stronger.

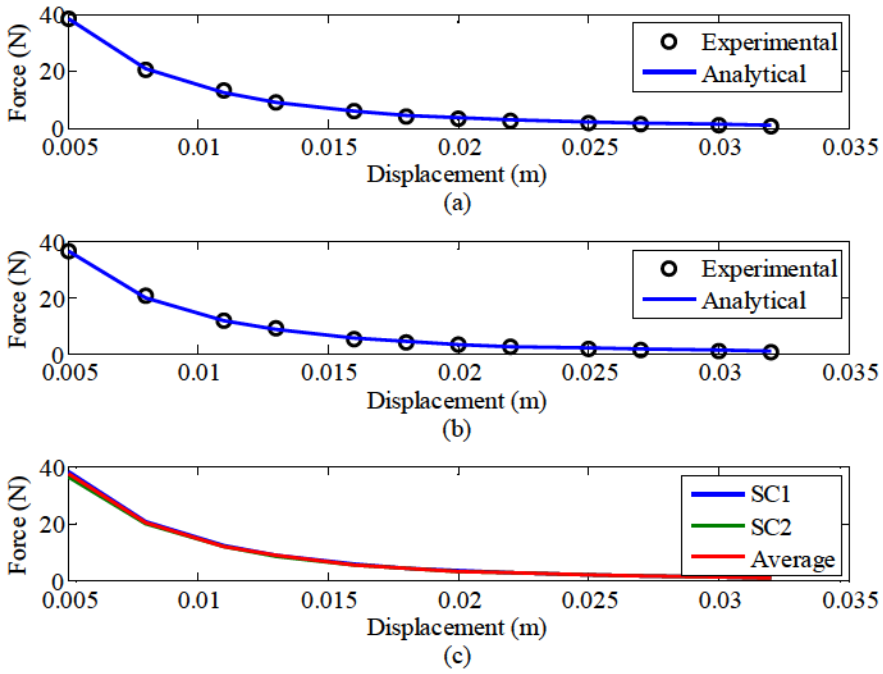

Figure 2.12 The SC attracting force for (a) F_{pc1} of SC_1 on PM south (b) F_{pc2} of SC_2 on PM north (c) average of F_{pc1} and F_{pc2}

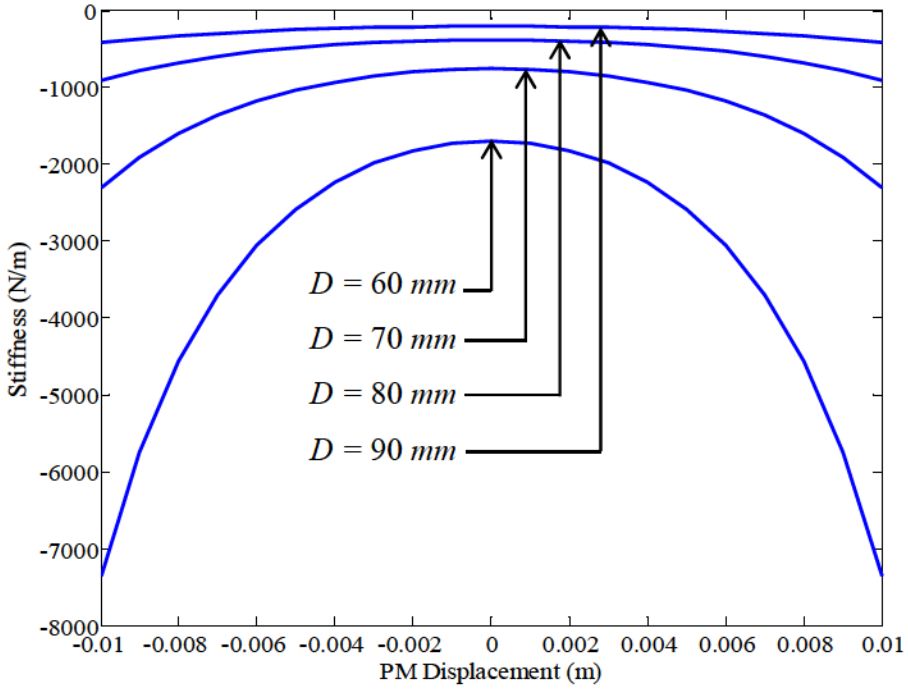

Figure 2.13 Analytical dynamic stiffness model of the PM-SC spring for different SC gap distances

2.4 Characterization of the Combined Electromagnetic Spring

2.4.1 Dynamic Model of the Combined Electromagnetic Spring

The electromagnetic force of the EM on the PM block, F_{pf}, results from energizing the EMs with current. This force can be modeled as [4]

$$F_{pf} = sgn(i)\left(1 - e^{-b_3|i|}\right)\frac{b_1}{(d + b_2)^4} \tag{2.21}$$

where sgn is the sign function, i is the EM current, and d is the distance between the surfaces of the PM and EM. b_1, b_2, and b_3 are the fitting constants to be determined.

As the SC is permanently fixed to the EM, it is more realistic to experimentally characterize the combined electromagnetic force of the PM-SC-EM. Therefore, the combined electromagnetic force, F_{pe}, is modeled as

$$F_{pe} = f_{corr}F_{pc} + F_{pf} \tag{2.22}$$

where f_{corr} is defined as

$$f_{corr} = 1 - a_3|i| \tag{2.23}$$

Increasing the current magnitude in the EM reduces the relative permeability of the SC, thereby reducing the effective PM-SC force, F_{pc} [48]. f_{corr} is introduced in equation (2.22) to model this effect. Thus, the combined electromagnetic force equation is given as

$$F_{pe} = \left(1 - a_3|i|\right)F_{pc} - sgn(i)\left(1 - e^{-b_3|i|}\right)\frac{b_1}{(d + b_2)^4} \tag{2.24}$$

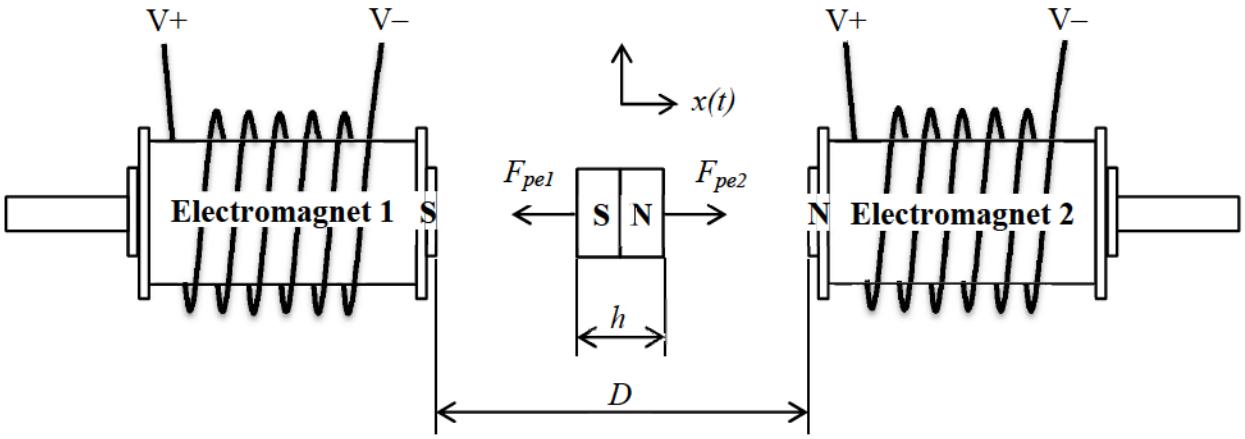

Figure 2.14 PM-EM interaction

Figure 2.14 illustrates the combined EM-SC forces on the PM block. F_{pe1} is the force of EM_1-SC_1 on the PM's south pole and F_{pe2} is the force of EM_2-SC_2 on the PM's north pole. D is the gap distance between the two EM surfaces and h is the width of the PM block. The PM block's equilibrium position ($x = 0$) is centered between the two EMs. Based on equation (2.21), F_{pe1} and F_{pe2} are defined as:

$$F_{pe1} = \left(1 - a_{31}|i_1|\right) F_{pc1} - sgn(i_1)\left(1 - e^{-b_{31}|i_1|}\right) \frac{b_{11}}{\left(d_1 + b_{21}\right)^4} \tag{2.25}$$

$$F_{pe2} = \left(1 - a_{32}|i_2|\right) F_{pc2} - sgn(i_2)\left(1 - e^{-b_{32}|i_2|}\right) \frac{b_{12}}{\left(d_2 + b_{22}\right)^4} \tag{2.26}$$

where d_1 and d_2 are the distances between the surfaces of the respective EMs and PM. Without loss of generality, d_1 and d_2 can be transformed in terms of the x coordinate:

$$d_1 = \frac{D - h}{2} + x \tag{2.27}$$

$$d_2 = \frac{D - h}{2} - x \tag{2.28}$$

The net force on the PM block is

$$\begin{aligned}\Delta F_{pe} &= F_{pe2} - F_{pe1} \\ &= \left(1 - a_{32}\left|i_2\right|\right)\frac{a_{12}}{\left(q_{12} - x\right)^4} - sgn\left(i_2\right)\left(1 - e^{-b_{32}\left|i_2\right|}\right)\frac{b_{12}}{\left(d_2 + b_{22}\right)^4} \\ &- \left(1 - a_{31}\left|i_1\right|\right)\frac{a_{11}}{\left(q_{11} + x\right)^4} + sgn\left(i_1\right)\left(1 - e^{-b_{31}\left|i_1\right|}\right)\frac{b_{11}}{\left(d_1 + b_{21}\right)^4}\end{aligned} \tag{2.29}$$

where q_{21} and q_{22} are defined as:

$$q_{21} = \frac{D - h}{2} + b_{21} \tag{2.30}$$

$$q_{22} = \frac{D - h}{2} + b_{22} \tag{2.31}$$

Differentiating equation (2.29) with respect to displacement and applying Hooke's law sign convention yields the stiffness of the PM-SC-EM spring:

$$\begin{aligned}k_{pe} = -\frac{\mathrm{d}\Delta F_{pe}}{\mathrm{d}x} &= -4\left[\left(1 - a_{31}\left|i_1\right|\right)\frac{a_{11}}{\left(q_{11} + x\right)^5} + \left(1 - a_{32}\left|i_2\right|\right)\frac{a_{12}}{\left(q_{12} - x\right)^5}\right] \\ &+ 4\left[sgn\left(i_2\right)\left(1 - e^{-b_{32}\left|i_2\right|}\right)\frac{b_{12}}{\left(q_{22} - x\right)^5} + sgn\left(i_1\right)\left(1 - e^{-b_{31}\left|i_1\right|}\right)\frac{b_{11}}{\left(q_{21} + x\right)^5}\right]\end{aligned} \tag{2.32}$$

In the special case where the EM current is the same ($i = i_1 = i_2$), equation (2.32) becomes

$$\begin{aligned}k_{pe} &= -4\left[\left(1 - a_{32}\left|i\right|\right)\frac{a_{12}}{\left(q_{12} - x\right)^5} + \left(1 - a_{31}\left|i\right|\right)\frac{a_{11}}{\left(q_{11} + x\right)^5}\right] \\ &+ 4sgn\left(i\right)\left[\left(1 - e^{-b_{32}\left|i\right|}\right)\frac{b_{12}}{\left(q_{22} - x\right)^5} + \left(1 - e^{-b_{31}\left|i\right|}\right)\frac{b_{11}}{\left(q_{21} + x\right)^5}\right]\end{aligned} \tag{2.33}$$

In the special case where the EMs are identical, the constants can be simplified to

$$\begin{aligned} b_1 &= b_{11} = b_{12} \\ b_2 &= b_{21} = b_{22} \\ a_3 &= a_{31} = a_{32} \\ q_2 &= q_{21} = q_{22} \end{aligned} \tag{2.34}$$

and equation (2.32) becomes

$$\begin{aligned} k_{pe} = -4a_1 &\left[\frac{\left(1-a_3|i_1|\right)\left(q_1-x\right)^5 + \left(1-a_3|i_2|\right)\left(q_1+x\right)^5}{\left(q_1^{\,2}-x^2\right)^5} \right] \\ + 4b_1 &\left[\frac{sgn\left(i_1\right)\left(1-e^{-b_3|i_1|}\right)\left(q_2-x\right)^5 + sgn\left(i_2\right)\left(1-e^{-b_3|i_2|}\right)\left(q_2+x\right)^5}{\left(q_2^{\,2}-x^2\right)^5} \right] \end{aligned} \tag{2.35}$$

If the current and EMs are both identical, then the stiffness model can be further simplified to

$$k_{pe} = -8\left(1-a_3|i|\right)a_1 q_1 \frac{\left(5x^4+10q_1^2x^2+q_1^4\right)}{\left(q_1^{\,2}-x^2\right)^5} + 8sgn\left(i\right)\left(1-e^{-b_3|i|}\right)b_1 q_2 \frac{\left(5x^4+10q_2^2x^2+q_2^4\right)}{\left(q_2^{\,2}-x^2\right)^5} \tag{2.36}$$

2.4.2 Experimental Identification of the Combined Electromagnetic Spring

An experiment was conducted to find the constants a_{31}, a_{32}, b_{11}, b_{12}, b_{21}, b_{22} in equations (2.25) and (2.26). The same experiment was followed in Section 2.3.2 with an additional step. A current was applied by a DC power supply unit (PSU) from -2 A to +2 A by increments of 0.2 A at each displacement increment between the PM and EM. At each current increment, the force was measured by the force sensor. The experiment was done for both EM_1 facing the south pole of the PM block and EM_2 facing the north pole of the PM block. The sequential simplex algorithm was used to curve fit the force-displacement data. The fitting constants are listed in Table 2.6 and the analytical equation and experimental data are plotted in Figure 2.15. The data strongly confirms that the EMs are identical. For simplicity, the average of each fitting constant between the two EMs is calculated and denoted as b_1, b_2, a_3, and q_2 in accordance with equation (2.34).

Table 2.6 Experimental fitting constants for Eq. 2.10, 2.11, 2.26, and 2.27

Constants	EM_1	EM_2	$EM_{average}$
a_1 (10^{-6})	4.145	4.227	4.186
a_2 (10^{-2})	1.312	1.344	1.328
a_3 (10^{-1})	2.543	2.522	2.532
b_1 (10^{-5})	9.346	10.30	9.825
b_2 (10^{-2})	3.596	3.706	3.651
b_3 (10^{-1})	8.187	7.789	7.988

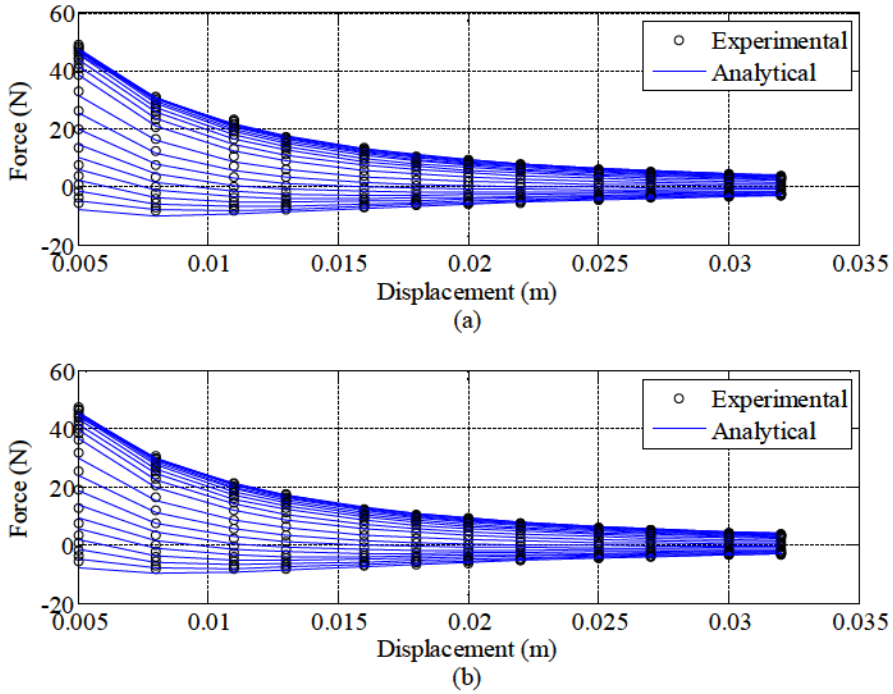

Figure 2.15 The EM force (the direction of increasing current is bottom to top) for (a) F_{pe1} of EM_1 on PM south (b) F_{pe2} of EM_2 on PM north

2.5 Characterization of the Combined System

2.5.1 Dynamic Model of the Combined System

The total force of the spring can be found by summing F_b and F_{pe}. The resulting analytical dynamic force and stiffness models are given in equation (2.37) and (2.38).

$$F_t = F_b + F_{pe}$$
$$= c_1 x^3 + c_2 - 8\left(1 - a_3|i|\right)a_1 q_1 \frac{x\left(q_1{}^2 + x^2\right)}{\left(q_1{}^2 - x^2\right)^4} + 8sgn(i)\left(1 - e^{-b_3|i|}\right)b_1 q_2 \frac{x\left(q_2{}^2 + x^2\right)}{\left(q_2{}^2 - x^2\right)^4} \quad (2.37)$$

$$k_t = k_b + k_{pe} = 3c_1 x^2 + c_2$$
$$-8\left(1 - a_3|i|\right)a_1 q_1 \frac{\left(5x^4 + 10q_1^2 x^2 + q_1^4\right)}{\left(q_1{}^2 - x^2\right)^5} + 8sgn(i)\left(1 - e^{-b_3|i|}\right)b_1 q_2 \frac{\left(5x^4 + 10q_2^2 x^2 + q_2^4\right)}{\left(q_2{}^2 - x^2\right)^5} \quad (2.38)$$

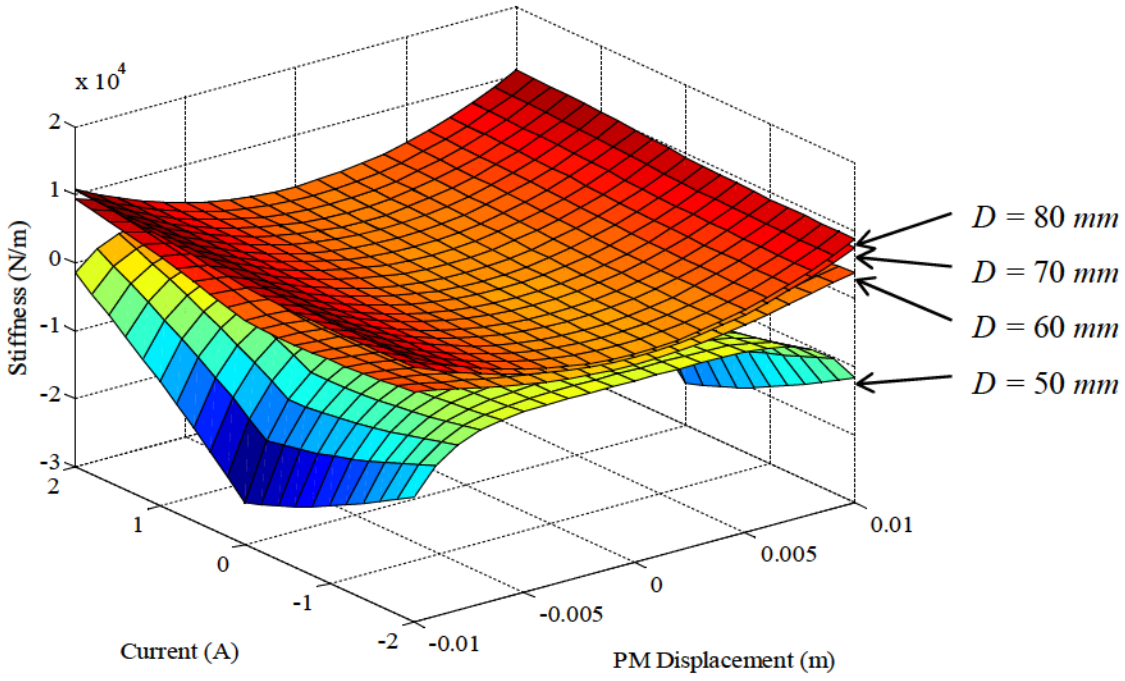

Figure 2.16 Total stiffness as a function of current and PM displacement for several fixed gap distances

Figure 2.16 shows the total system stiffness as a function of the EM current and PM displacement for case 2 MB tension at 50, 60, 70, and 80 mm EM gap distances. In general, the

total system stiffness as a function of PM displacement is quadratic in nature. For smaller gap distances ($D < 60$ mm), the stiffness-displacement parabola is negative due to the emphasized softening effect of the SC. This effect imposes a stability issue. A negative parabola implies that for a sufficient PM mass displacement, the total restoring force will act to pull the PM block away from its equilibrium position until the block either becomes stuck to an EM or is physically limited by the MB. Increasing the MB stiffness can offset the negative stiffness from the SCs and allow the system to be stable at smaller EM gap distances. When the EMs are energized, the stiffness-displacement parabola shifts. Increasing the EM current increases the overall linear and non-linear stiffness of the system while decreasing the EM current has the opposite effect.

2.5.2 Cubic polynomial Models for the Total Stiffness of the Combined System

Figure 2.17 shows the force-displacement curve for (a) the mechanical spring, (b) the magnetic spring, (c) the electromagnetic spring, and (d) the combined system spring (found in equation (2.37)) at a fixed gap distance of 80mm and a current of 1.5 A. Based on Figure 2.16 and Figure 2.17, two things are noted about the combined system spring: the dynamic force-displacement model resembles a cubic polynomial and the dynamic stiffness-displacement model resembles a quadratic polynomial. Therefore, like the characterization of the MB force, the total system dynamic force can be approximated by

$$F_t = Nx^3 + Mx \tag{2.39}$$

and the stiffness is given as

$$k_t = 3Nx^2 + M \tag{2.40}$$

where N is the coefficient of the nonlinear term and M is the coefficient of the linear term.

The constants of equation (2.39) were determined using Matlab's polynomial fitting function, *'polyfit'*, for both MB tension cases, 70 and 80 mm gap distances, and -1.5, 0, and 1.5 A current. The results are listed in Table 2.7. Increasing the MB tension increases the linear and non-linear stiffness. Increasing the gap distance reduces the softening effect of the magnetic spring thereby increasing the linear and non-linear stiffness. Similarly, increasing the EM current increases the linear and non-linear stiffness.

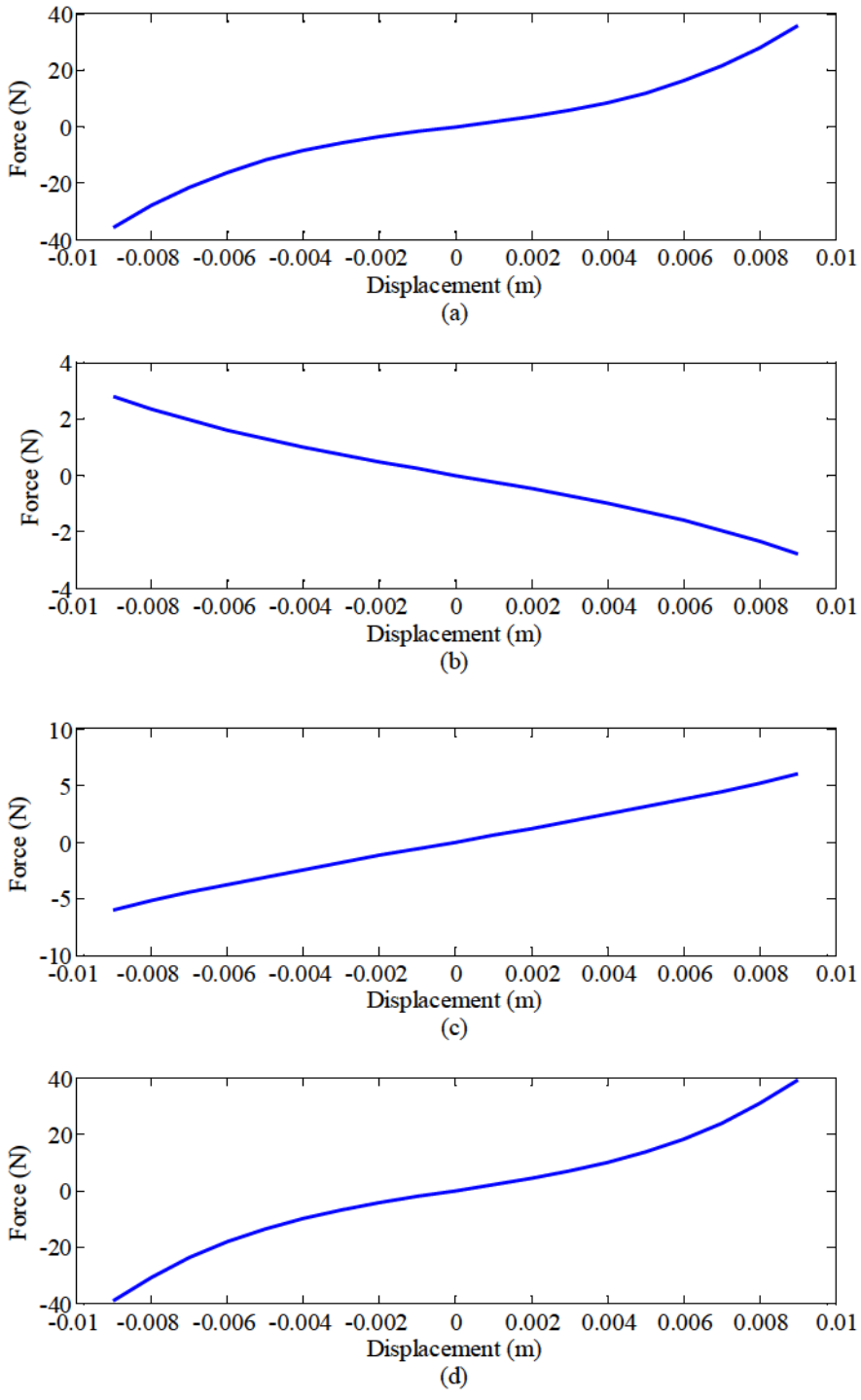

Figure 2.17 Force-displacement curves at 80 mm gap distance and 1.5 A current for (a) PM-MB spring F_b, (b) PM-SC spring F_{pc} (c) PM-EM spring F_{pf} (d) PM-MB-SC-EM spring F_t

Table 2.7 Linear and non-linear constants of equation (2.39) and (2.40) for different MB tensions, gap distances, and EM currents

Case	Gap Distance	Current	N (10^7)	M (10^3)
1	70	-1.5	2.287	-0.454
		0	2.277	0.173
		1.5	2.593	1.363
	80	-1.5	2.527	0.084
		0	2.553	0.538
		1.5	2.694	1.278
2	70	-1.5	2.459	0.278
		0	2.449	0.905
		1.5	2.765	2.095
	80	-1.5	2.699	0.815
		0	2.725	1.270
		1.5	2.866	2.010

2.5.3 Natural Frequency and Damping of the Combined System

A free response experiment was conducted to examine the natural frequency and damping of the combined system. The experimental setup is shown in Figure 2.18. The EM gap distance was configured for 70 and 80 mm and the EM current was set to -1.5, 0, and 1.5 A. At each gap distance and current setting, a free response of the system was induced by tapping the PM block. The free responses were measured by the optical reflex sensor and collected through the DAQ board and computer. Control Desk and Matlab Simulink were used to interface the experiment. This experiment was repeated for both the MB tension cases.

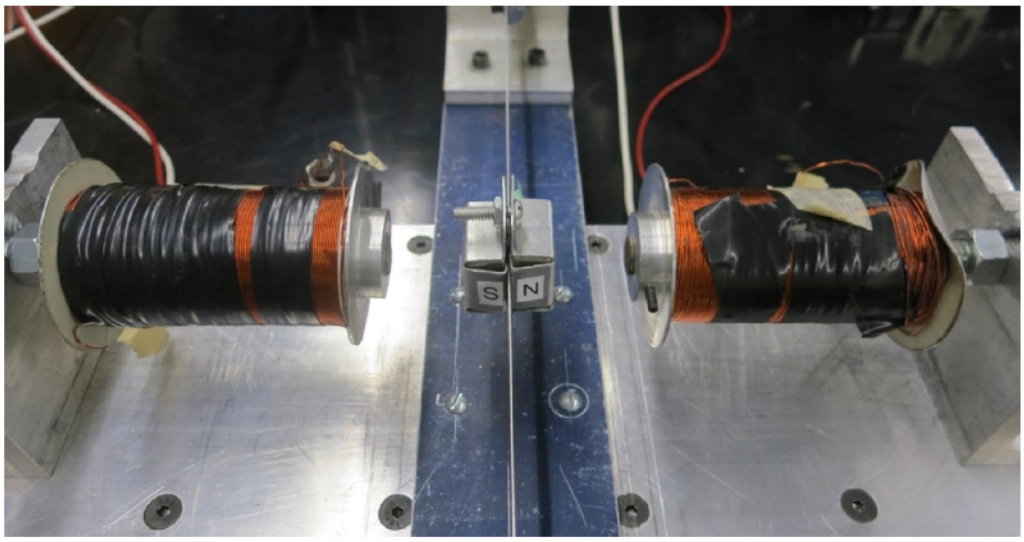

Figure 2.18 Combined system free response experiment setup

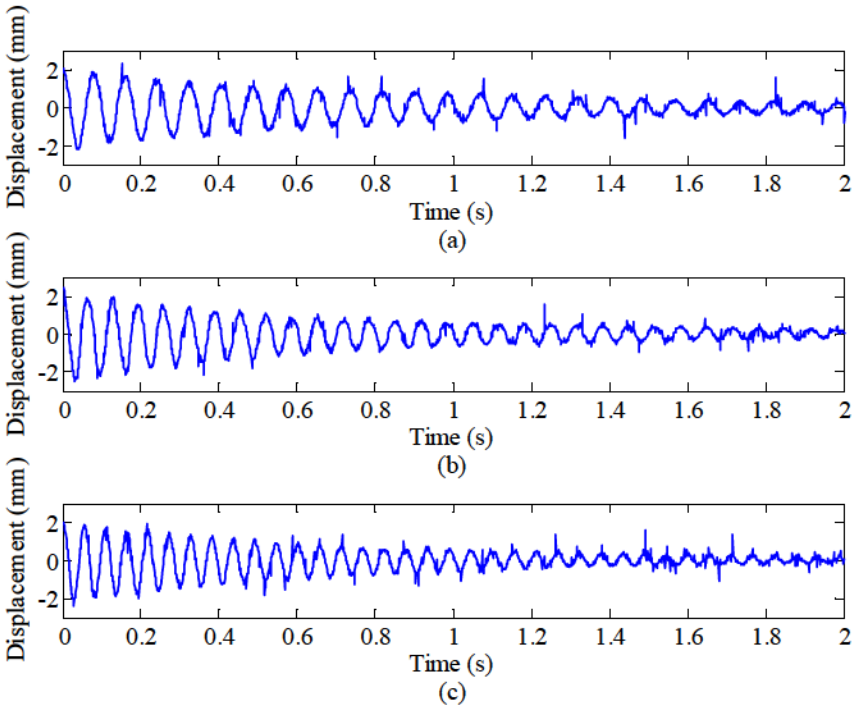

Figure 2.19 Typical free responses of the system for case 2 MB and 80 mm EM gap distance for different current values: (a) -1.5 A, (b) 0 A, and (c) 1.5 A

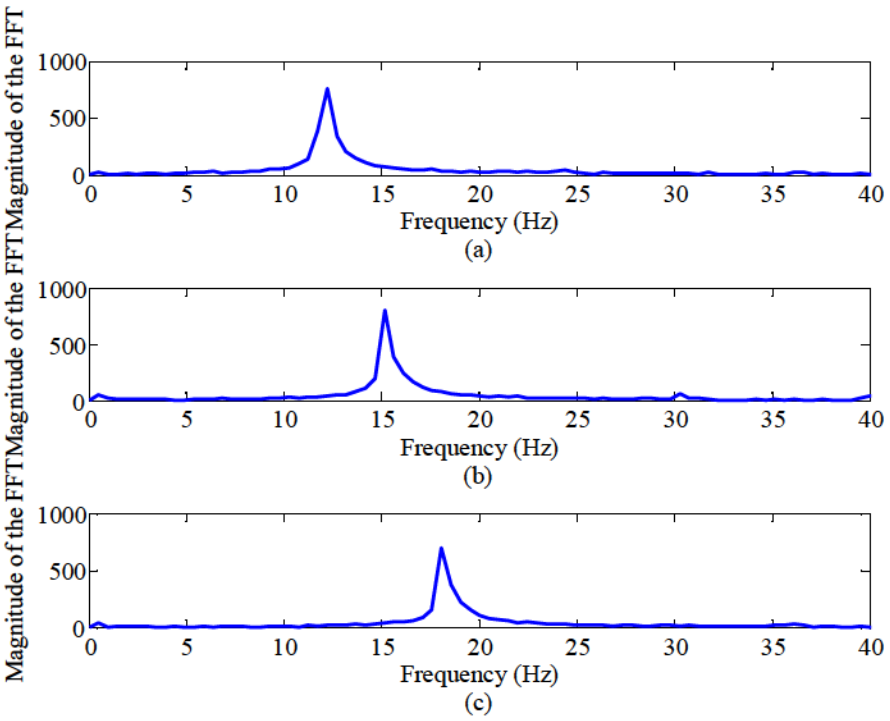

Figure 2.20 Typical FFT for case 2 MB and 80 mm EM gap distance for different current values: (a) -1.5 A, (b) 0 A, and (c) 1.5 A

Figure 2.19 shows a typical unfiltered free response for the system configured at medium tension and 80 mm gap distance with the current at (a) -1.5 A, (b) 0 A, and (c) 1.5 A. Applying Matlab's built in fast Fourier transform function, *fft*, to the free response data, the natural frequency of the system was found for each case. The natural frequencies were identified from the FFT peaks, similar to the peaks shown in Figure 2.20. The analytical model of the system's natural frequency can be determined by using equation (2.3). Using the small displacement approximation ($x \cong 0$) in equation (2.38), the linear stiffness is given by

$$k_t = c_2 - 8\left(1 - a_3|i|\right)\frac{a_1}{q_1^{\,5}} + 8sgn(i)\left(1 - e^{-b_3|i|}\right)\frac{b_1}{q_2^{\,5}} \tag{2.41}$$

and the analytical natural frequency becomes

$$\omega_n = \sqrt{\frac{k_t}{m}} \tag{2.42}$$

Table 2.8 shows the experimental and analytical natural frequencies of the system for different gap distances, tension cases, and EM current. In general, there is good agreement between the experimental results and analytical predictions except for cases where the predicted natural frequency was less than 7 Hz. As expected, an increase in the MB tension, EM current, or decreasing the gap distance all increased the system's natural frequency. When the negative stiffness was too strong (case 1, 70 mm gap distance, and -1.5 A EM current), the PM block was unable to return to the equilibrium position.

Table 2.8 System experimental and analytical natural frequencies

Case	Gap Distance (mm)	EM Current (A)	Experiment ω_n (Hz)	Analytic ω_n (Hz)
1 - Low	70	-1.5	n/a	n/a
		0	8.30	5.47
		1.5	16.11	16.24
	80	-1.5	8.79	3.94
		0	10.74	10.19
		1.5	15.14	15.77
2 – Medium	70	-1.5	7.81	7.16
		0	13.67	13.14
		1.5	19.04	20.62
	80	-1.5	12.21	12.58
		0	15.14	15.70
		1.5	18.07	19.78

The damping ratio was calculated by applying the logarithmic decrement method (equations (2.5) and (2.6)) to the measured free response data. The damping constant was calculated using equation (2.7) with the corresponding experimental natural frequencies. The results of the damping ratio ζ and the damping constant c are shown in Table 2.9. In general, increasing the MB tension, EM gap distance, and EM current will increase the overall stiffness of the system. As a result, ζ will decrease as predicted by equation (2.8). Note that ζ will decrease when the EM current increases in the positive direction and increase when the EM current increases in the negative direction.

Table 2.9 System damping ratio results for different beam tension cases at different gap distances

Case	EM Gap Distance (mm)	EM Current (A)	ζ	c
1	70	-1.5	n/a	n/a
		0	0.0666	0.924
		1.5	0.0236	0.634
	80	-1.5	0.0446	0.655
		0	0.0253	0.454
		1.5	0.0123	0.310
2	70	-1.5	0.0418	0.546
		0	0.0319	0.729
		1.5	0.0214	0.680
	80	-1.5	0.0143	0.291
		0	0.0138	0.350
		1.5	0.0113	0.342

2.6 Characterization of EM_B

A second set of EMs, EM set B denoted as EM_B, was characterized using an alternative characterization method to the methods presented in Sections 2.3 and 2.4. When comparing the two sets, the original EM pair presented in Section 2.1 will be denoted as EM set A or EM_A.

For this method, three assumptions are made: the MB's force model is symmetrical, the two EMs are identical, and the system's stiffness is linear about the equilibrium ($x \cong 0$). Based on these assumptions, the dynamic models given in equations (2.2), (2.20), (2.36), and (2.38) are linearized about the equilibrium position ($x \cong 0$):

$$k_b = c_2 \tag{2.43}$$

$$k_{pc} = -8\frac{a_1}{q_1^5} \tag{2.44}$$

$$k_{pe} = -8\left(1 - a_3|i|\right)\frac{a_1}{q_1^5} + 8sgn(i)\left(1 - e^{-b_3|i|}\right)\frac{b_1}{q_2^5} \tag{2.45}$$

$$k_t = c_2 - 8\left(1 - a_3|i|\right)\frac{a_1}{{q_1}^5} + 8sgn(i)\left(1 - e^{-b_3|i|}\right)\frac{b_1}{{q_2}^5} \tag{2.46}$$

As a result of linearization, the following relationship between the stiffness and natural frequency holds:

$$k = {\omega_n}^2 m \tag{2.47}$$

A series of experiments were conducted to identify the constants in equations (2.44) and (2.45) for EM_B. An accelerometer was mounted on the PM block by adhesive wax and connected to the B&K charge amplifier and DAQ system. A dedicated computer running Pulse Labshop measured the natural frequency using an online FFT. First, the MB natural frequency was measured via induced free response. Second, the EM_B set was added. Then, the EM gap distances were varied from 0.015 m to 0.045 m with the PM block at the center. At each increment, the current was varied from -2 A to 0 A by increments of 0.25 A. At each gap distance and current increment, the natural frequency was measured via induced free response. The stiffnesses of the mechanical, magnetic, and electromagnetic spring were calculated using equation (2.47) and the measured natural frequencies. The fitting constants in equations (2.44) and (2.45) were identified using the sequential simplex algorithm. The determined constants are shown in Table 2.10. Figure 2.21 and Figure 2.22 compares the experimental data and analytical model for the magnetic and combined electromagnetic spring.

Table 2.10 EM_B Fitting constants

Constants	**EM_B**
a_1 (10^{-6})	1.892
a_2 (10^{-2})	1.006
a_3 (10^{-3})	1.606
b_1 (10^{-4})	9.667
b_2 (10^{-2})	4.860
b_3 (10^{-2})	3.504

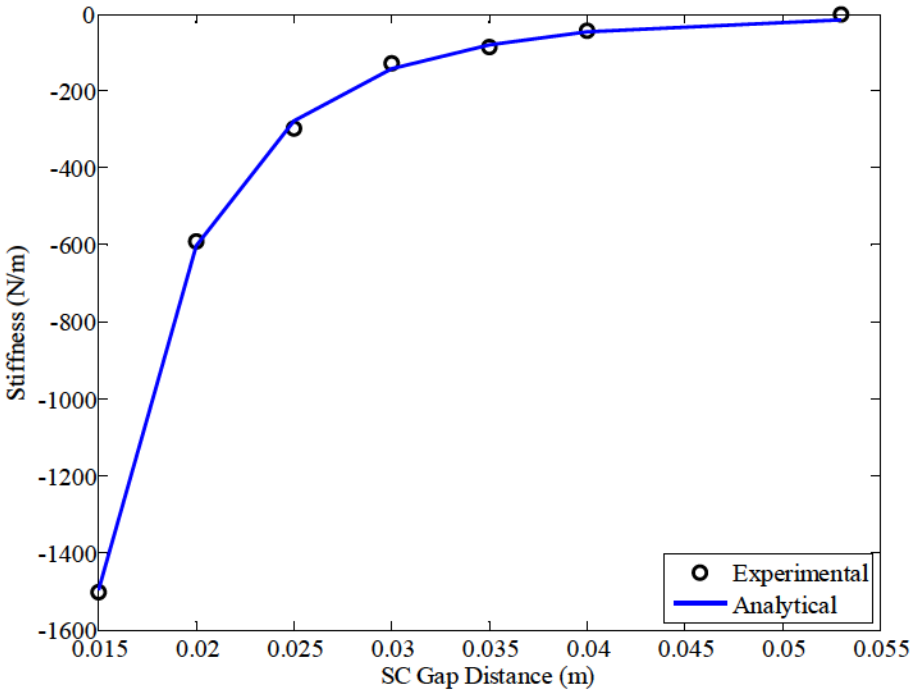

Figure 2.21 Stiffness model of the PM-SC spring for EM_B

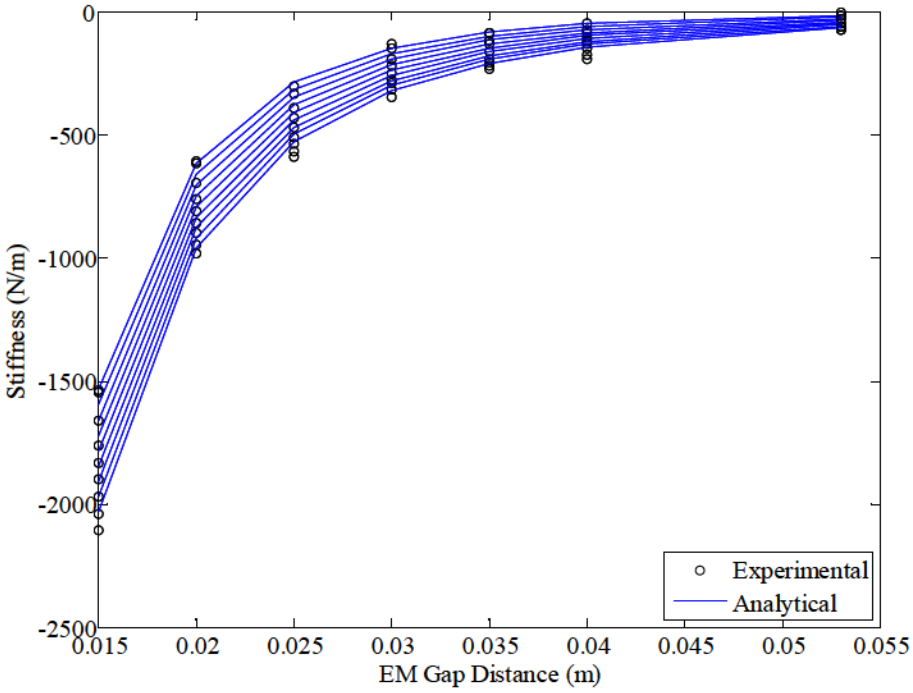

Figure 2.22 Stiffness model of the PM-SC-EM spring for EM_B

2.7 Identification of the System Time Delay

An experiment was conducted to determine the total system time delay τ_d. A step voltage signal was sent from the computer to the EMs and the PM displacement was measured. Figure 2.23 shows the displacement step response. The time difference between the computer step signal (dotted green) and the filtered response signal (solid blue) was measured for experimental iterations. An average time-delay was determined to be approximately 12 ms.

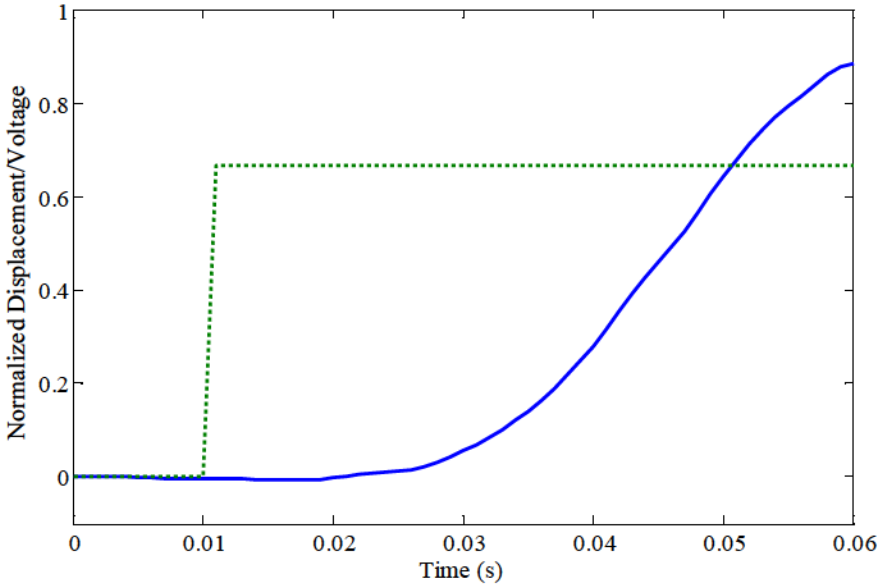

Figure 2.23 Voltage step input (dotted green) and mass displacement response (blue)

2.8 Characterization of the EM Dynamics

2.8.1 EM Inductance

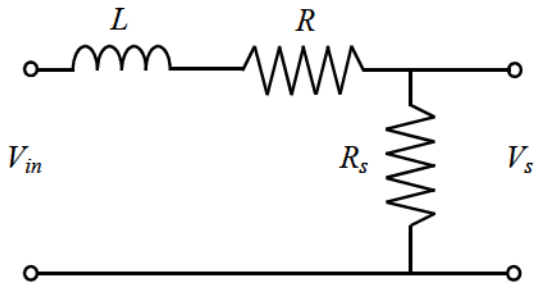

Figure 2.24 EM circuit diagram

Figure 2.24 shows the EM circuit used to identify the EM inductance and equation (2.48) shows the corresponding governing equation. L and R are the inductance and resistance of the EM, R_s and V_s are the resistance and voltage of the 1 Ω power resistor, V_{in} is the voltage from the PSU, and $i(t)$ is the current in the circuit.

$$L\dot{i}(t)+(R+R_s)i(t)=V_{in} \tag{2.48}$$

The general solution to this differential equation is [48]

$$i(t)=\frac{V}{R+R_s}\left(1-e^{\frac{R+R_s}{L}t}\right) \tag{2.49}$$

where the inductance term can be rearrange to be

$$L=-\frac{(R+R_s)t}{\ln\left(\frac{i(t)(R+R_s)}{V}\right)} \tag{2.50}$$

An experiment was conducted to determine the EM inductance in equation (2.50) for EM_A and EM_B. A step voltage of 22 V from the PSU was applied to the circuit. The current in the circuit was determined by measuring the voltage across the 1 Ω power resistor and applying Ohm's law. The voltage step responses of EM_A and EM_B are shown in Figure 2.25.

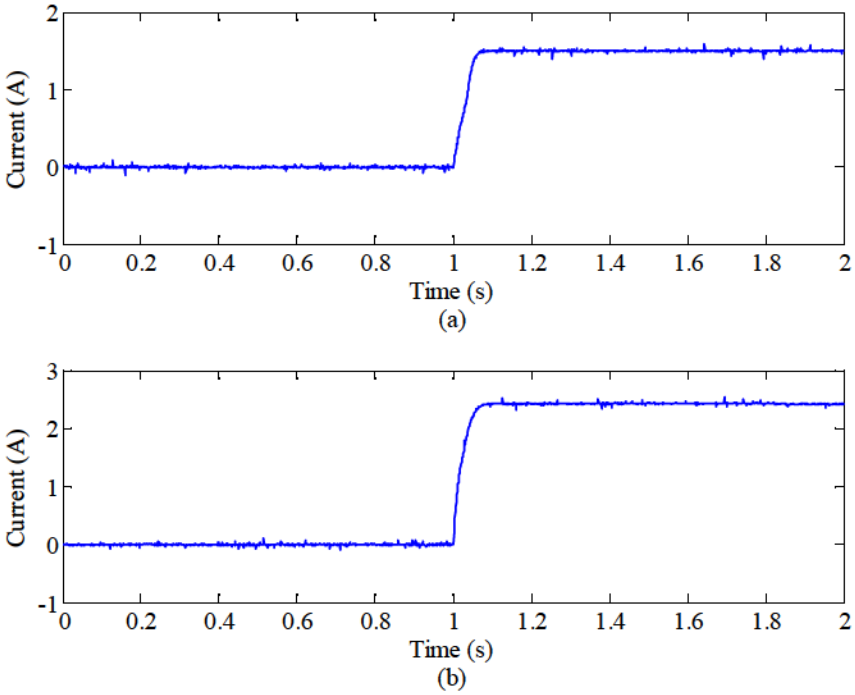

Figure 2.25 Voltage step response of (a) EM_A and (b) EM_B

A set of values was selected corresponding to half of the steady state current ($t_{1/2}$, $i(t_{1/2})$) from Figure 2.25. The selected points were substituted into (2.50) to solve for the inductance. The inductance results are listed in Table 2.11.

Table 2.11 Experimental inductance

EM set	*L* (H)
A	0.55
B	0.21

2.8.2 EM Back EMF

The motion of the PM block between the two SCs induces a changing magnetic field. According to Faraday's law of induction and Lenz's law, the changing magnetic field induces a current in the EM coil that opposes the motion of the PM block [49]. This back electromotive force (back EMF) acts as a damping force that is proportional to the velocity of the mass. Based

on the experimental setup shown in Figure 2.14 and assuming that the EMs are identical, the dynamics of the actuators are given as

$$\begin{aligned} L\dot{i}_1(t) + Ri_1(t) - V_{emf} &= V_{in1} \\ L\dot{i}_2(t) + Ri_2(t) + V_{emf} &= V_{in2} \end{aligned} \tag{2.51}$$

$$V_{emf} = k_v \dot{x} \tag{2.52}$$

where V_{emf} is the induced voltage and k_v is the back EMF proportional constant. The numeric subscripts denote the EM. The sign of V_{emf} was determined by Lenz's Law.

An experiment was conducted to determine k_v based on equation (2.52). A 16 Hz sinusoidal disturbance was input into EM_1 causing the PM to oscillate. The induced voltage was measured across EM_2 directly through the DAQ board and computer. Control desk and Matlab Simulink were used to interface the experiment. This experiment was repeated for EM_A and EM_B at 70 and 80 mm EM gap distances. A typical EMF voltage and velocity response is shown in Figure 2.26. The peaks of the velocity and EMF voltage were used in equation (2.52) to identify k_v. Several peaks were chosen and the average was taken to eliminate any high frequency distortion. The resulting k_v are listed in Table 2.12.

Table 2.12 Experimental back EMF proportional constant

EM Set	**EM Gap Distance (mm)**	**Back EMF Constant k_v (Vs/m)**
A	70	4.127
	80	3.091
B	70	2.266
	80	1.918

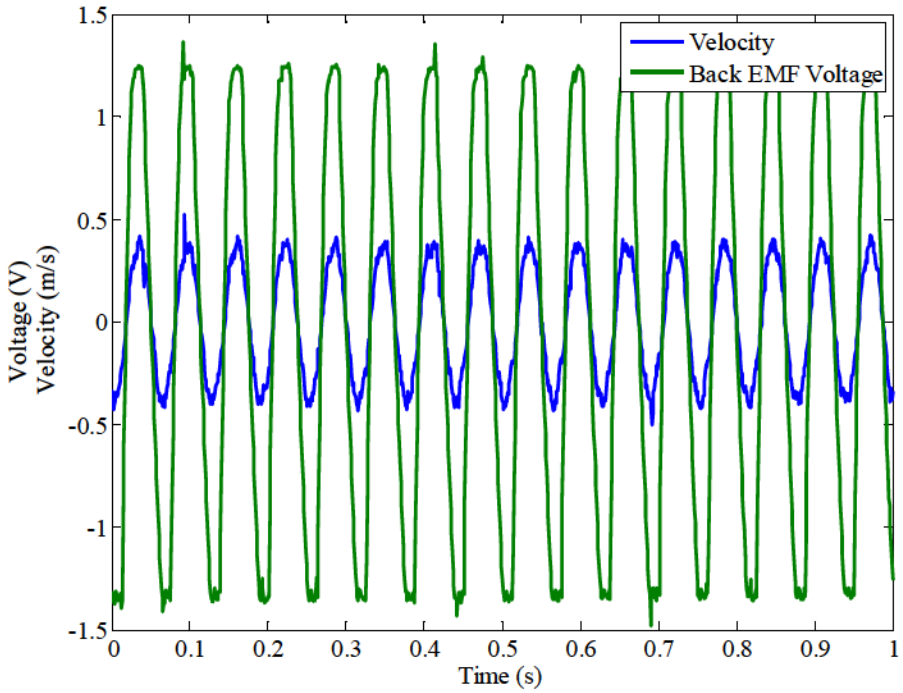

Figure 2.26 Induced back EMF response

2.9 Conclusions

In this chapter, the experimental apparatus used for this study was illustrated. An equivalent force and stiffness model were presented. An analytical model of each dynamic force and stiffness was developed. The dynamic force models were identified through a series of force-displacement experiments. The natural frequency and viscous damping constants were identified from a series of free-response experiments. The results showed that the combined spring force could be modeled as a cubic polynomial. A secondary set of EMs (EM_B) was identified by linearizing the dynamic models and conducting a series of free-response experiments. The EM dynamics and system time delay were also identified. This characterization procedure was necessary in order to conduct simulations for the prediction and development of the SS controller presented in the following sections.

Chapter 3 – SS Control & Simulation

This chapter presents a switchable stiffness (SS) control strategy [23] used to suppress the free vibration of a simple mechanical system, idealized as a SDOF spring-mass system. This control strategy is investigated through computer simulations based on the modeling and characterization presented in Chapter 2. Section 3.1 presents the concept, stability and mechanism of the SS control. Section 3.2 studies the effect of the inherent system time-delay and proposes a novel method used to overcome possible instabilities. Finally, the conclusions are presented in Section 3.4.

3.1 SS Control Strategy

3.1.1 SS Concept and Control Law

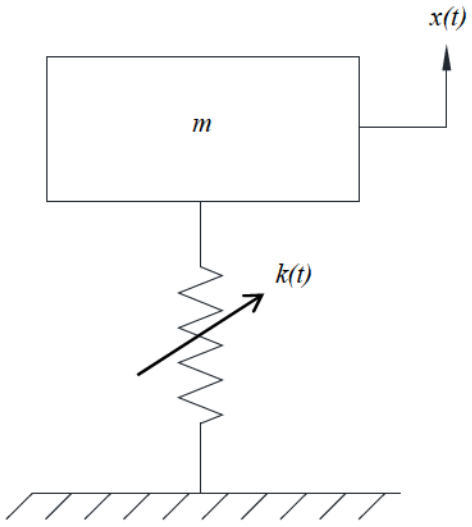

Figure 3.1 Single degree of freedom (SDOF) vibrating system

The SS control strategy aims to suppress the free vibration of a typical SDOF system. The system under consideration is shown in Figure 3.1 where m and $k(t)$ are the mass and switchable stiffness of the system, respectively. The governing equation is given in equation (2.1) where $\ddot{x}(t)$, $\dot{x}(t)$, and $x(t)$ are the acceleration, velocity, and displacement of the system, respectively. The initial conditions are denoted as $\dot{x}(0)$ and $x(0)$.

$$m\ddot{x}(t)+k(t)x(t)=0,\ x(0)\ \text{and}\ \dot{x}(0) \tag{3.1}$$

The SS control achieves vibration suppression by actively switching $k(t)$ between two distinct states based on the position and velocity feedback. The system assumes a high stiffness state when the mass is moving away from its equilibrium and a low stiffness state when the mass is moving towards its equilibrium. Stiffness switching occurs when the mass changes direction with respect to the equilibrium position. This control strategy can be expressed as

$$k(t)=\begin{cases} k_{high} & \text{for } x(t)\dot{x}(t)\geq 0 \\ k_{low} & \text{for } x(t)\dot{x}(t)<0 \end{cases} \tag{3.2}$$

where k_{high} is the high stiffness state and k_{low} is the low stiffness state. Equation (3.2) can be rewritten as [27]

$$k(t)=K_1+K_2 sgn(x\dot{x}) \tag{3.3}$$

where $sgn()$ is the sign function and the terms K_1 and K_2 are defined as

$$\begin{aligned} K_1&=\frac{(k_{high}+k_{low})}{2} \\ K_2&=\frac{(k_{high}-k_{low})}{2} \end{aligned} \tag{3.4}$$

From equation (3.3), it is observed that the state-feedback stiffness switching is only dependent on the function $sgn(x\dot{x})$ which can be interpreted as the direction of the mass with respect to the equilibrium position. A positive $sgn(x\dot{x})$ implies that the mass is moving away

from the equilibrium. A negative $sgn(x\dot{x})$ implies that the mass is moving towards the equilibrium. The switching is independent of the states' magnitudes.

3.1.2 Closed Loop Stability Analysis

Lyapunov's direct method [50] was used to prove the stability of the closed loop system given in equations (2.1) and (3.3). For generality, viscous damping was added to the system equation. The state variables are defined as

$$X = \begin{bmatrix} X_1 \\ X_2 \end{bmatrix} = \begin{bmatrix} x(t) \\ \dot{x}(t) \end{bmatrix} \tag{3.5}$$

and the state space is defined as

$$\dot{X} = \begin{bmatrix} \dot{X}_1 \\ \dot{X}_2 \end{bmatrix} = \begin{bmatrix} 0 & 1 \\ -k(t)/m & -c/m \end{bmatrix} \begin{bmatrix} X_1 \\ X_2 \end{bmatrix} \tag{3.6}$$

A Lyapunov candidate function was chosen to represent the energy of the system

$$V(X) = \frac{1}{2} K_1 X_1^{\,2} + \frac{1}{2} m X_2^{\,2} \tag{3.7}$$

The Lyapunov candidate function was differentiated with respect to time to yield

$$\dot{V}(X) = -K_2 \left| X_1 X_2 \right| - c X_2^{\,2} \tag{3.8}$$

Without damping ($c = 0$), the derivative is given as

$$\dot{V}(X) = -K_2 \left| X_1 X_2 \right| \tag{3.9}$$

The resulting Lyapunov derivatives are negative semi-definite. Therefore, based on equations (3.8) and (3.9) and LaSalle's invariance theorem [50], the closed loop system (with or without damping) is globally asymptotically stable.

3.1.3 SS Control and Mechanism

Simulations were conducted to illustrate the control and mechanism of the SS strategy. Matlab Simulink was used to simulate the model based on equations (3.1) and (3.3). The fixed step Runge Katta (ode45) numerical solver was used. The stiffness values were chosen from the linearized model based on medium MB tension and 80 mm EM gap distance. The initial conditions were chosen arbitrarily. No damping was considered. The Simulink block diagram is shown in Figure 3.2 and the relevant simulation parameters are shown in Table 3.1.

Table 3.1 Simulation parameters

Parameter	Configuration
c	0 [kg/s]
k_{high}	2010 [N/m]
k_{low}	815 [N/m]
$x(0)$	-3.4 [mm]
$\dot{x}(0)$	0.31 [m/s]

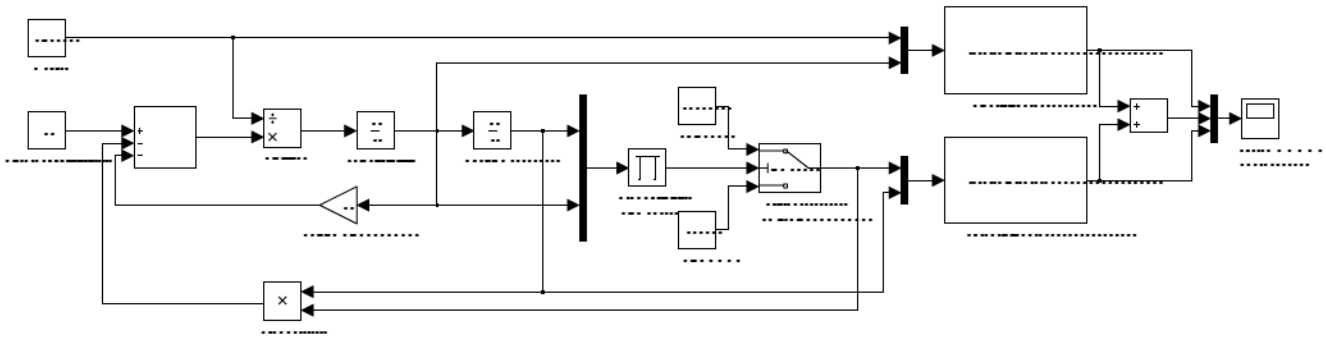

Figure 3.2 Simulink block diagram of SS control on a simple model

Figure 3.3 shows the simulation results: (a) the system control response and (b) the stiffness switching for the system under consideration. It is observed that the displacement and velocity amplitudes decay rapidly; the free vibration of the system is being effectively suppressed. Additionally, it is observed that the stiffness actively switches in accordance to the control law in equation (3.2) and that this switching only occurs when the mass changes

directions with respect to the equilibrium position. There are two cases where this change happens. First, a direction change occurs when the mass crosses the equilibrium (the zeros of the displacement curve). At this point, the stiffness switches from k_{low} to k_{high} (stiffness addition). Second, a direction change occurs when the mass reaches the oscillation peaks (the top or bottom peaks of the displacement curve). At this point, the stiffness switches from k_{high} to k_{low} (stiffness reduction).

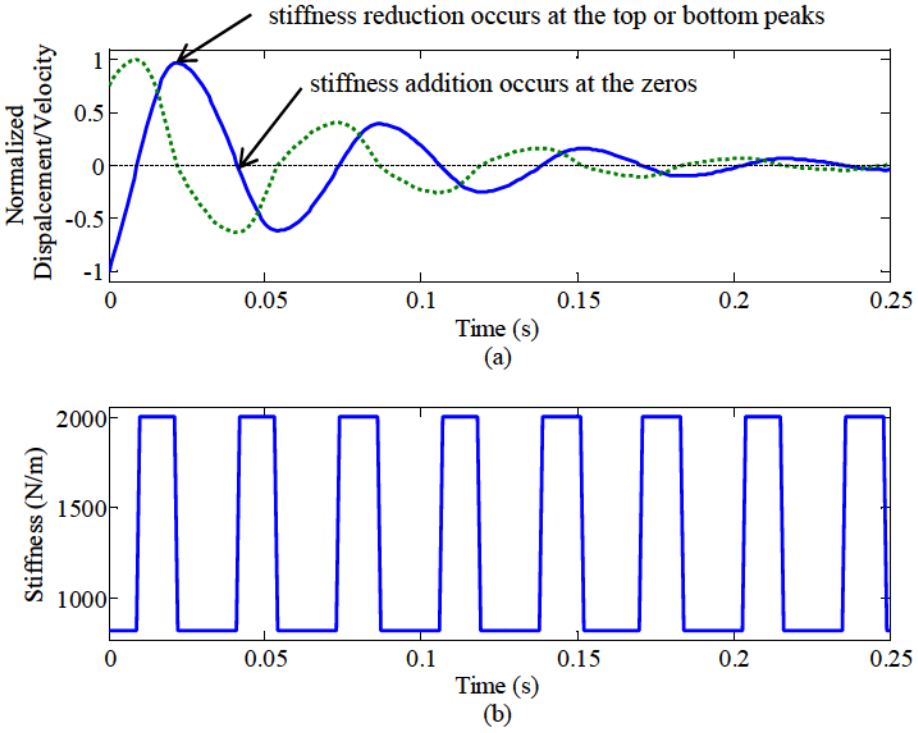

Figure 3.3 Simulated SS control response on undamped SDOF system (a) normalized displacement $\frac{x(t)}{\max|x(t)|}$ (solid blue) and normalized velocity $\frac{\dot{x}(t)}{\max|\dot{x}(t)|}$ (dashed green) response and (b) stiffness switching.

3.1.4 Energy Dissipation

For reference, Figure 3.4 (a) shows the system's displacement response for a single period. Additionally, Figure 3.5 shows the corresponding displacement and velocity phase plot. The first peak, second peak, and third peak are labeled x_p, $x_{p+T/2}$, and x_{p+T} with respect to the period of the system T. The subscript p implies that x is at a peak. Figure 3.4 (b) shows the kinetic, potential, and total system energies corresponding to Figure 3.4 (a). The total energy of the system is given as

$$E = K + P \tag{3.10}$$

where the kinetic energy K and the potential energy P are defined as

$$K = \frac{1}{2}m\dot{x}^2 \qquad P = \frac{1}{2}kx^2 \tag{3.11}$$

To illustrate how the SS control suppresses vibration, consider the two stiffness switching cases and the system energies shown in Figure 3.4. During stiffness addition when $x = 0$, the change in energy is given as

$$\Delta E_{zero} = \Delta K_{zero} + \Delta P_{zero} = \left[\frac{1}{2}m\left(\dot{x}^2 - \dot{x}^2\right)\right] + \left[\frac{1}{2}\left(k_{high} - k_{low}\right)0^2\right] \tag{3.12}$$

The resulting change in energy at this instance is

$$\Delta E_{zero} = 0 \tag{3.13}$$

It is observed that the stiffness addition at the zeros does not change the total energy of the system. During stiffness reduction when $x = x_{peak}$, the change in energy is given as

$$\Delta E_{peak} = \Delta K_{peak} + \Delta P_{peak} = \left[\frac{1}{2}m\left(0^2 - 0^2\right)\right] + \left[\frac{1}{2}\left(k_{low} - k_{high}\right)x_{peak}^2\right] \tag{3.14}$$

The resulting change in energy at this instance is

$$\Delta E_{peak} = -\frac{1}{2}\Delta k x_{peak}^2 \tag{3.15}$$

where Δk is the change in stiffness defined as

$$\Delta k = k_{high} - k_{low} \tag{3.16}$$

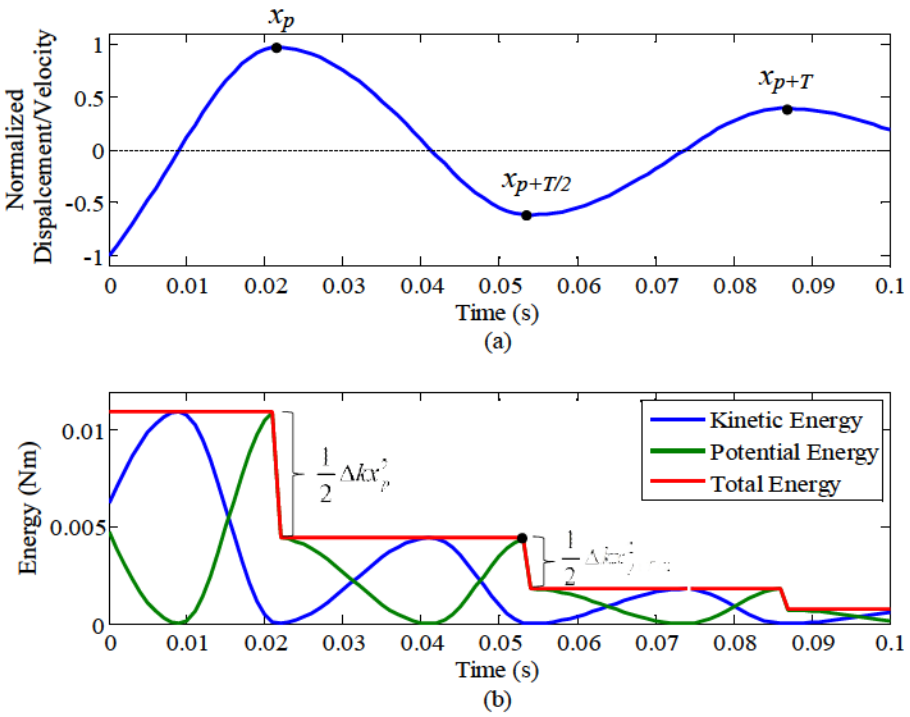

Figure 3.4 Simulated energy response of kinetic energy (blue), potential energy (red), and total energy (green)

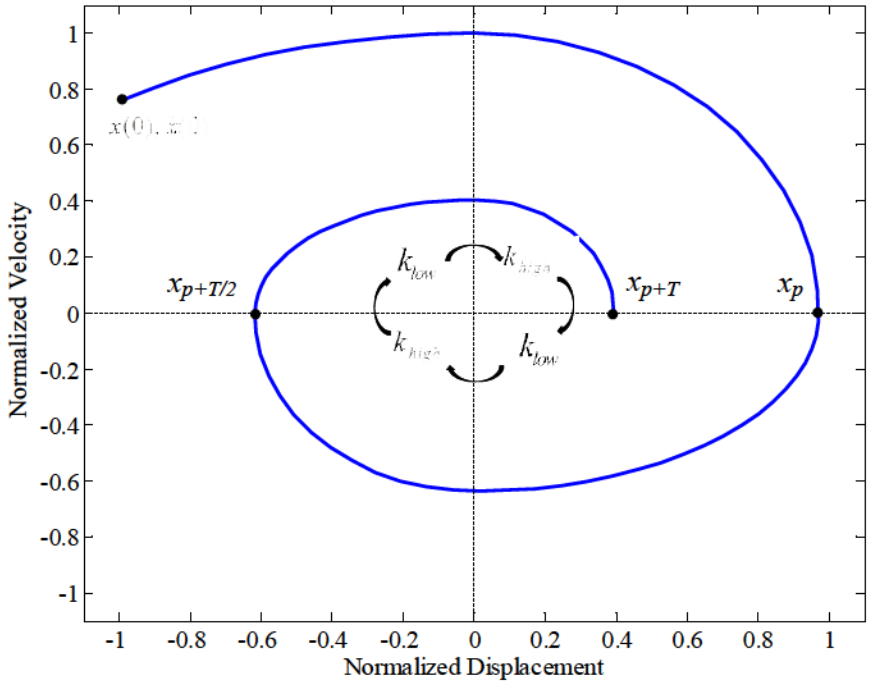

Figure 3.5 Displacement and velocity phase plot

Therefore, three conclusions can be made about the switchable stiffness mechanism. First, stiffness addition at the zeros does not add energy to the system and only serves to reset the stiffness to k_{high}. Second, the stiffness reduction at the peaks removes energy from the system by directly reducing potential energy. The result is energy dissipation at each peak. Third, the amount of energy dissipated is directly proportional to the change in the stiffness Δk.

3.1.5 Vibration Damping

The relationship between the stiffness switching and energy dissipation has been established in equations (3.13) and (3.15). However, it is desirable to obtain a relationship between the stiffness switching and the amount of vibration being suppressed.

The relationship between the stiffness switching and the amplitude reduction can be determined by examining the displacement peaks and the energies of the system shown in Figure 3.4. First, consider the change in energy between the peaks x_p and $x_{p+T/2}$. It has been previously established that the change in energy is only caused by stiffness reduction at the peaks. Therefore, the change in energy between x_p and $x_{p+T/2}$ is equivalent to the stiffness reduction occurring between these peaks. Therefore, the energy conservation equation is given as

$$\Delta E = \frac{1}{2}k_{high}x_{p+T/2}^2 - \frac{1}{2}k_{high}x_p^2 = -\frac{1}{2}\Delta k x_p^2 \tag{3.17}$$

Solving for $x_{p+T/2}$ yields

$$x_{p+T/2} = -x_n\sqrt{\frac{k_{low}}{k_{high}}} \tag{3.18}$$

Equation (3.18) suggests that for each successive half period, the amplitude decays by a factor of $\sqrt{k_{low}/k_{high}}$. Similarly, consider the change in energy between x_p and x_{p+T}.

$$\frac{1}{2}k_{high}x_{p+T}^2 - \frac{1}{2}k_{high}x_p^2 = -\left[\frac{1}{2}\Delta k x_p^2 + \frac{1}{2}\Delta k x_{p+T/2}^2\right] \tag{3.19}$$

Substituting equation (3.18) into equation (3.19) yields

$$x_{p+T} = x_p \left(\frac{k_{low}}{k_{high}} \right) \tag{3.20}$$

Equation (3.20) implies that for each successive period, the amplitude decays by a multiplicative factor of k_{low}/k_{high}. A more generalized relationship is given as

$$\left| x_{p+mT} \right| = \left| x_p \right| \left(\frac{k_{low}}{k_{high}} \right)^m \tag{3.21}$$

where m is the number of successive periods which can be whole numbers or increments of ½. Note that this equation is only valid for peaks and successive peaks. A stiffness ratio can be defined as

$$\alpha = \frac{k_{low}}{k_{high}} \tag{3.22}$$

As the stiffness ratio is directly proportional to the amplitude ratio for $m = 1$, the logarithmic decrement can be used to calculate an equivalent viscous damping ratio [41]. This damping is due to the control law and not to be confused with the damping due to the internal mechanical friction forces. The logarithmic decrement is given by

$$\hat{\delta} = \ln \frac{1}{\alpha} \tag{3.23}$$

The damping ratio can be estimated using the relationship between viscous damping and the logarithmic decrement [2]

$$\hat{\zeta} = \frac{\hat{\delta}}{\sqrt{4\pi^2 + \hat{\delta}^2}} \tag{3.24}$$

Using equations (3.22), (3.23), and (3.24) for this system under consideration, the damping ratio was found to be $\hat{\zeta} = 0.142$. This value can be confirmed by applying $x(t)$ and $x(t+T)$ from the simulation results in Figure 3.3 (a) to equations (2.5) and (2.6). The resulting damping ratio was also found to be $\zeta = 0.142$.

3.1.6 Inverted SS Control and the Instability Problem

The SS strategy can also be manipulated to excite the system [36]. To destabilize the system, the opposite SS control algorithm is applied: the system will assume a low stiffness state when the mass is moving away from equilibrium and a high stiffness state when the mass is moving towards equilibrium. The inverted SS control law can be expressed as

$$k(t) = \begin{cases} k_{high} & \text{for } x(t)\dot{x}(t) < 0 \\ k_{low} & \text{for } x(t)\dot{x}(t) \geq 0 \end{cases} \tag{3.25}$$

Figure 3.6 shows the simulation results: (a) the system response, (b) the stiffness switching, and (c) the energies for a system using the inverted control law. From (a) and (c), it can be seen that the system is unbounded. From (b), it can be seen that the opposite stiffness switching occurs. Stiffness reduction occurs at the zeros and only serves to reset the stiffness to k_{low}. Stiffness addition occurs at the peaks and adds energy to the system through the potential energy. This case reveals a possible instability issue for the SS control strategy. Inappropriate stiffness switching due to time delays may reduce the effectiveness or destabilize the SS control.

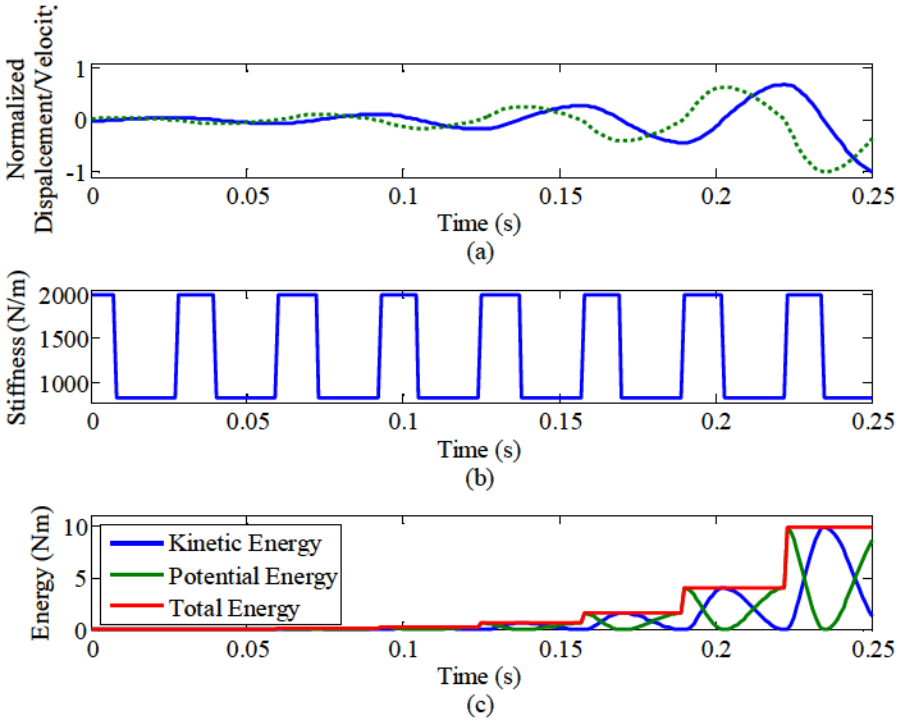

Figure 3.6 Simulated SS excitation response on undamped SDOF system (a) displacement (solid blue) and velocity (dotted green) response, (b) stiffness switching, and (c) kinetic energy (blue), potential energy (green), and total energy (red)

3.1.7 SS Control of a Non-Linear Dynamic System

Table 3.2 Simulation parameters

Parameter	Configuration
c	0.34 [kg/s]
V_{high}	20 [V]
V_{low}	-20 [V]
$x(0)$	-3.4 [mm]
$\dot{x}(0)$	0.31 [m/s]

A series of simulations were conducted based on the non-linear dynamic force and stiffness models presented in Chapter 2. Arbitrary initial conditions were chosen. The dynamics of the actuators were neglected. The MB tension was set to medium and the EM gap distance

was set to 80 mm. The Simulink block diagrams are shown in Figure 3.7 and the configuration parameters are shown in Table 3.2. The simulation results are shown in Figure 3.8. In general, the results show that the system states decay quickly due to the appropriate stiffness switching. It is also noted that for non-linear stiffness systems, the natural frequency and period varies as a function of the displacement. The period is expected to be shorter for larger vibration amplitudes and longer for smaller vibration amplitudes.

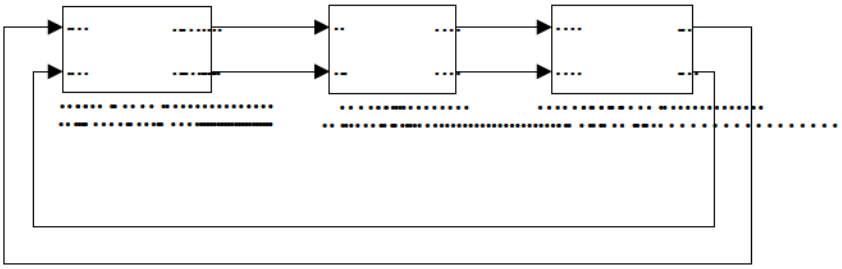

(a)

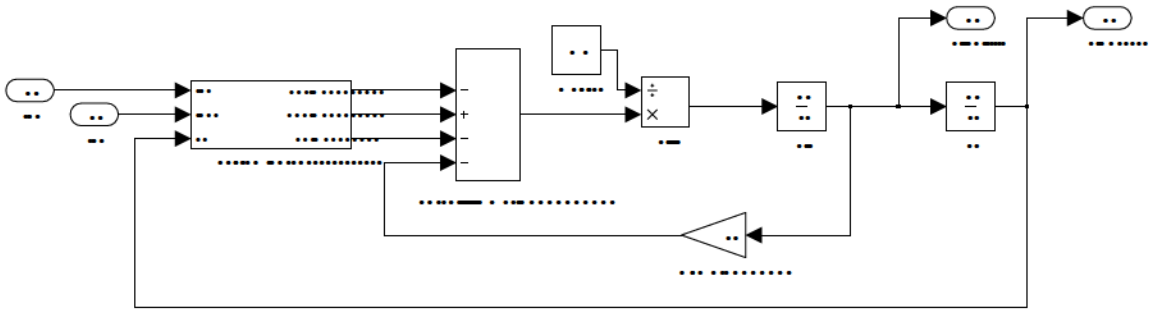

(b)

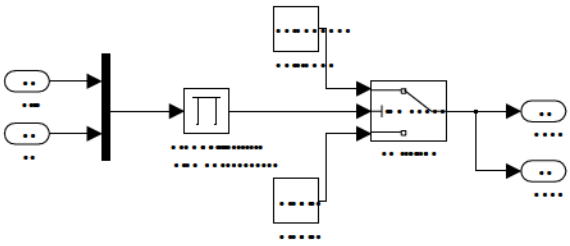

(c)

Figure 3.7 Simulink block diagram of SS control on a non-linear model (a) closed loop system (b) non-linear system dynamics (c) stiffness switching mechanism

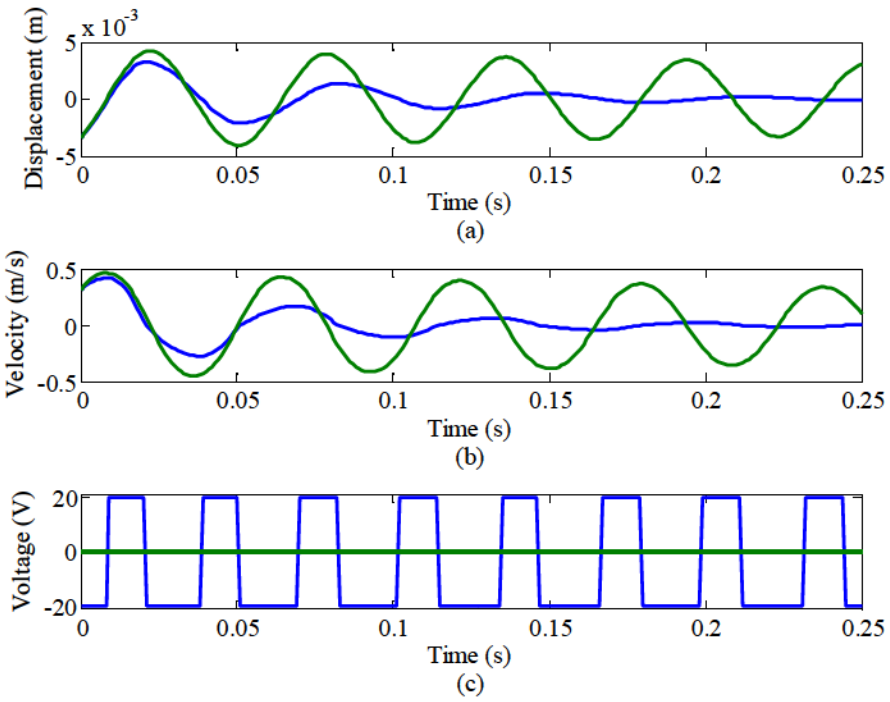

Figure 3.8 Simulated SS control (blue) and no-control (green) responses on damped non-linear system (a) displacement, (b) velocity, and (c) voltage

3.2 Delayed SS Control

3.2.1 System Time-Delay

Time delays are inherent in all real-time systems and pose one of the biggest challenges for the implementation of active and semi-active control. These delays arise due to the speed limit at which signals can be processed and transferred. In typical systems, these delays may be made up of sensor, actuator, computer, and filter delays [51]. The total delay, which is the summation of these delays, will cause an inappropriate application of the control signal. At worst, these delays will destabilize the system.

A simulation was conducted to show the effects of delays on the closed loop SS control. The same configuration was used in Section 3.2.1 with the addition of a delay added to the position and velocity signals. A time delay of 12 ms was used based on the identification in Section 2.7. As shown in Figure 3.9, an inherent time delay causes vibration amplification.

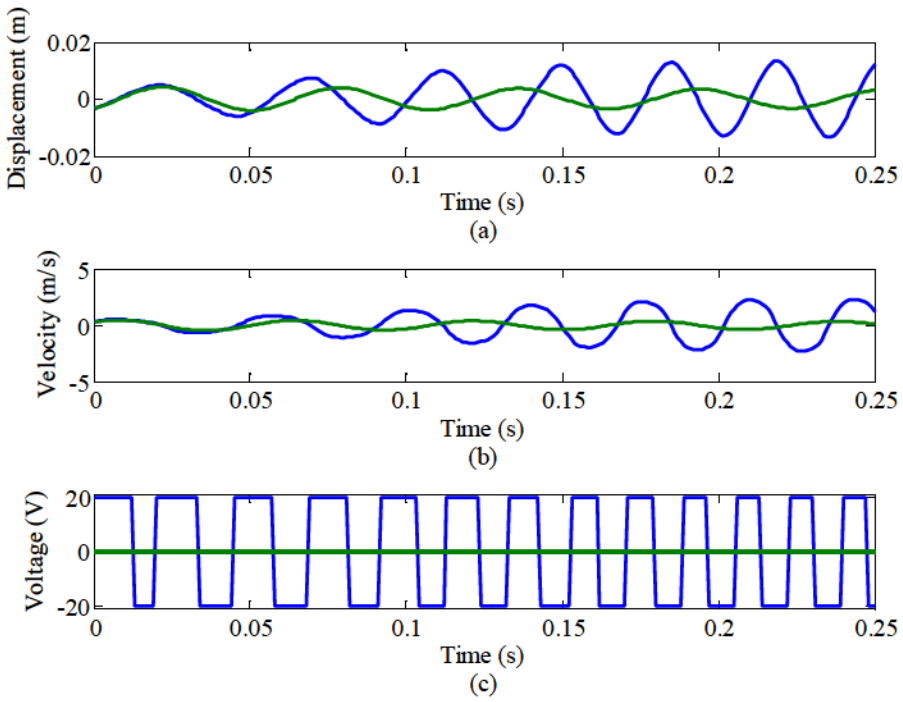

Figure 3.9 Simulated SS control (blue) and no-control (green) responses on damped non-linear system with inherent time delays (a) displacement, (b) velocity, and (c) voltage

To illustrate how delay can affect the system, consider the two idealized signals shown in Figure 3.10 and Figure 3.11. These signals represent a typical sinusoidal free vibration displacement response of the system. The delayed response (solid blue) is the response interpreted by the controller and the original response (dotted green) is instantaneous response of the system. Consider the state at point A_o. The signal at this point is delayed by τ_d and is not observed until point A_d A control signal sent at this point will not reach the system until point B_o (on the original response) or point B_d (on the delayed response). As a result, the control, which was intended for A_o, was applied at B_o. From Figure 3.11 (a), it is observed that if $\tau_d = \frac{1}{4}T$, the resulting SS control will be inverted. That is, the control signal for A_o is equivalent to the opposite control signal at B_o. The inverted control was shown to destabilize the system in Section 3.1.5. From Figure 3.11 (b), it is observed that if $\tau_d = \frac{1}{2}T$, the SS control will be applied correctly due to the symmetry of the system. That is, the control signal for A_o is equivalent to the control signal for B_o. Of course, if $\tau_d = T$, the delayed and original signals will overlap and the SS control will also be applied correctly.

In general, assuming that the response is sinusoidal in nature, the following statements can be made about the effects of time delay. (1) The SS control will be inverted and the closed loop system will become unstable if

$$\tau_d = h\frac{1}{4}T \tag{3.26}$$

where h is an odd whole number. (2) The SS control will be applied correctly and the system will become stable if

$$\tau_d = n\frac{1}{2}T \tag{3.27}$$

where n is a whole number. Essentially, equation (3.25) lists all the possible values of τ_d in which the control is inverted and unstable and equation (3.26) lists all the possible values of τ_d in which the control correct and stable.

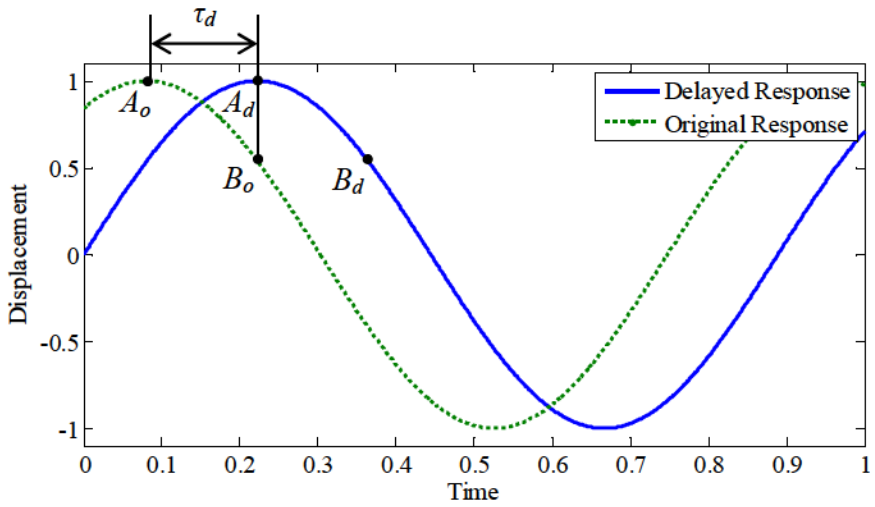

Figure 3.10 Actual signal and time-delayed signal comparison with (green) representing the real-time signal and (blue) representing the observed delayed signal

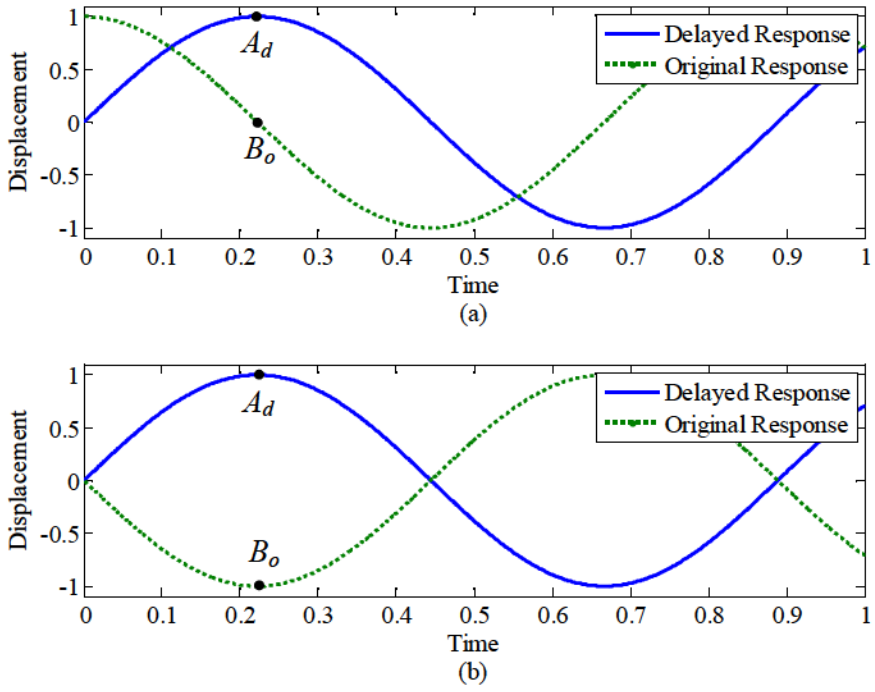

Figure 3.11 Actual signal and time-delayed signal comparison with (green) representing the real-time signal and (blue) representing the observed delayed signal for (a) $\tau_d = ¼T$ and (b) $\tau_d = ½T$

3.2.2 Delayed SS Control Strategy

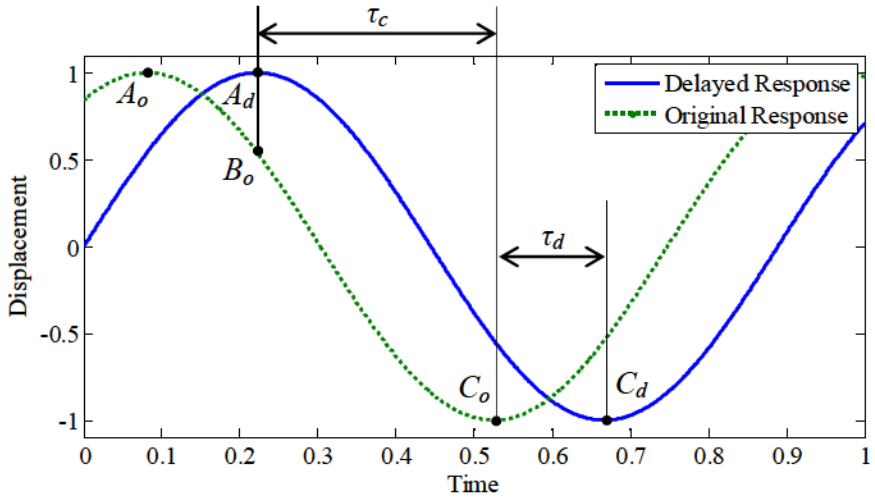

Figure 3.12 Actual signal and time-delayed signal comparison with (green) representing the real-time signal and (blue) representing the observed delayed signal for HP delayed SS control

Two strategies are proposed to overcome the instability problem due to time delays. These strategies involve the introduction of an intentional delay τ_c so that the SS control will be applied correctly and the system will be stable.

The first strategy, the half period (HP) delayed SS control, is illustrated in Figure 3.12. For brevity, this strategy will be referred to as the HP delayed control. Given the state at point A_d, it is impossible to control the original point A_o. A control signal based on A_d will be applied incorrectly at B_o on the original response. To overcome this error, an intentional delay τ_c is introduced such that the signal based on A_d will be applied half of a period later at C_o. Recall from Figure 3.11 that any multiple of a half of a period delay will result in the correct application of the SS control law.

Therefore, based on equation (3.27) and the HP delayed control is given as

$$k(t+\tau_c) = \begin{cases} k_{high} & \text{for } x(t)\dot{x}(t) \geq 0 \\ k_{low} & \text{for } x(t)\dot{x}(t) < 0 \end{cases} \tag{3.28}$$

where the HP intentional delay is defined as

$$\tau_c = n\frac{1}{2}T - \tau_d, \quad \tau_c \geq 0 \tag{3.29}$$

Note that n should be chosen such that τ_c is minimized. The average period is used

$$T = \frac{T_{high} + T_{low}}{2} \tag{3.30}$$

where T_{high} is the period resulting from the high stiffness state and T_{low} is the period resulting from the low stiffness state.

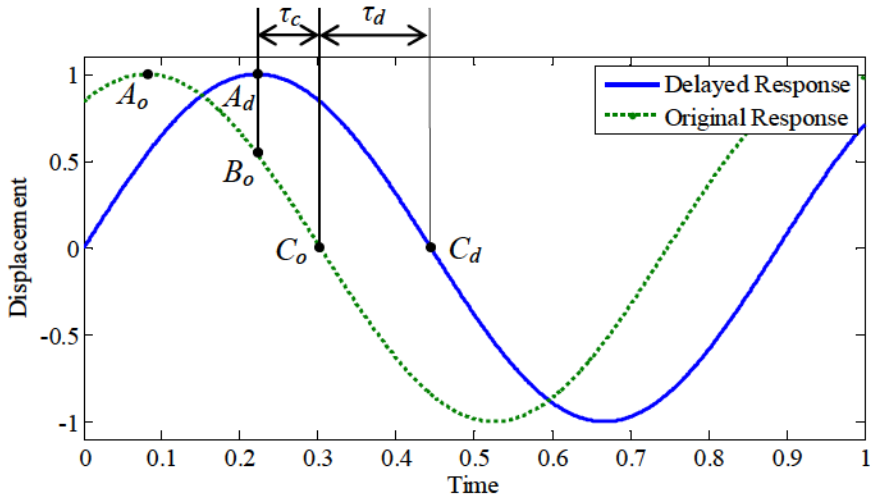

Figure 3.13 Actual signal and time-delayed signal comparison with (green) representing the real-time signal and (blue) representing the observed delayed signal for QP delayed inverted SS control

The second strategy, the quarter period (QP) inverted delayed SS control, is shown in Figure 3.13. For brevity, this strategy will be referred to as the QP delayed control. An intentional delay is introduced such that the signal based on A_d will be applied a quarter of a period later at C_o. Recall from Figure 3.11 that any odd multiple of a QP delay will result in the opposite application of the SS control law and result in instability. Therefore, the inverted SS control law is used. The opposite application of the inverted SS control law will result in the correct application of the SS control law. Therefore, based on equation (3.26), the QP delayed SS control is given as

$$k(t+\tau_c) = \begin{cases} k_{high} & \text{for } x(t)\dot{x}(t) < 0 \\ k_{low} & \text{for } x(t)\dot{x}(t) \geq 0 \end{cases} \tag{3.31}$$

$$\tau_c = h\frac{1}{4}T - \tau_d, \quad \tau_c \geq 0 \tag{3.32}$$

Note that h should be chosen such that τ_c is minimized. In general, the control law for which τ_c is minimized should be chosen.

3.2.3 Delayed SS Control Simulations

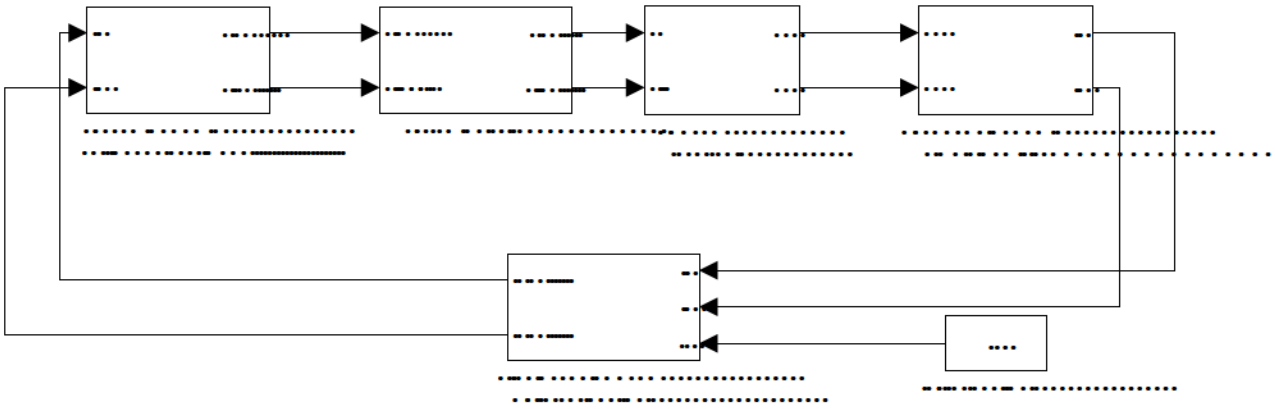

Figure 3.14 Simulink block diagram of the closed-loop SS system with system delays and delay control

Simulations based on the QP and HP delayed control were conducted. The non-linear stiffness system dynamics with arbitrary initial conditions were used. Ohm's law was used in place of the actuator dynamics. The MB tension was set to medium and the EM gap distance was set to 80 mm. The damping was chosen based on the characterization in Section 2.5.3.

The simulation results for the QP delayed control are shown in Figure 3.15. In general, the system was stable and the states decayed quickly. The QP delayed control strategy was shown to be effective. However, two main sources of non-linearities in the system limit the control performance. First, the stiffness switching introduces a stiffness variation and, thus, a period variation. The high stiffness state corresponds to shorter periods and a low stiffness state corresponds to longer periods. To compensate for this variation, the average period given in equation (3.30) is used to determine the intentional delay. Second, the non-linear springs introduce a stiffness variation as a function of mass displacement. This variation causes difficulties in determining the intentional delay from equations (3.22) and (3.29). For larger vibrations, the period is shorter and, therefore, τ_c should be smaller.

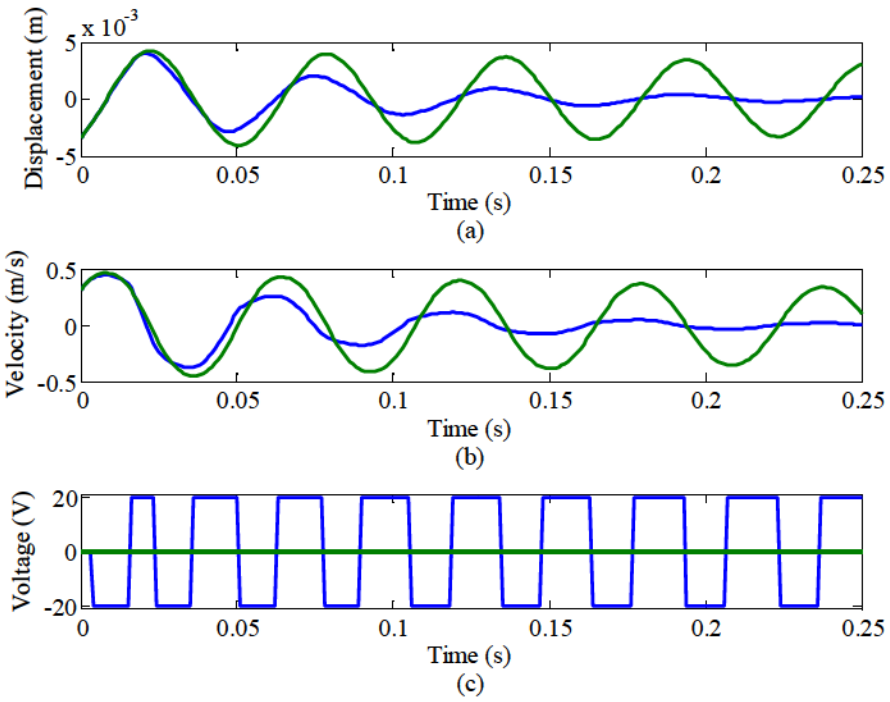

Figure 3.15 Simulated QP delayed inverted SS control (blue) and no-control (green) responses on damped non-linear system (a) displacement, (b) velocity, and (c) voltage

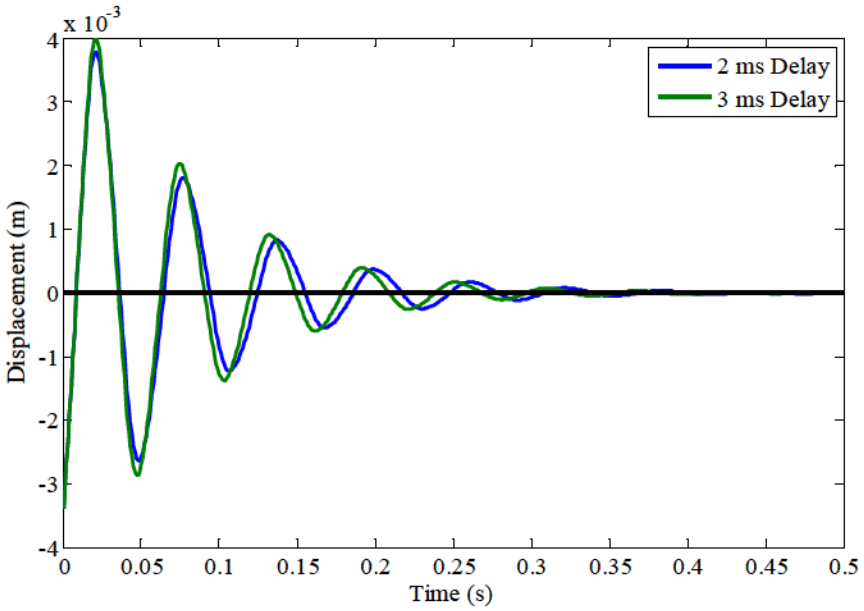

Figure 3.16 Simulated QP delayed inverted SS control for 2 ms (blue) and 3 ms (green) intentional delay

Figure 3.16 shows the simulated QP delayed inverted SS control displacement responses for two values of intentional time delays. The intentional delay based on the linear model (when vibration is small) was calculated to be 3 ms. It can be seen that at larger vibration amplitudes, the vibration suppression is better with τ_c = 2 ms. When the vibration amplitudes are small, the vibration suppression is slightly better with τ_c = 3 ms.

Figure 3.17 compares the different HP and QP delayed control simulation results. In general, the smaller the τ_c, the better the performance. Instability occurs if τ_c is too large (n = 2 HP delayed control). For non-linear system, a large intentional delay may cause instability problems due to the variation in period across different vibration amplitudes. In general, this method is better suited for linear systems where the natural periods are relatively constant.

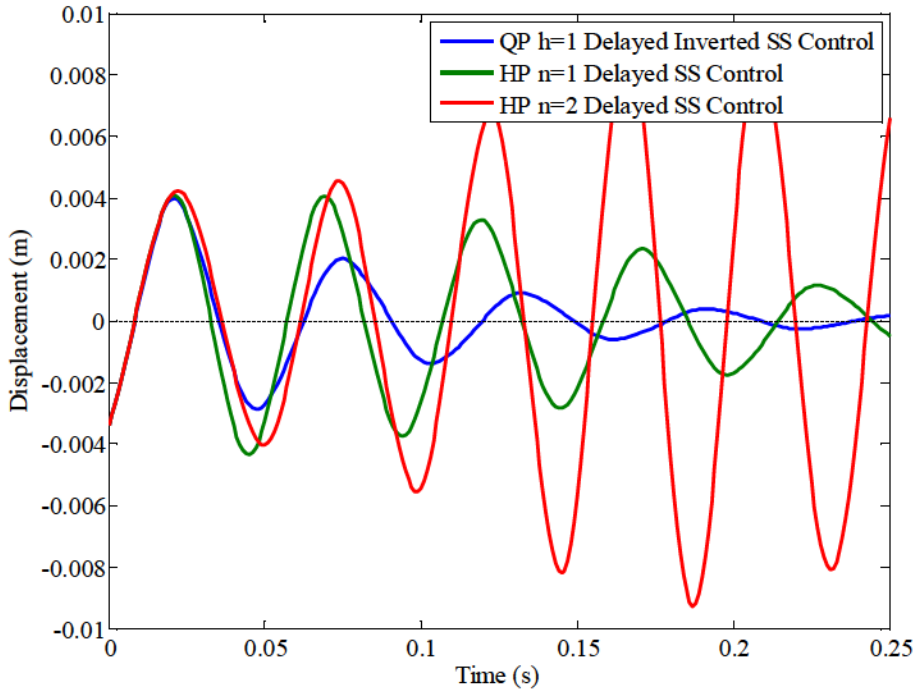

Figure 3.17 Simulated QP control (blue) HP control (n=1) (green) and HP control (n=2)

3.3 Dynamics of the EM Actuators

3.3.1 SS Control of the Non-Linear System with the EM Inductance

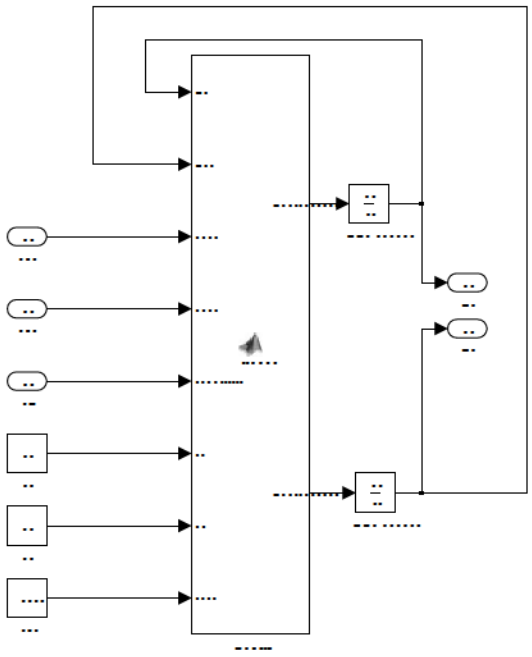

Figure 3.18 Simulink block diagram of the EM dynamics

A series of simulations based on the characterization in Section 2.8 were conducted to examine the dynamics of the EM, in particular, the inductance. The non-linear stiffness system dynamics with arbitrary initial conditions were used. The EM dynamics based on the circuit shown in Figure 2.24 were used. The Simulink block diagram of the EM dynamics is shown in Figure 3.18. The MB tension was set to medium and the EM gap distance was set to 80 mm. The damping was chosen based on the characterization in Section 2.5.3.

The simulation results are shown in Figure 3.19. It can be seen that the system is stable and, at best, decays slightly faster than the no-control case. It is evident that the inductance significantly slows the EM current response; therefore, the stiffness switching is not instantaneous. It is important to note that the frequency of stiffness switching is four times the frequency of vibration based on the SS strategy. That is, the stiffness switches four times per period of vibration. Therefore, any gradation in the stiffness switching is detrimental to the SS control performance. This effect is especially true for high frequency systems. The current

response assumes a triangular waveform. The triangular peaks only reach -0.2 to 0.2 A. For comparison, the incoming control voltages to the EMs switch from -20 to 20 V , which is a maximum of -1.5 to 1.5 A based on Ohm's law. Roughly, only 13% of the maximum current is effectively used. A reduced EM current variation corresponds to a reduced stiffness variation. The end result is a reduction in vibration suppression performance.

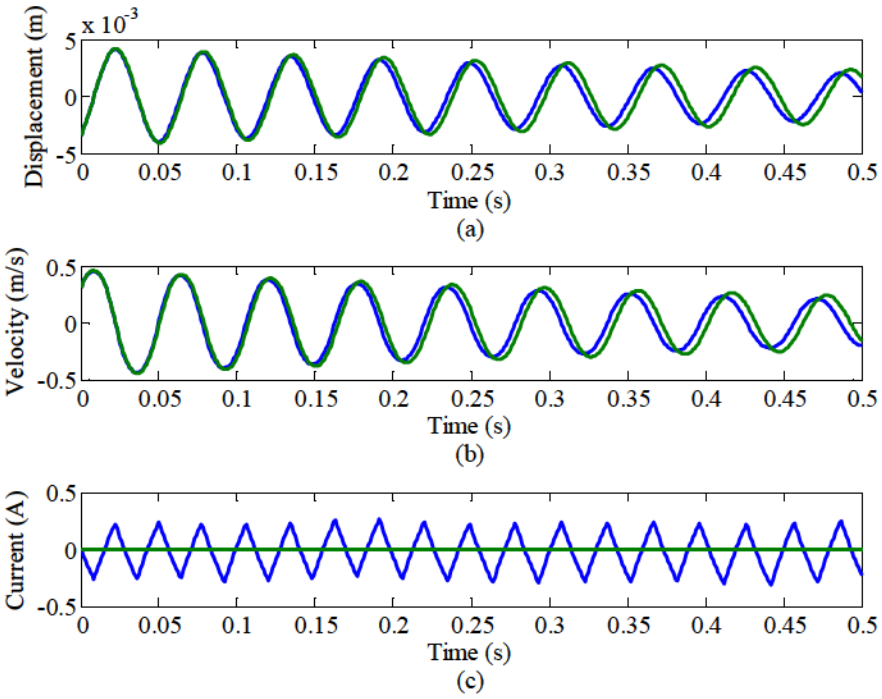

Figure 3.19 Simulated SS control (blue) and no-control (green) responses on damped non-linear system with EM dynamics (a) displacement, (b) velocity, and (c) voltage

3.3.2 Different Experimental Configurations

Different configurations of the experimental setup may increase the EM current variation, and, therefore, improve the performance of the system. One way is to use a set of EM actuators with low inductance. In general, however, an EM with low inductance may correspond to lower EM strength. Another way is to decrease the EM gap distance and thereby increase the EM force on the PM. Additionally, the MB tension may be reduced to increase the natural period. A long natural period will allow more time for the EM to reach higher current magnitudes. However, a longer natural period also means a lower frequency of stiffness switching. These ideas are investigated in the following subsection.

A series of simulations were conducted to investigate the effects of EM inductance using different experimental configurations. The objective is to determine configurations that maximize vibration suppression. The simulations were executed based on the setup in Section 3.3 with each simulation configured slightly differently. Figure 3.20 shows the SS control with the SS spring configured to EM_B. It is observed that the stiffness switching is slightly faster and the current reaches slightly higher magnitudes (-0.6 A to 0.6 A). However, the relative EM_B strength is too to weak to show a significant improvement in amplitude reduction. Figure 3.21 shows the SS control with the EM gap distance configured to 70 mm. It is observed that there is a slight improvement in amplitude reduction due to the increased force of the EMs on the PM. The current variation remains the same. Figure 3.22 shows the SS with MB tension configured to low. It is observed that the period is longer which allows time for the EM current variation to be higher (-0.25 A to 0.25 A). In general, these changes create slight improvements to the overall performance. The improvements are, however, not enough for the EM to be an effective SS actuator. The EM inductance proves to be one of the biggest limitations of using EMs as the SS actuator.

Therefore, an ideal SS actuator should have fast switching times, large stiffness variation, and low energy costs. A piezoelectric actuator possesses these characteristics and may be a possible choice [27]. Such an actuator can achieve effective vibration suppression (similar to Figure 3.8). Other SS mechanisms are discussed in Section 1.2.3. The implementation of another actuator device is beyond the scope of this thesis but may be an item for future work.

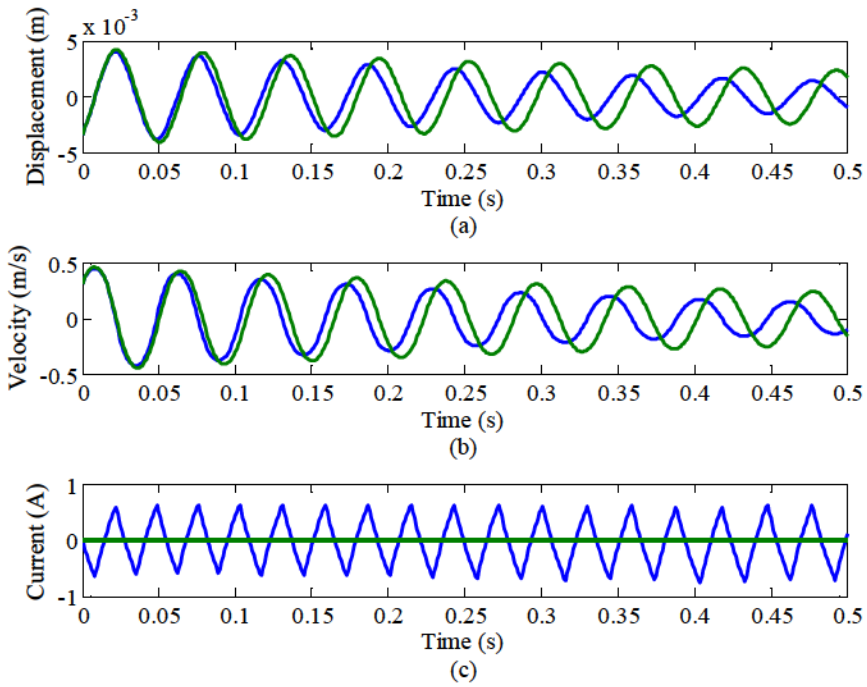

Figure 3.20 EM_B: simulated SS control (blue) and no-control (green) responses on damped non-linear system with EM dynamics (a) displacement, (b) velocity, and (c) voltage

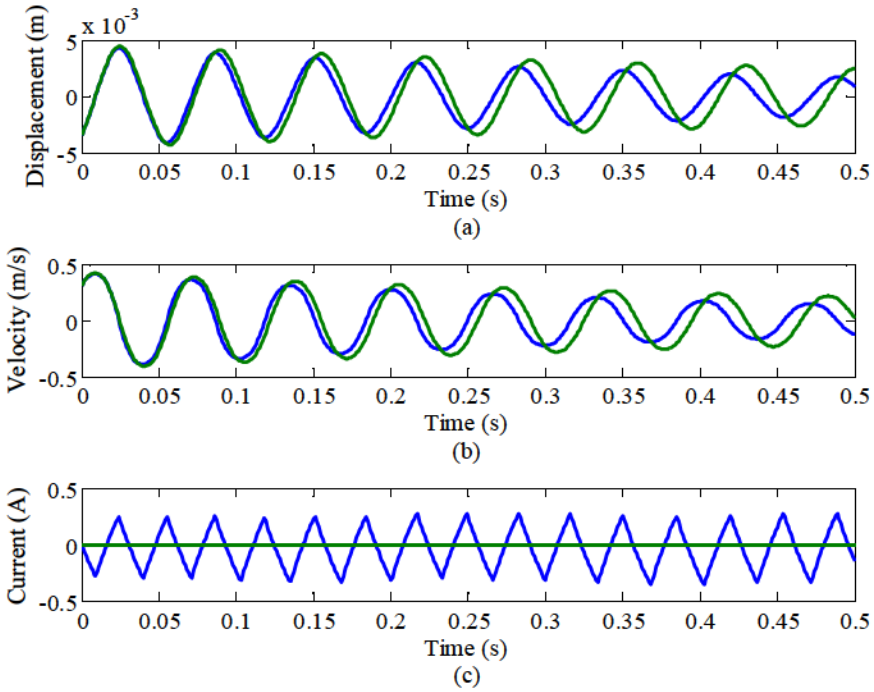

Figure 3.21 EM gap distance 70 mm: simulated SS control (blue) and no-control (green) responses on damped non-linear system with EM dynamics (a) displacement, (b) velocity, and (c) voltage

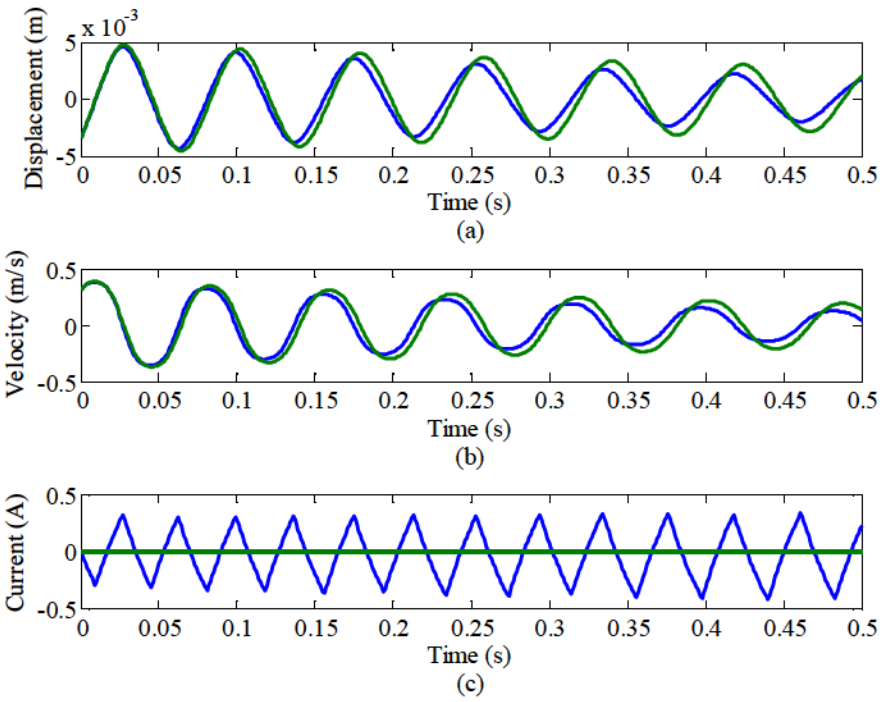

Figure 3.22 Low MB tension: simulated SS control (blue) and no-control (green) responses on damped non-linear system with EM dynamics (a) displacement, (b) velocity, and (c) voltage

3.4 Conclusions

In this chapter, the SS control, as presented in [23], was examined through theory and simulations. The concept, control law, stability, and control were investigated. It was shown that the SS control was effective at suppressing free vibration. From studying the SS mechanism, it was observed that vibration suppression was achieved through the dissipation of potential energy via stiffness reduction at the peaks of the mass displacements. Additionally, it was shown that the inverted SS control had the opposite effect; it caused vibration amplification.

In addition, the impact of time delay was studied. Time delay caused the stiffness to switch at inappropriate instances. However, it was shown that if the time delay was a multiple of half of the period, the control effort would be applied correctly and the system would be stable. On the other hand, if the time delay was an odd multiple of a QP, the control effort would be inverted and the system would be unstable. Using these properties, an intentional time delay was introduced to the existing system time delay such that the total time delay would be a multiple of the half of the period. This method was referred to as the HP delayed SS control or HP delayed

control for brevity. To achieve an even faster response, the SS was inverted and an intentional time delay was introduced such that the total time delay equaled an odd multiple of a quarter of the period. This method was referred to as the QP delayed inverted SS control or QP delayed control for brevity. Through simulations, both of these methods proved to be effective at overcoming the inherent time delay. One problem limited the performance of these methods. Due to the non-linearity of the system, the constant intentional delay could not compensate for the time delay of all amplitudes of vibration.

The effects of the dynamics of the EM actuators were also explored. It was shown that the inductance of the EM significantly slowed the EM current change and, thus, stiffness switching. Additionally, the EM inductance also reduced the effective current passing through the EMs. This effect was a huge factor in debilitating the performance of the SS control. Different configurations of the experimental setup were explored such as reducing the EM inductance, reducing the EM gap distance, or reducing the MB tensions. These configurations showed little improvement. In summary, this chapter laid the groundwork for the next step: the real-time implementation of the SS control.

Chapter 4 – Implementation of the SS Control

This chapter aims to implement the SS control strategy using the SDOF experimental apparatus characterized in Chapter 2. Section 4.1 presents the instrumentation, configuration, interface, filter selection, and experimental procedure. Section 4.2 presents the modified SS control laws for real-time implementation. Section 4.3 presents the experimental results for the direct application of the SS control. Section 4.4 presents the experimental results for the delayed control strategy and the effects of the EM dynamics. Section 4.5 presents the experimental results for different configurations of the gap distance, EM sets, and MB tension. Finally, Section 4.6 presents the conclusions.

4.1 Experimental Setup

4.1.1 Instrumentation and Configuration

The primary instruments used for these experiments include the sensor, computer, DAQ board, and power supplies. The position sensor is an optical reflex sensor (Wenglor CP24-MHT80) powered by an external power supply unit (PSU). The internal sensor filter setting was disabled and the voltage calibration was determined through the sensor data chart. The sensor was positioned at an angle to the mass. As a result, a correction factor was introduced to compensate for the angle. The voltage signal from the sensor was collected by the DAQ board (dSpace dS1102), which executes the analogue to digital conversion (ADC). The DAQ board is the hub for which signals are sampled and transmitted via the computer. The computer is a dedicated Pentium III PC used to interpret sensor signals and generate control signals. The control signals or the voltages applied to the EMs were sent to two individual power supplies

(Quanser UPM-2405) via the DAQ board which executes the digital to analogue conversion (DAC). These instruments are shown in Figure 4.1.

(a) (b) (c) (d)

Figure 4.1 Experimental instruments (a) Wenglor optical reflex position sensor (b) dSpace dS1102 DAQ board terminal block (c) dedicated PC (d) Quanser UPM 2405 PSU

4.1.2 Interface

The SS controller logic, sensor calibration, signal processing, and system parameters were programmed using the Simulink block diagrams in Matlab. The experiment execution and data collection were done through the custom graphical UI program, Control Desk. Simulink and Control Desk were linked using Matlab's Realtime Workshop. The sampling frequency used is 1000 Hz. A typical Control Desk program is shown in Figure 4.2 and the Simulink block diagram is shown in Figure 4.3.

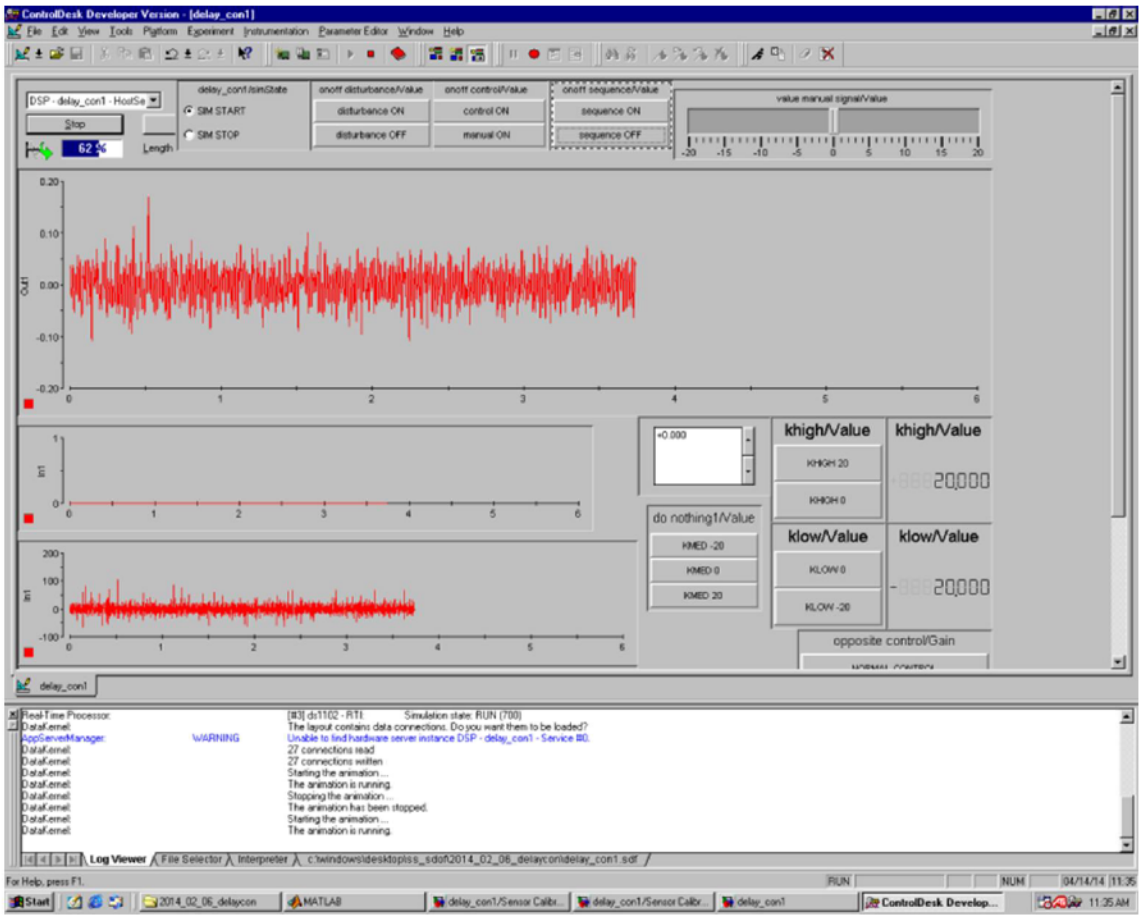

Figure 4.2 Typical Control Desk experiment interface

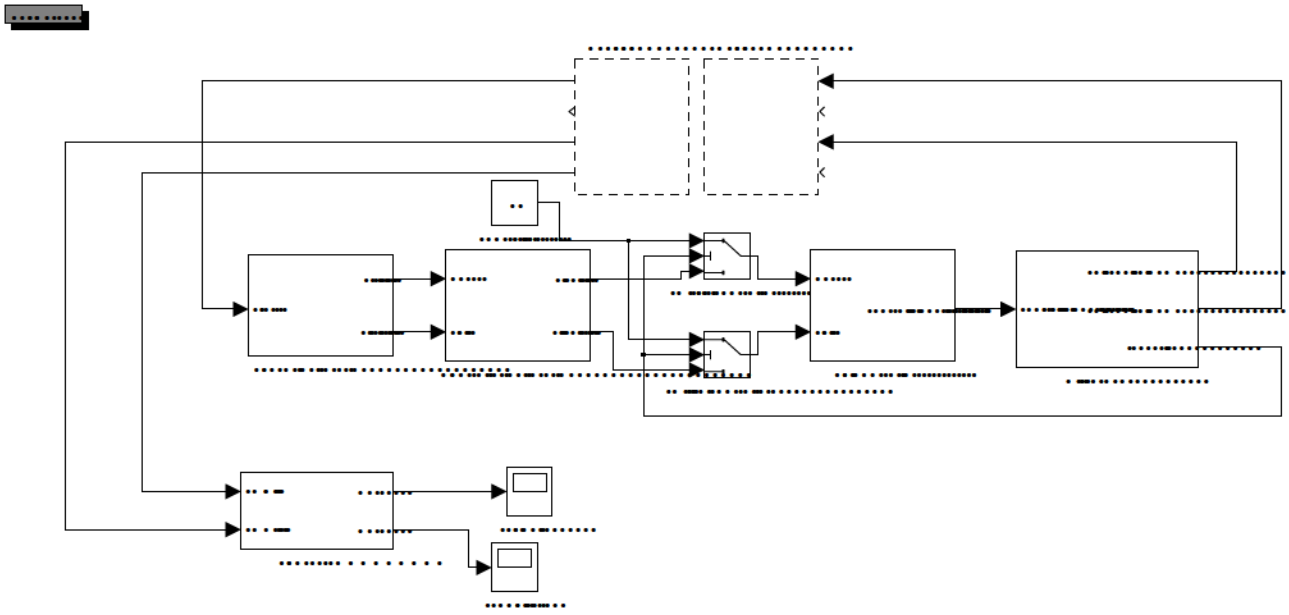

Figure 4.3 Simulink block diagram for experiments

4.1.3 Filter Selection

Noise, a random fluctuation in electrical signals, is present in all electronic circuits. Noise may be due to thermal energy at non-zero temperatures, semi-conductor defects, or circuit manufacturing quality [52]. In general, noise is undesirable as it may distort the feedback signals. Signal distortion may lead to an unintended application of the control logic. To overcome this issue, low pass filters are used to eliminate the noise above the low pass cutoff frequency. Additionally, high pass filters are employed to remove the direct current (DC) bias.

The noise from the position signal in the experiment creates undesirable effects to the SS control logic. Additionally, taking the derivative of the noisy signal (to determine velocity) amplifies the noise. The sharp fluctuations in the velocity and position signal cause the appearance of random high frequency vibration. The SS controller interprets the noisy signal as rapid direction changes in the mass motion. As a result, the SS controller applies the corresponding stiffness switching which invariably excites the system.

To deal with signal noise, a series of low pass and high pass filters were employed. The signal filter block diagrams are shown in Figure 4.4. The position signal was filtered by a first order low pass filter with a cut-off frequency of 70 Hz twice. The velocity signal was determined by differentiating the once filtered position signal. The velocity signal was filtered again using a first order low pass filter with a cut-off frequency of 70 Hz. Both the position and velocity signals were filtered by a first order high pass filter with a cut-off frequency of 5 Hz to remove any DC bias.

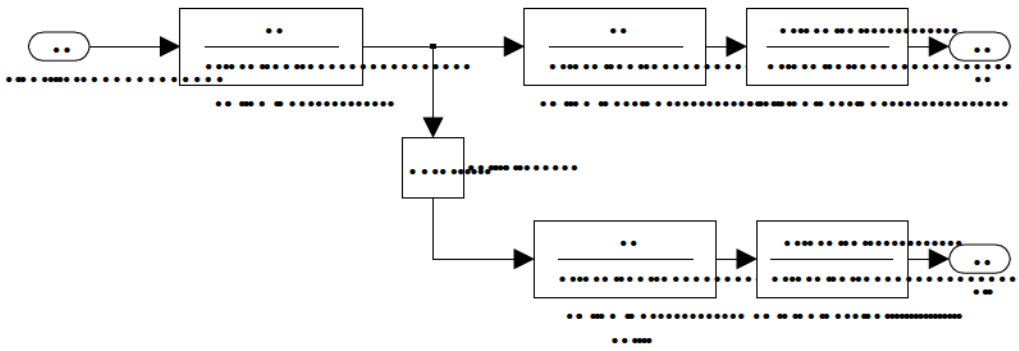

Figure 4.4 Signal filters

The high and low pass filters distorts the original signal in two ways. First, the signal amplitudes are attenuated slightly (approximately 10% when the amplitudes are large). Since the SS control logic is independent of the signal magnitudes, this distortion is not considered relevant. Second, the filters introduce a phase lag and phase lead. The lead and lag partially cancel each other. The net lag can be seen in Figure 4.5 which was determined to be approximately 2 to 3 ms.

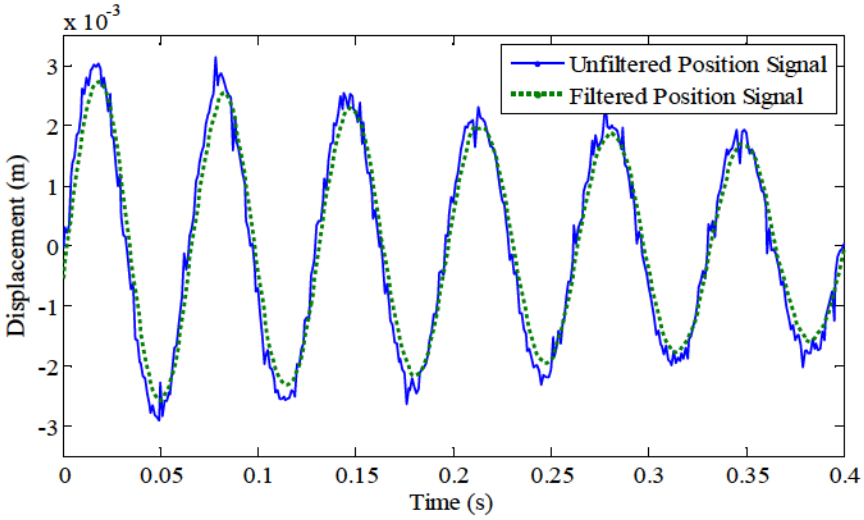

Figure 4.5 Comparison of filtered signal and unfiltered signal

4.1.4 General Experimental Procedure

The experimental procedure is as follows. Two separate opposing 16 Hz sinusoidal voltage signals were sent to EM_1 and EM_2 through the amplifiers. As the signs of the currents applied to the EMs were different, a sinusoidal force was exerted on the mass. The magnitude of the signals was different for different configurations. After the mass vibration has reached steady state, the sinusoidal signals were terminated. At this point, the SS control logic was implemented. The data was collected to the computer for post processing. In all of the following experiments, a sampling frequency of 1000 Hz was used. The resolution time was 1 ms.

4.2 Modified SS Control Laws

4.2.1 Direct Control Law

An additional medium stiffness state, k_{med}, is introduced to the SS control law presented in Section 3.1.1. This state is activated when the position or velocity enters a small tolerance region around the equilibrium. There are several reasons why this state is necessary for real-time implementation. First, vibration theoretically never reaches zero via the SS control; the stiffness switching will occur indefinitely. Introducing k_{med} allows the actuators to turn off when the vibration is sufficiently low, thus, allowing the system to naturally decay. Using k_{med} instead of k_{high} also conserves energy. Additionally, noise causes the SS control logic to randomly switch when the vibrations are small enough to be disguised by noise. This effect may cause parametric excitation. Introducing k_{med} prevents this problem.

The modified SS control law is defined as

$$k(t) = \begin{cases} k_{high} & \text{for } x(t)\dot{x}(t) > 0 \\ k_{low} & \text{for } x(t)\dot{x}(t) < 0 \\ k_{med} & \text{for } x(t) < |\varepsilon_1| \text{ and } \dot{x}(t) < |\varepsilon_2| \end{cases} \tag{4.1}$$

where ε_1 and ε_2 are the saturation points for this control algorithm.

4.2.2 Delayed Control Laws

The modified HP delayed SS control law is defined as

$$k(t+\tau_c) = \begin{cases} k_{high} & \text{for } x(t)\dot{x}(t) > 0 \\ k_{low} & \text{for } x(t)\dot{x}(t) < 0 \\ k_{med} & \text{for } x(t) < |\varepsilon_1| \text{ and } \dot{x}(t) < |\varepsilon_2| \end{cases} \tag{4.2}$$

where the HP intentional delay is defined as

$$\tau_c = n\frac{1}{2}T - \tau_d, \quad \tau_c \geq 0 \tag{4.3}$$

The modified QP delayed inverted SS control is defined as

$$k(t+\tau_c)=\begin{cases} k_{high} & \text{for } x(t)\dot{x}(t)<0 \\ k_{low} & \text{for } x(t)\dot{x}(t)>0 \\ k_{med} & \text{for } x(t)<|\varepsilon_1| \text{ and } \dot{x}(t)<|\varepsilon_2| \end{cases} \tag{4.4}$$

where the QP intentional delay is defined as

$$\tau_c = h\frac{1}{4}T-\tau_d,\ \ \tau_c \geq 0 \tag{4.5}$$

4.3 Direct SS Control

An experiment was conducted according to the general procedure described in Section 4.1.4. The MB tension was tuned to medium and the EM gap distance was set to 80 mm. The experimental results are shown in Figure 4.6. The states of the system are unbounded and the system vibration is amplified. This observation is congruent with the simulation results in Section 3.1.6. Inherent delays in the system cause inappropriate stiffness switching and, therefore, instability. The direct application of the SS control is ineffective due to inherent delays in the system.

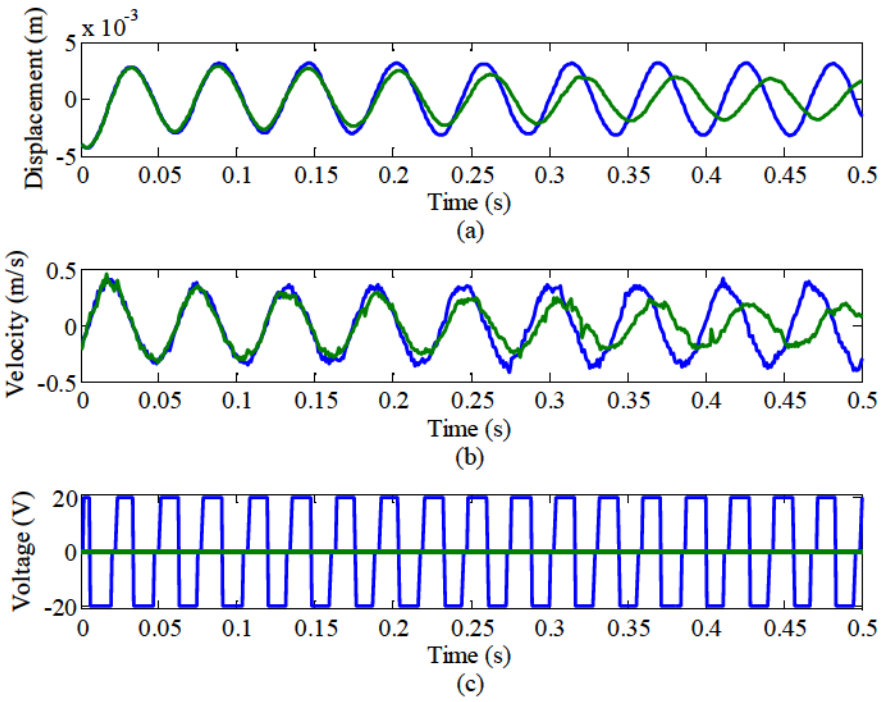

Figure 4.6 Experimental displacement (a), velocity (b), and voltage (c) response for direct control (blue) vs. no control (green)

4.4 Delayed SS Control

4.4.1 Experimental Intentional Delay

A series of experiments were conducted to validate the delayed SS control strategies. The procedure presented in Section 4.1.4 was followed. The MB tension was tuned to medium and the EM gap distance was set to 80 mm. The experiment was repeated for several values of intentional delay τ_c. By finding the best amplitude reduction of the control responses, the experimental τ_c was determined. This procedure was repeated for both QP and HP delayed control strategies. The estimated τ_c and experimental τ_c are summarized in Table 4.1. A typical HP delayed control displacement response for different values of τ_c are shown in Figure 4.7. Note that for higher amplitude vibrations, a lower τ_c is slightly more effective than the estimated τ_c. This effect is due to the dynamics of the non-linear stiffness. For lower amplitude vibrations, the estimated τ_c is optimal. In general, there is strong agreement between the estimated and experimental τ_c. This observation supports the delayed SS models.

Table 4.1 Comparison of estimated and experimental intentional delays

Delay Strategy	Estimated τ_c (s)	Experimental τ_c (s)
HP SS Control	0.018	0.018
QP SS Control	0.003	0.002

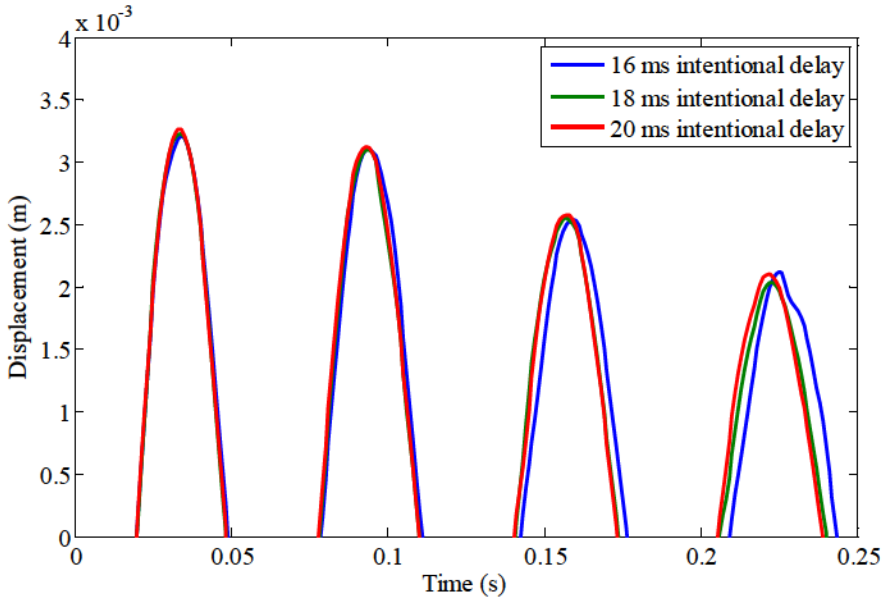

Figure 4.7 Displacement response for HP delayed inverted SS control for different intentional delays

4.4.2 Delayed SS Control Implementation

A series of simulations were conducted using the experimental τ_c values for the delayed SS control law. Figure 4.8 and Figure 4.9 show the response of the QP and HP delayed control strategies, respectively. For convenience, the control response (shown in blue) is compared against the no-control response (shown in green). In general, the faster the controller is able to respond, the better the performance. The QP delayed control is better than the HP delayed control. The overall performances of the SS control strategies, however, are poor compared to the simulations in Section 3.2.3. In the best case, the delayed control strategies are stable and decay the system response slightly faster than no-control case. It is expected, based on the simulations in Section 3.3.1, that the EM dynamics are the limiting factor in the performance of the SS control.

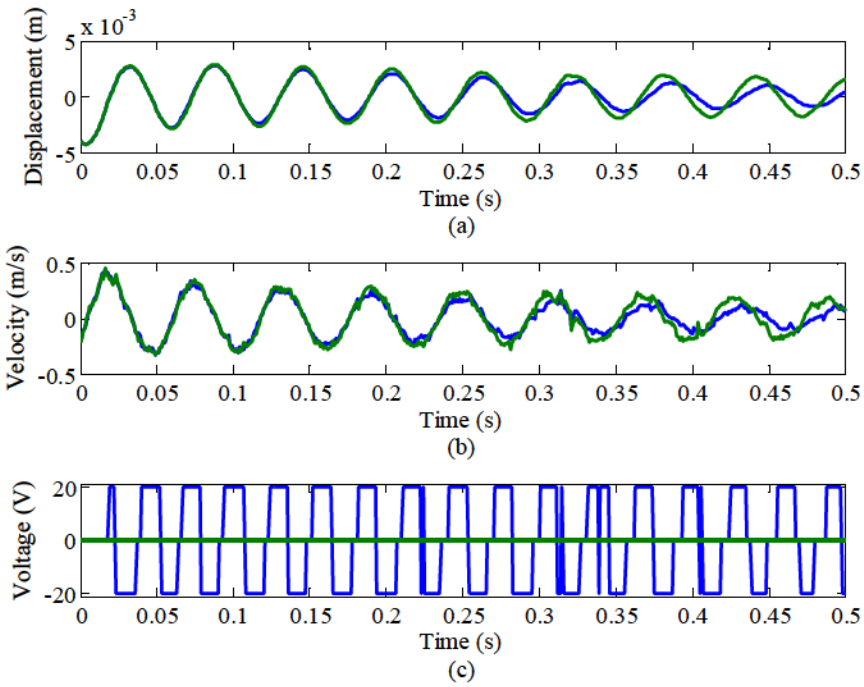

Figure 4.8 Experimental displacement (a), velocity (b), and voltage (c) response for HP control (blue) vs. no control (green)

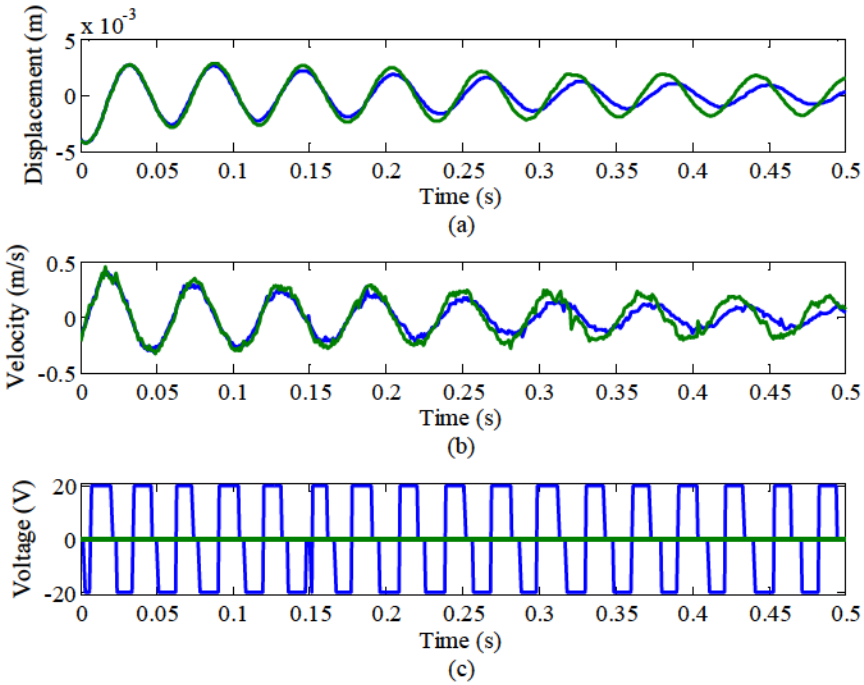

Figure 4.9 Experimental displacement (a), velocity (b), and voltage (c) response for QP control (blue) vs. no control (green)

4.4.3 Effect of the EM Inductance

In order to study the effects of the EM inductance, a 1 Ω power resistor was attached in series to each EM. The current in the circuit was determined by measuring the power resistor voltage and applying Ohm's law (assuming that the inductance of the power resistor is negligible). The voltage was measured directly by the DAQ system. The QP delayed control experiment was repeated with the actual current measurements. The experimental results are shown in Figure 4.10. Additionally, a comparison of the control signal and the measured current is shown in Figure 4.11. The results confirm a major problem with the EM actuators for the SS control. The EM inductance causes the current to assume a triangular wave form and the stiffness switching is not instantaneous. Additionally, the peaks of the waves reach roughly -0.2 to 0.2 A, only 13% of the maximum predicted current of -1.5 to 1.5 A. The EM inductance effectively limits the amount of current being applied to the EMs. In turn, this limits the stiffness variation and, hence, the vibration suppression. These experimental results agree with the simulation results in Section 3.3.1.

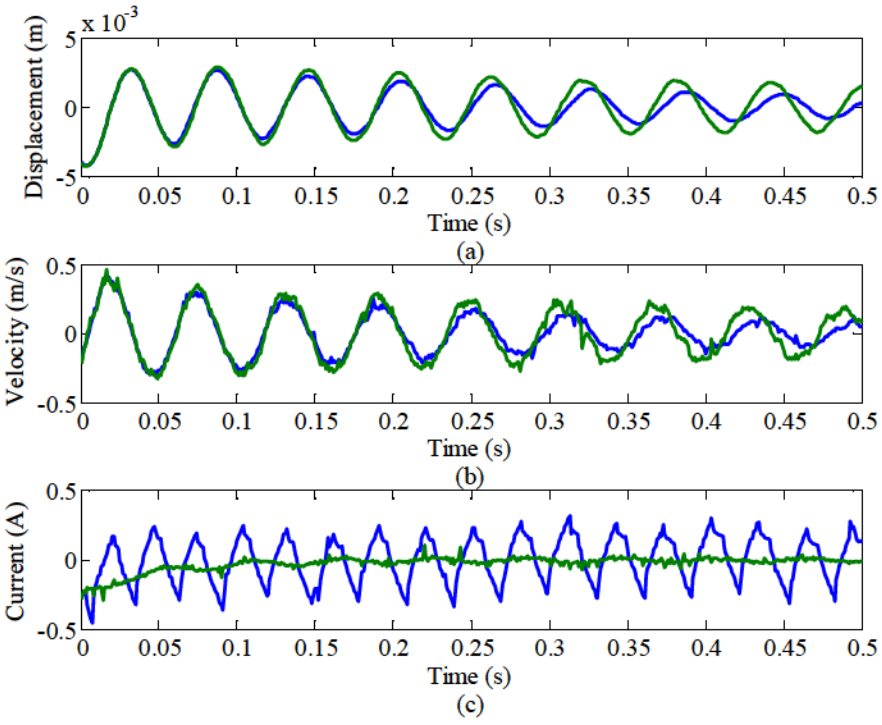

Figure 4.10 Experimental displacement (a), velocity (b), and current (c) response for QP control (blue) vs. no control (green)

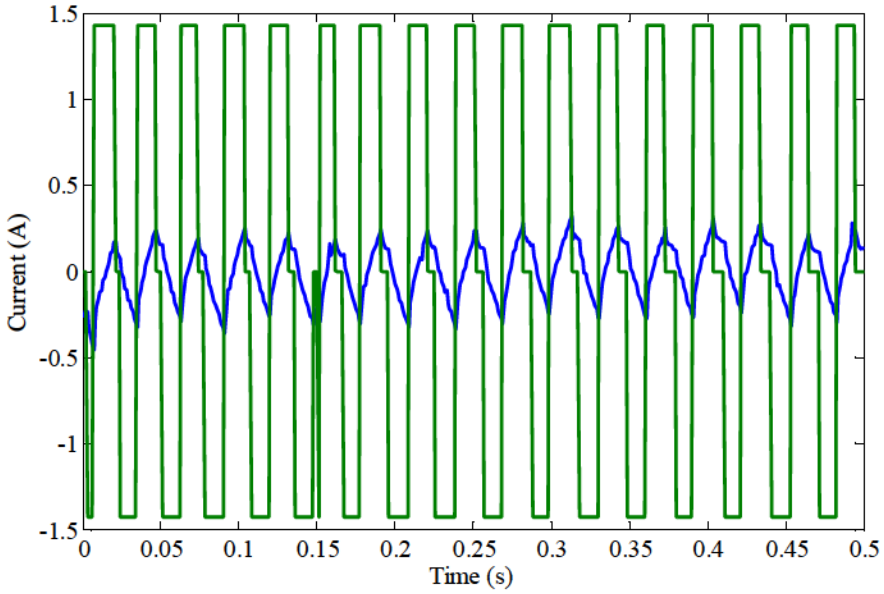

Figure 4.11 Comparison of actual measured current (blue) and expected current without inductance considerations (green)

4.5 Control for Different Configurations

Essentially, the EM inductance inhibits the SS control performance by reducing the effective stiffness variation Δk. In lieu of the EM dynamics, there are several ways to reconfigure the system and increase the effective Δk. The EM actuators may be changed to a different set with lower inductance. Additionally, the EM gap distance may be reduced to increase the magnetic strength of the EM on the PM. Also, decreasing the MB tension may increase the period, allowing the EM current more time to reach higher magnitudes. These configurations are tested in the remaining subsections.

4.5.1 EM Gap Distance and MB Tension

The experiment in Section 4.4.3 was repeated for an EM gap distance of 70 mm. The results are shown in Figure 4.12. It is observed that the amplitude reduction is slightly better for a smaller gap distance. Decreasing the gap distance increases the softening effect of the magnetic spring thereby decreasing the natural frequency. This allows the EM slightly more time to reach higher currents. The EM current variation is, at the best, approximately 0.6 A (-0.3 A to 0.3 A), more than the 0.4 A (-0.2 A to 0.2 A) current variation for the 80 mm EM gap distance

experiment. Decreasing the gap distance also increases the magnetic force of the EMs. Therefore, the current variation would be amplified at closer gap distances.

In general, decreasing the EM gap distance reduces the natural frequency via the magnetic spring, allows more time for the current to reach higher values, and increases the change in effective stiffness. However, decreasing the EM gap distance also increases the non-linearity of the system and may not allow enough room for the mass to vibrate without physically contacting the actuators.

Also, the experiment in Section 4.4.3 was repeated for the low MB tension case. The results are shown in Figure 4.13. Reducing the MB tension directly reduces the stiffness and, thus, increases the period. An increase in period will allow the EM more time to reach higher current values. The EM current variation is, at best, approximately 0.7 A (-0.35 A to 0.35 A), 23% of the maximum current variation. It is observed that there is an improvement, however small, in the response as compared to the medium MB tension case. Reducing the gap distance is more effective, as it also increases the effective EM force on the PM.

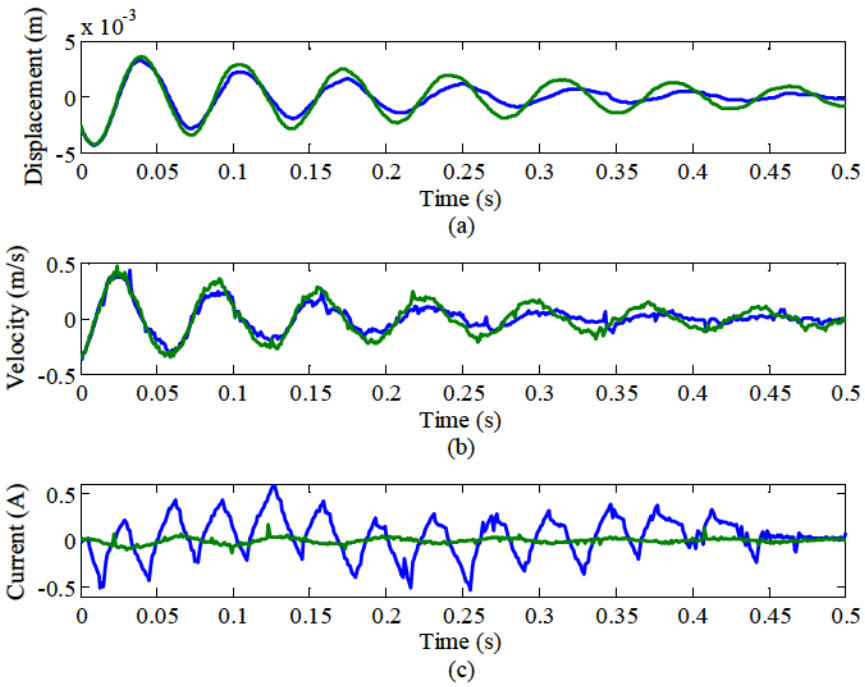

Figure 4.12 Experimental displacement (a), velocity (b), and current (c) response for QP control (blue) vs. no control (green) at EM gap distance of 70 mm

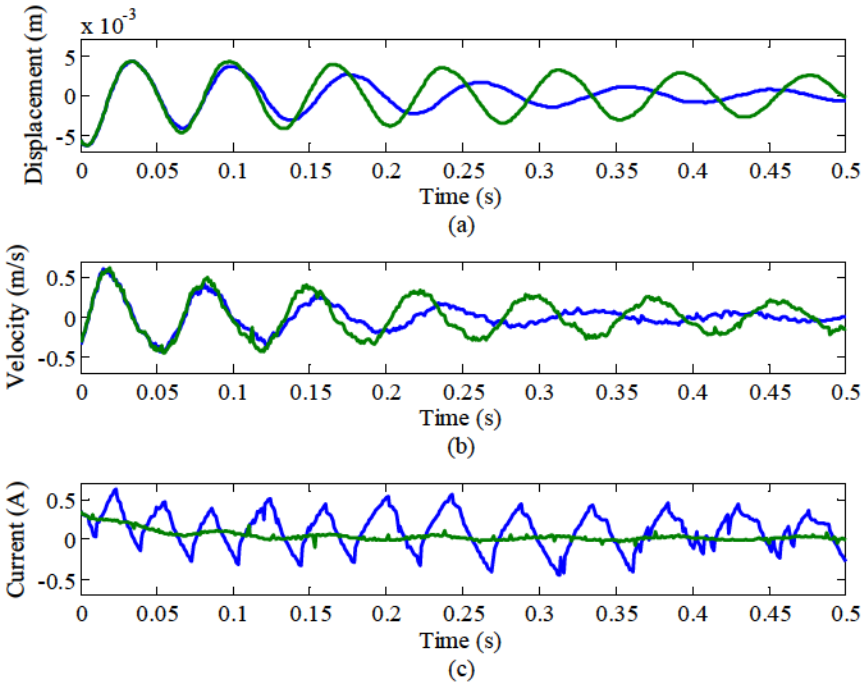

Figure 4.13 Experimental displacement (a), velocity (b), and current (c) response for QP control (blue) vs. no control (green) using low MB tension

4.5.2 EM Set B

The experiment in Section 4.4.4 was repeated for EM_B. The results are shown in Figure 4.14. EM_B has an inductance value of 0.16 H, much lower than EM_A inductance of 0.65 H. The variation in current is roughly 2 A (-1 A to 1 A), 40% of the maximum current variation. Lower inductance allows a significantly higher percentage of the EM strength to be applied. However, there is a tradeoff to lower inductance. EM_B has a weaker magnetic flux. Despite a larger variation in current, the EM_B current actually produces lower magnetic forces. Therefore, the ideal EM actuator must have a low inductance and a strong magnetic flux.

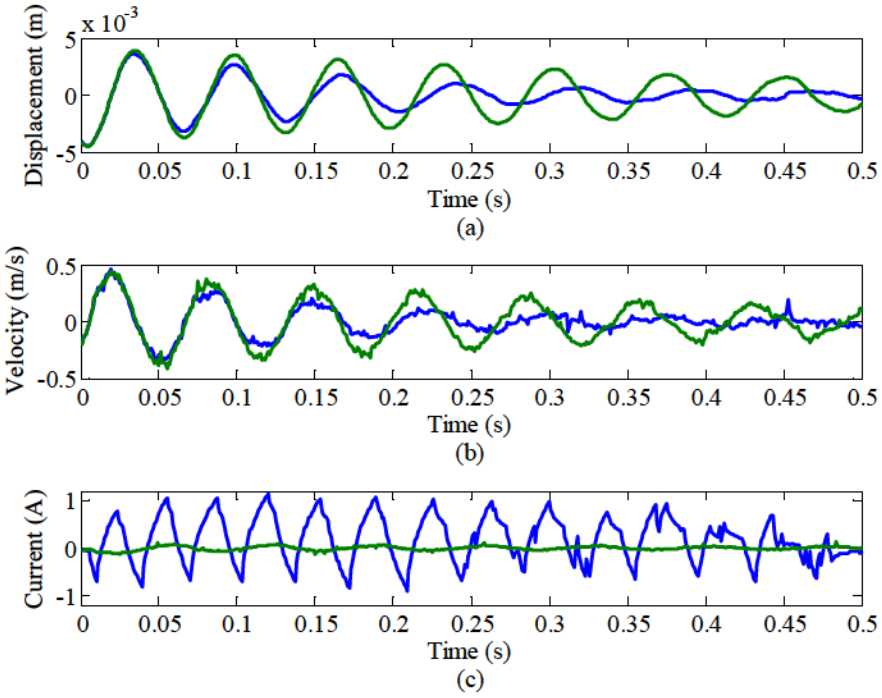

Figure 4.14 Experimental displacement (a), velocity (b), and current (c) response for QP control (blue) vs. no control (green) using EM_B

4.6 Conclusions

In this chapter, the real time implementation of the SS control strategy was presented in detail. The experimental setup and configuration were described and the SS control law was modified for real time implementation. An off state, k_{med}, was introduced to turn the control off when the vibrations were below a threshold, allowing the system to naturally decay. This modification also conserves power and prevents the SS control from misinterpreting static noise as disturbances.

The direct application of the SS control was verified. As the simulations predicted, the SS control was shown to be unstable due to the inherent time delays. Additionally, the SS delayed control strategies were tested and verified. An experiment was conducted to find the most appropriate τ_c based on the amplitude reduction. It was shown that, in general, the experimental and estimated τ_c values agreed. However, due to the non-linearity of the system, τ_c values slightly lower than the estimated τ_c worked better for larger vibration amplitudes. This was also congruent with the predictions made in Section 3.2.3. Overall, the delayed SS control strategies were verified experimentally. Unfortunately, the amplitude reduction was not as great as expected. To understand why, the EM current was measured during the control. It was shown that the EM inductance severely limited the effective current being applied to the EMs. This limited the effective force of the EM and therefore the stiffness variation.

Different configurations were tested to increase the effectiveness of EM force on the PM (in order to ultimately increase the effective stiffness variation). A series of experiments using different configurations of the EM gap distance, EM sets, and MB tension were conducted. Decreasing the natural frequency by decreasing the MB tension and EM gap distance showed little improvement. Physically decreasing the natural frequency of the system for this effect is not ideal in many real systems. The overall tradeoff between decreasing frequency and increasing performance was shown to be poor. Lowering the EM inductance was shown to be a better option, only if it was not at the expense of the EM flux. The ideal EM actuator was postulated to have very low inductance but a large magnetic flux.

Chapter 5 – SS Vibration Control of a 2DOF System

Most real systems have more than one degree of freedom (DOF). Thus, it is desirable to investigate the SS control strategy for 2DOF systems in order to extend the area of applications. This chapter presents a preliminary investigation of the SS control for a 2DOF system. In Section 5.1, the dynamic models are introduced and the equations of motion are presented. In Section 5.2, the 2DOF version of the direct and delayed SS control law is presented. In Section 5.3, simulations are conducted to examine the SS control on the linear, non-linear, and time delay models. Finally, in Section 5.4, the conclusions are presented.

5.1 Dynamic Model of a 2DOF System

The 2DOF system under consideration is made up of two individual SDOF systems coupled by a beam. The schematic of this system is shown in Figure 5.1 and the FBD is shown in Figure 5.2. The symbols m, k, c, and l are the mass, stiffness, damping constant, and lengths respectively. F_s and F_d are the generalized spring force and damping force, respectively. The subscripts *1*, *2*, and *b* refer to the first system, second system, and beam. $x_1(t)$, $x_2(t)$, $x_G(t)$, and $\theta(t)$ are different coordinates for the translation of the first system, translation of the second system, translation of the combined system at the center of gravity (C.G.), and the rotation of the combined system at the C.G. with respect to the horizontal.

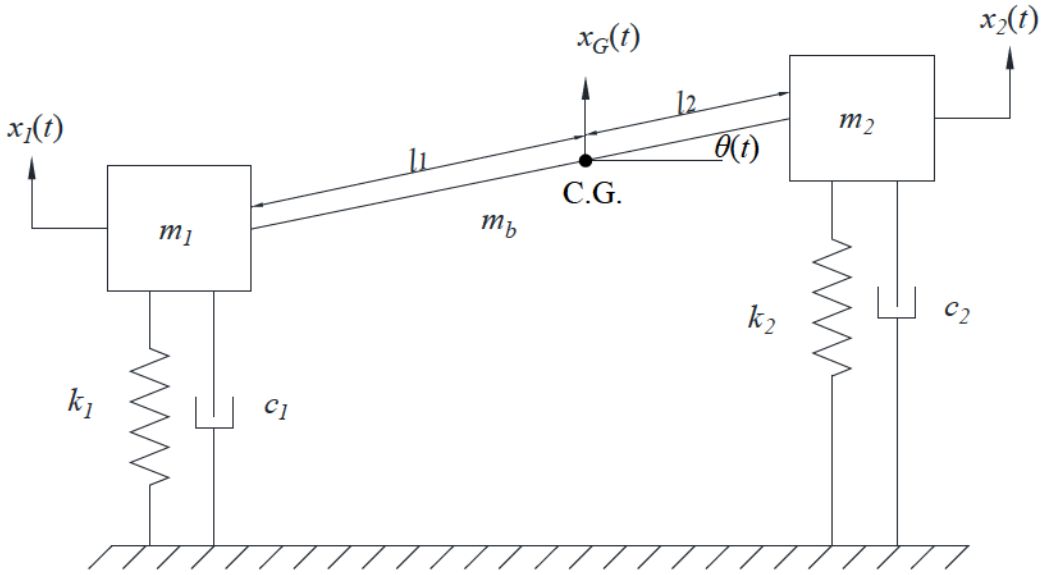

Figure 5.1 Schematic of 2DOF system

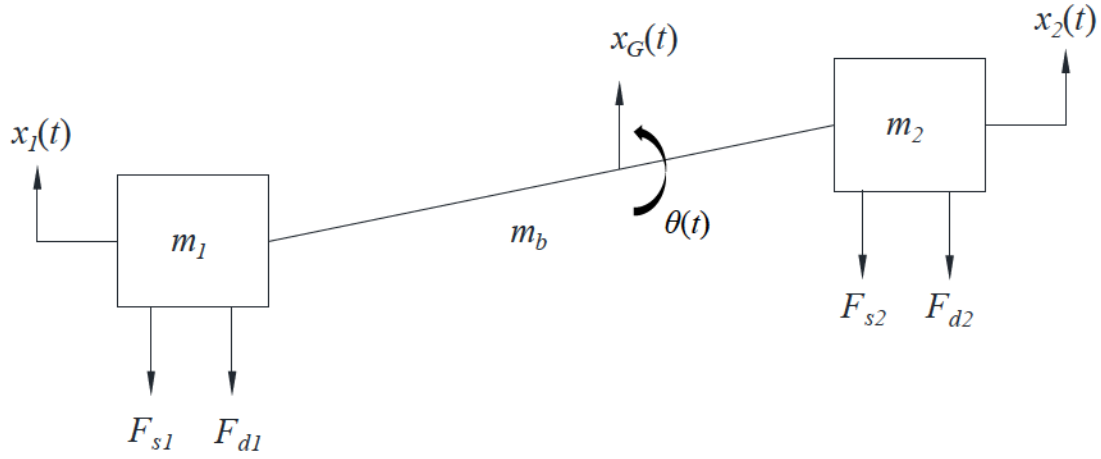

Figure 5.2 Free body diagram (FBD) of 2DOF system

For the full derivation, refer to Appendix A. The equations of motion are

$$\ddot{x}_1 = -\left(\frac{F_{s1}+F_{s2}+F_{d1}+F_{d2}}{m_t}\right)-\left(\frac{l_1\left(F_{s1}l_1+F_{d1}l_1-F_{s2}l_2-F_{d2}l_2\right)}{I_G}\right) \tag{5.1}$$

$$\ddot{x}_2 = -\left(\frac{F_{s1}+F_{s2}+F_{d1}+F_{d2}}{m_t}\right)+\left(\frac{l_2\left(F_{s1}l_1+F_{d1}l_1-F_{s2}l_2-F_{d2}l_2\right)}{I_G}\right) \tag{5.2}$$

where m_t and l_t are defined as

$$\begin{aligned} m_t &= m_1 + m_2 + m_b \\ l_t &= l_1 + l_2 \end{aligned} \tag{5.3}$$

The moment of inertia, I_G, is determined by

$$\begin{aligned} x_{CG} &= \sum_i \frac{m_i r_i}{m_i} = \frac{m_1 r_1 + m_2 r_2 + m_b r_b}{m_t} \\ I_G &= \frac{1}{12}\left(l_t^2 + w_b^2\right) + m_1 r_1^2 + m_2 r_2^2 + m_b \left(x_{CG} - r_b\right)^2 \end{aligned} \tag{5.4}$$

where r_1, r_2, and r_b are the distances of the respective masses to the origin. If the origin is set at m_1, then $r_1 = 0$, $r_2 = l_t$, and $r_b = l_t/2$.

Substituting viscous damping and a linear spring force, the equations of motion can be written as

$$\begin{bmatrix} \ddot{x}_1 \\ \ddot{x}_2 \end{bmatrix} = \begin{bmatrix} -\frac{c_1}{m_t} - \frac{c_1 l_1^2}{I_G} & -\frac{c_2}{m_t} + \frac{c_2 l_1 l_2}{I_G} \\ -\frac{c_1}{m_t} + \frac{c_1 l_1 l_2}{I_G} & -\frac{c_2}{m_t} - \frac{c_2 l_2^2}{I_G} \end{bmatrix} \begin{bmatrix} \dot{x}_1 \\ \dot{x}_2 \end{bmatrix} + \begin{bmatrix} -\frac{k_1}{m_t} - \frac{k_1 l_1^2}{I_G} & -\frac{k_2}{m_t} + \frac{k_2 l_1 l_2}{I_G} \\ -\frac{k_1}{m_t} + \frac{k_1 l_1 l_2}{I_G} & -\frac{k_2}{m_t} - \frac{k_2 l_2^2}{I_G} \end{bmatrix} \begin{bmatrix} x_1 \\ x_2 \end{bmatrix} \tag{5.5}$$

The equations can also be written for modal analysis (in terms of the translation and rotation at the C.G.) as

$$\begin{bmatrix} 0 \\ 0 \end{bmatrix} = \begin{bmatrix} m_t & 0 \\ 0 & I_G \end{bmatrix} \begin{bmatrix} \ddot{x}_G \\ \ddot{\theta} \end{bmatrix} + \begin{bmatrix} c_1 + c_2 & l_2 c_2 - l_1 c_1 \\ l_2 c_2 - l_1 c_1 & l_2^2 c_2 + l_1^2 c_1 \end{bmatrix} \begin{bmatrix} \dot{x}_G \\ \dot{\theta} \end{bmatrix} + \begin{bmatrix} k_1 + k_2 & l_2 k_2 - l_1 k_1 \\ l_2 k_2 - l_1 k_1 & l_2^2 k_2 + l_1^2 k_1 \end{bmatrix} \begin{bmatrix} x_G \\ \theta \end{bmatrix} \tag{5.6}$$

In addition, equation (5.5) can be re-written in state space form. First, the state variables are introduced as

$$\begin{aligned} h_1 &= x_1 \\ h_2 &= x_2 \\ h_3 &= \dot{x}_1 = \dot{h}_1 \\ h_4 &= \dot{x}_2 = \dot{h}_2 \end{aligned} \tag{5.7}$$

The state space of the system is given as

$$\dot{h} = Ah = \begin{bmatrix} \dot{h}_1 \\ \dot{h}_2 \\ \dot{h}_3 \\ \dot{h}_4 \end{bmatrix} = \begin{bmatrix} 0 & 0 & 1 & 0 \\ 0 & 0 & 0 & 1 \\ -\frac{k_1}{m_t} - \frac{k_1 l_1^2}{I_G} & -\frac{k_2}{m_t} + \frac{k_2 l_1 l_2}{I_G} & -\frac{c_1}{m_t} - \frac{c_1 l_1^2}{I_G} & -\frac{c_2}{m_t} + \frac{c_2 l_1 l_2}{I_G} \\ -\frac{k_1}{m_t} + \frac{k_1 l_1 l_2}{I_G} & -\frac{k_2}{m_t} - \frac{k_2 l_2^2}{I_G} & -\frac{c_1}{m_t} + \frac{c_1 l_1 l_2}{I_G} & -\frac{c_2}{m_t} - \frac{c_2 l_2^2}{I_G} \end{bmatrix} \begin{bmatrix} h_1 \\ h_2 \\ h_3 \\ h_4 \end{bmatrix} \tag{5.8}$$

5.2 SS Control Laws for a 2DOF System

Based on the control law introduced in Section 3.2.2., the SS control law for the 2DOF system can be expressed in terms of the stiffness of the individual masses. Each SDOF system in the 2DOF system is independently controlled by switching the stiffness based on the respective position and velocity feedback. The SS control law focuses on the dissipating the energy from the individual masses.

$$\begin{aligned} k_1(t) &= \begin{cases} k_{1high} & \text{for } x_1(t)\dot{x}_1(t) \geq 0 \\ k_{1low} & \text{for } x_1(t)\dot{x}_1(t) < 0 \end{cases} \\ k_2(t) &= \begin{cases} k_{1high} & \text{for } x_2(t)\dot{x}_2(t) \geq 0 \\ k_{1low} & \text{for } x_2(t)\dot{x}_2(t) < 0 \end{cases} \end{aligned} \tag{5.9}$$

The delayed SS control strategy presented Section 3.2.2. yields the following control law for 2DOF systems. The HP delayed control is given in equation by

$$\begin{aligned} k_1(t+\tau_c) &= \begin{cases} k_{1high} & \text{for } x_1(t)\dot{x}_1(t) \geq 0 \\ k_{1low} & \text{for } x_1(t)\dot{x}_1(t) < 0 \end{cases} \\ k_2(t+\tau_c) &= \begin{cases} k_{2high} & \text{for } x_2(t)\dot{x}_2(t) \geq 0 \\ k_{2low} & \text{for } x_2(t)\dot{x}_2(t) < 0 \end{cases} \end{aligned} \tag{5.10}$$

where the 2DOF HP intentional delay is given as

$$\tau_c = n\frac{1}{2}T - \tau_d, \quad \tau_c \geq 0 \tag{5.11}$$

The natural period T is determined by averaging the two natural periods.

$$T = \frac{T_1 + T_2}{2} \tag{5.12}$$

where T_1 and T_2 are the natural periods of the system. The natural periods can be determined using modal analysis on the system. The stiffness of the 2DOF system ($k1$ and k_2) is calculated from the averaged respective k_{low} and k_{high} values.

The 2DOF QP delayed control is given in equation by

$$\begin{aligned} k_1(t+\tau_c) &= \begin{cases} k_{1low} & \text{for } x_1(t)\dot{x}_1(t) \geq 0 \\ k_{1high} & \text{for } x_1(t)\dot{x}_1(t) < 0 \end{cases} \\ k_2(t+\tau_c) &= \begin{cases} k_{2low} & \text{for } x_2(t)\dot{x}_2(t) \geq 0 \\ k_{2high} & \text{for } x_2(t)\dot{x}_2(t) < 0 \end{cases} \end{aligned} \tag{5.13}$$

where the QP intentional delay is given as

$$\tau_c = h\frac{1}{4}T - \tau_d, \quad \tau_c \geq 0 \tag{5.14}$$

The natural period T is determined by equation (5.12).

5.3 Simulations of SS Control for a 2DOF System

5.3.1 SS Control of a Linear 2DOF System

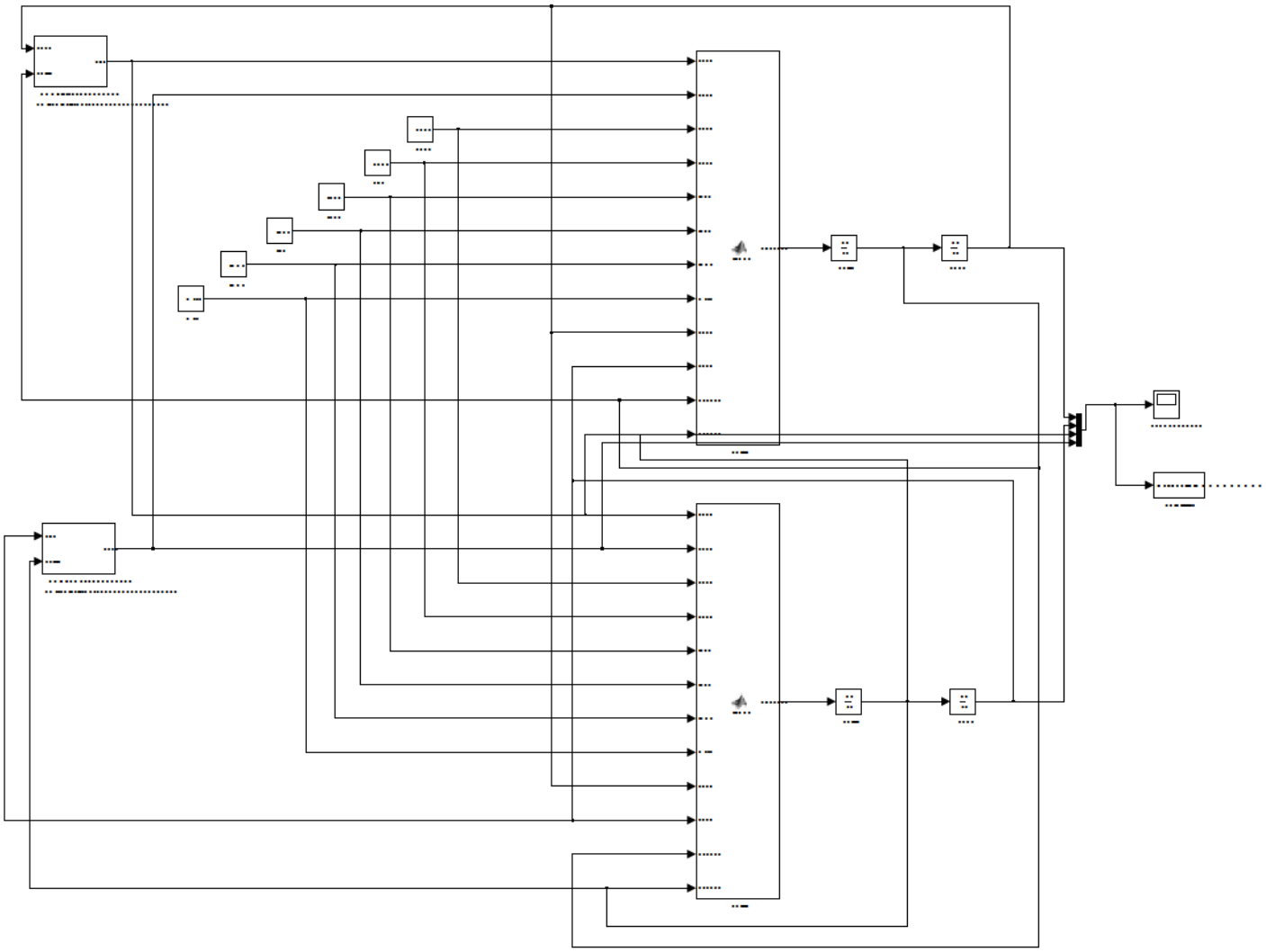

Figure 5.3 Simulink block diagram of linear model

A series of simulations were conducted through Matlab Simulink based on the linear model presented in equation (5.5). An initial displacement of 6 mm was input into the second mass. The rest of the initial conditions were zero. For the free response, an average stiffness value was used ($k_1 = k_2 = 1500$ N/m). The system mass, stiffness, and damping are symmetrical. The simulation parameters are given in Table 5.1

Table 5.1 Simulation parameters for symmetrical linear model

Parameters	Values
k_{1high}	2000 [N/m]
k_{1low}	1000 [N/m]
k_{2high}	2000 [N/m]
k_{2low}	1000 [N/m]
c_1	0 [kg/s]
c_2	0 [kg/s]
m_1	0.130 [kg]
m_2	0.130 [kg]
m_b	0.207 [kg]
l_t	0.446 [m]

The free response of this system is shown in Figure 5.4. It is evident through each mass's displacement appears like beat, which indicates that there are two close frequencies present in the responses [2]. Using modal analysis, the natural frequencies of the system were determined to be 11.28 Hz (first mode) and 12.76 Hz (second mode). The modes of vibration are shown in Figure 5.5. Unless the system is vibrating at its natural modes, it difficult to pin point the frequency of each mass, as it is composed of more than a single frequency. Herein lies a problem for using the delayed SS control strategy. The vibration profile of each mass depends on the initial conditions and may vary [53].

The SS control simulation results are shown in Figure 5.6. In the ideal case, the SS strategy is very effective at vibration suppression for 2DOF systems.

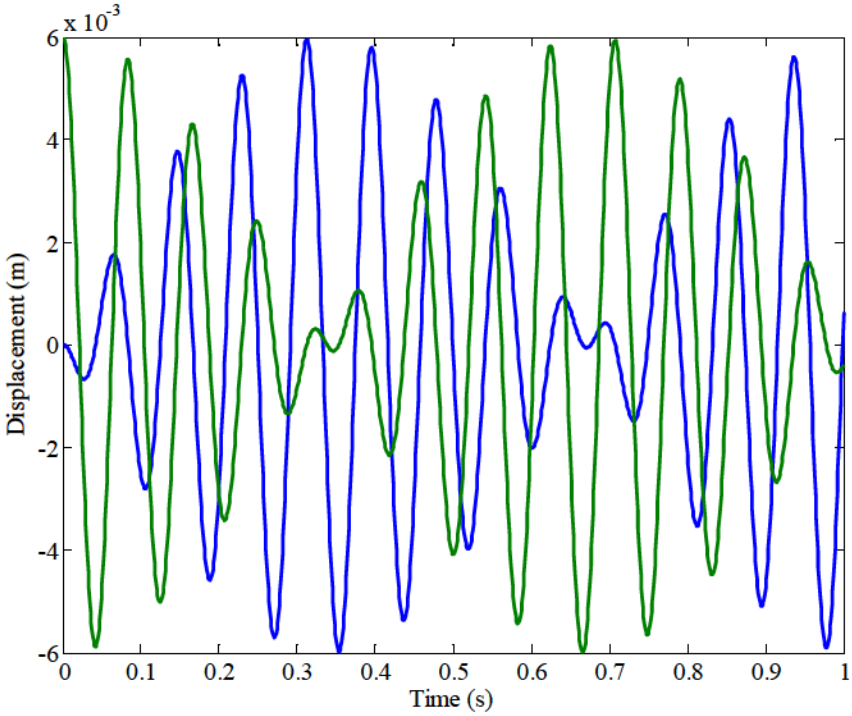

Figure 5.4 Free response of 2DOF system for mass 1 (blue) and mass 2 (green)

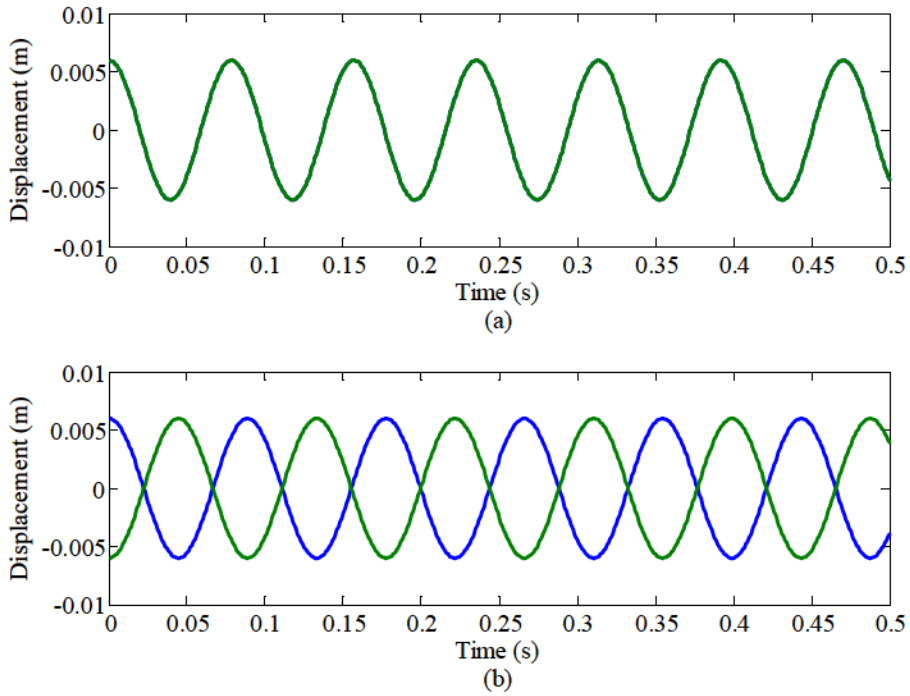

Figure 5.5 Free response of 2DOF system for mass 1 (blue) and mass 2 (green) at (a) the first mode and (b) the second mode

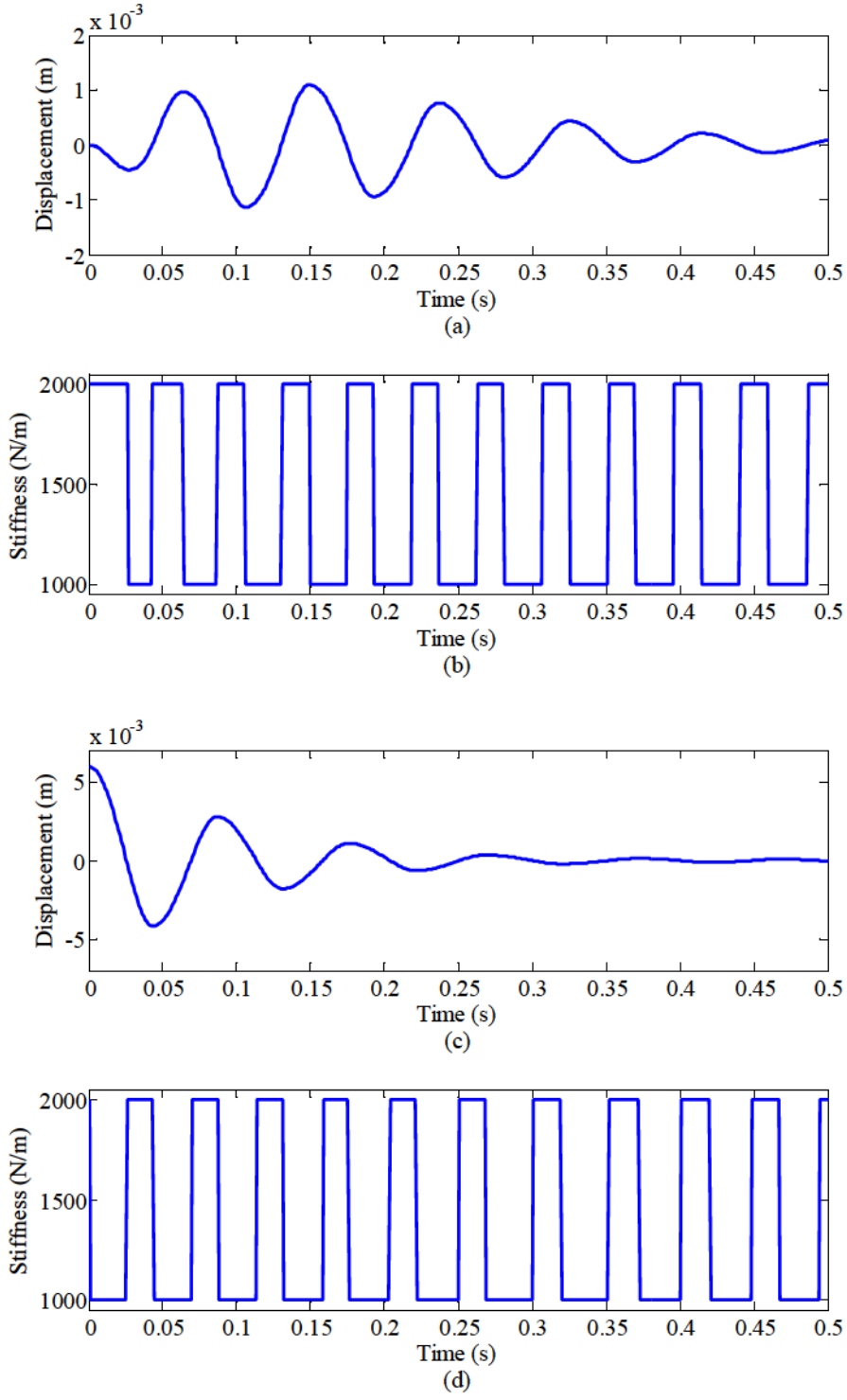

Figure 5.6 Simulation of direct SS control of a linear 2DOF system (a) m_1 displacement response, (b) k_1 stiffness switching, (c) m_2 displacement response, and (d) k_2 stiffness switching

5.3.2 SS Control of a Linear 2DOF System with Time Delay

A series of simulations were conducted to examine the effects of inherent time delays and the efficacy of the delayed control strategies. The simulation parameters are given in Table 5.1 and are almost identical to the simulation procedure in Section 5.3.1 with one exception. A time delay was added to the system states entering the controller. The time delay was 12 ms based on the characterization in Section 2.7.

For the first set of simulations, the direct SS control law defined by equation (5.9) was applied. The simulation results are shown in Figure 5.7. The simulations show that the system is unstable due to the inappropriate stiffness switching.

The delayed control strategies presented in Section 3.2 may be used to overcome the instabilities due to time delay. For the delayed SS control of a 2DOF system, complications arise when predicting the natural period in order to calculate τ_c. In the case where the system is symmetrical (e.g. identical mass, stiffness, and damping), the natural periods are very close as shown in Figure 5.4 and Figure 5.5. Therefore, the average of the two natural periods is proposed to determine τ_c.

For the second set of simulations, the first set is repeated using the delayed SS strategy. In this case, the QP delayed control law was employed as it yielded the minimum τ_c. The average stiffness of each system ($k_1(k_{1high}, k_{1low})$ and $k_2(k_{2high}, k_{2low})$) was used for modal analysis to determine the natural frequencies. The two natural frequencies of the system were determined to be ω_1 = 11.28 Hz and ω_2 = 12.76 Hz and the average natural period was calculated to be 83 ms (12.02 Hz). The QP intentional delay was calculated to be approximately τ_c = 9 ms. The simulation results are shown in Figure 5.8. It is observed that the delayed SS control strategy is effective for the vibration suppression of a linear symmetrical 2DOF system with time delay.

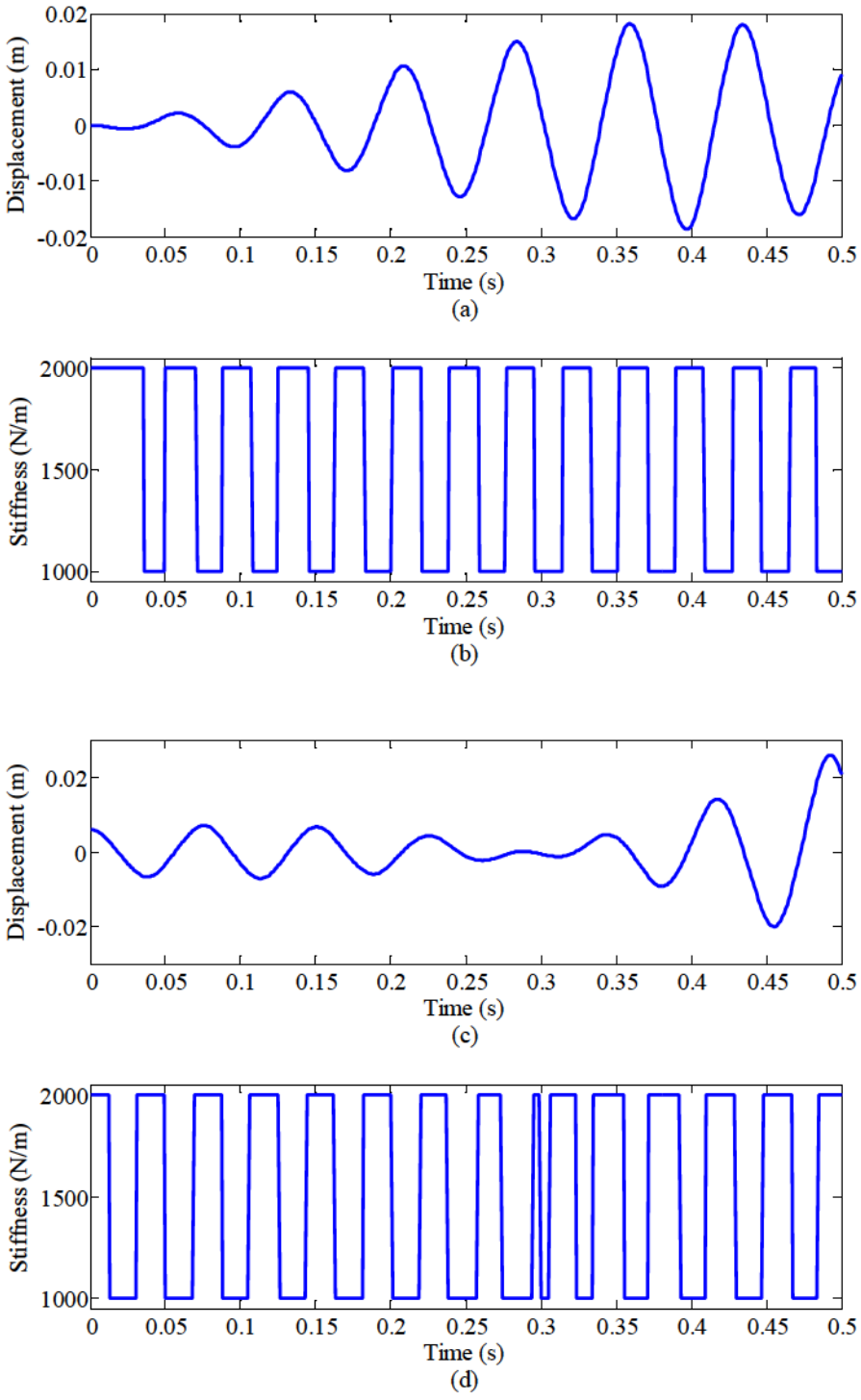

Figure 5.7 Simulation of direct SS control of a linear 2DOF system with 12 ms time delay (a) m_1 displacement response, (b) k_1 stiffness switching, (c) m_2 displacement response, and (d) k_2 stiffness switching

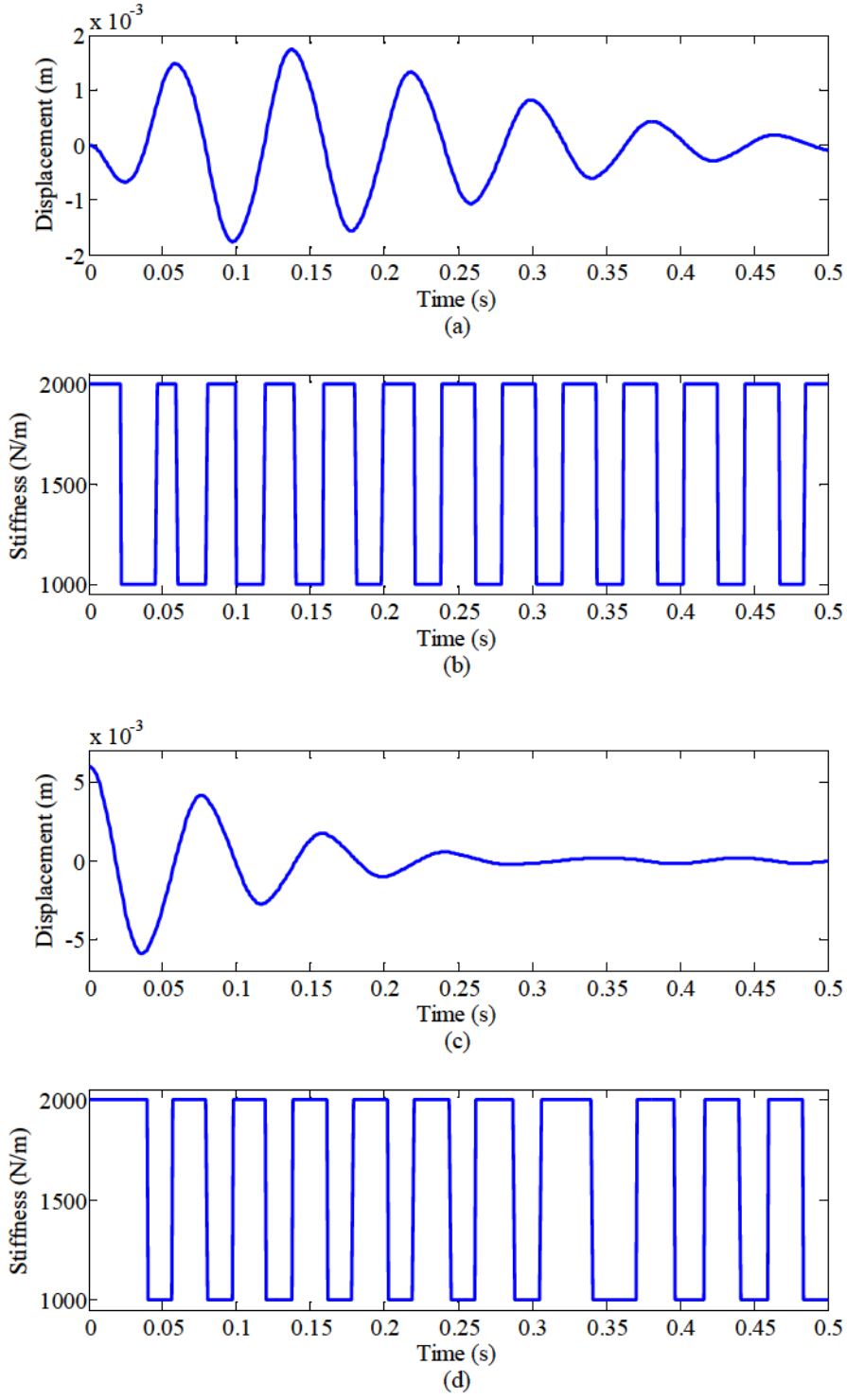

Figure 5.8 Simulation of QP delayed inverted SS control of a linear 2DOF system with 12 ms time delay (a) m_1 displacement response, (b) k_1 stiffness switching, (c) m_2 displacement response, and (d) k_2 stiffness switching

5.3.3 SS Control of a Non-Linear 2DOF System

A simulation was conducted based on the non-linear dynamic force and stiffness models characterized in Chapter 2. The direct SS control in equation (5.9) was used. An initial displacement of 6 mm was input into the second mass and the rest of the initial conditions were zero. The dynamics of the EMs are neglected. The simulation setup and parameters are listed in Table 5.2 and the Simulink block diagram is shown in Figure 5.9. The simulation results are shown in Figure 5.10. It is observed that the SS control is effective on 2DOF systems regardless of the system non-linearity.

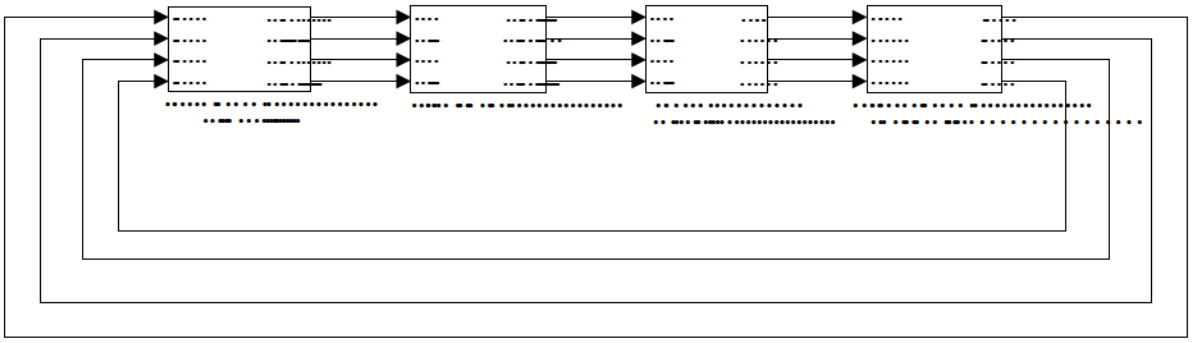

Figure 5.9 Simulink block diagram for non-linear model

Table 5.2 Simulation parameters for the non-linear model

Parameters	Values
EM set A for both actuators	
Medium MB tension for both MB	
D	80 [mm]
V_{1high}	20 [V]
V_{1low}	-20 [V]
V_{2high}	20 [V]
V_{2low}	-20 [V]
c_1, c_2	0 [kg/s]
m_1, m_2	0.130 [kg]
m_b	0.207 [kg]
l_t	0.446 [m]

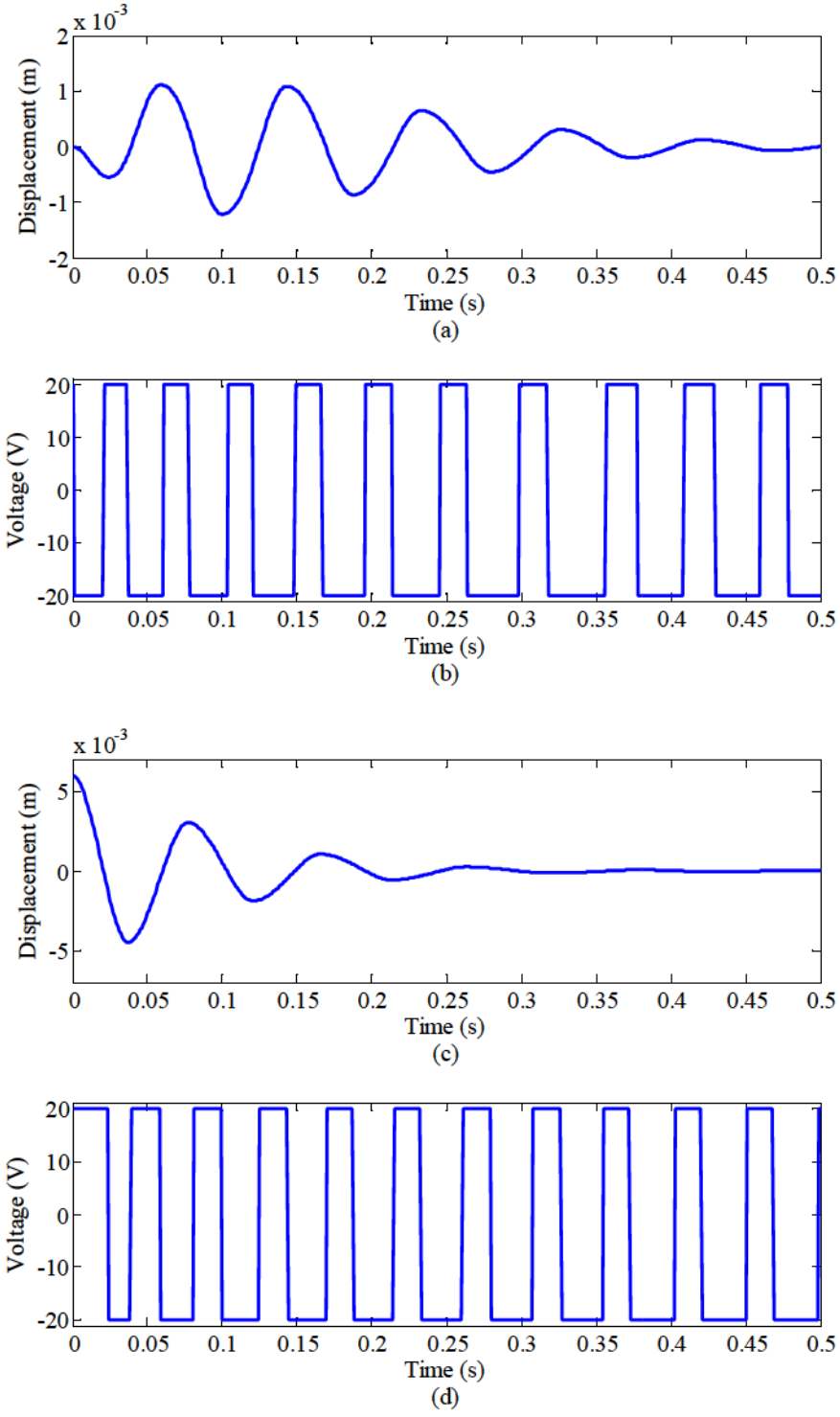

Figure 5.10 Simulation of direct SS control of a non-linear 2DOF system (a) m_1 displacement response, (b) k_1 stiffness switching, (c) m_2 displacement response, and (d) k_2 stiffness switching

5.3.4 SS Control of a Non-Linear 2DOF System with Time Delay

A series of simulations were conducted to examine the effects of inherent time delays and the efficacy of the delayed control strategy on the non-linear symmetrical 2DOF system. The simulation parameters are given in Table 5.2. An inherent time delay of 12 ms was added to the system states entering the controller. A 6 mm initial displacement was input into m_2 and the remaining initial conditions were set to 0.

For the first set of simulations, the direct SS control law defined by equation (5.9) was applied to the non-linear system. Similar to the direct SS control of a linear system with time delay in Section 5.3.2, the inherent time delay causes parametric excitation. To overcome this issue, the delayed SS control strategies can be used.

The second set of simulations investigates the delayed SS control for non-linear symmetrical 2DOF systems with time delay. For this configuration, the QP delayed control strategy was implemented as it minimizes τ_c. First, the QP intentional delay was determined. The analytical high and low stiffness values of the individual SDOF systems were calculated from equation (2.8) in Section 2.5.1. The min and max current used in these equations are -1.5 A and 1.5 A corresponding to -20 V and 20 V. The stiffness values for each SDOF system were determined to be $k_{1low} = k_{2low} = 812.20$ N/m and $k_{1high} = k_{2high} = 2007.96$ N/m. The mean stiffness value for each SDOF system was calculated to be $k_{mean} = k_1 = k_2 = 1410.08$ N/m. The natural frequencies of the system were determined from the modal analysis of equation to be $\omega_1 = 10.93$ Hz and $\omega_2 = 12.37$ Hz. As these frequencies are relatively close, the average natural frequency and period was found to be approximately 11.65 Hz and 86 ms, respectively. The QP intentional delay was calculated to be roughly 10 ms.

The QP delayed control simulation results are shown in Figure 5.11. The vibrations of both masses are effectively suppressed. It is shown that the delayed SS control strategy is viable for non-linear symmetrical 2DOF systems.

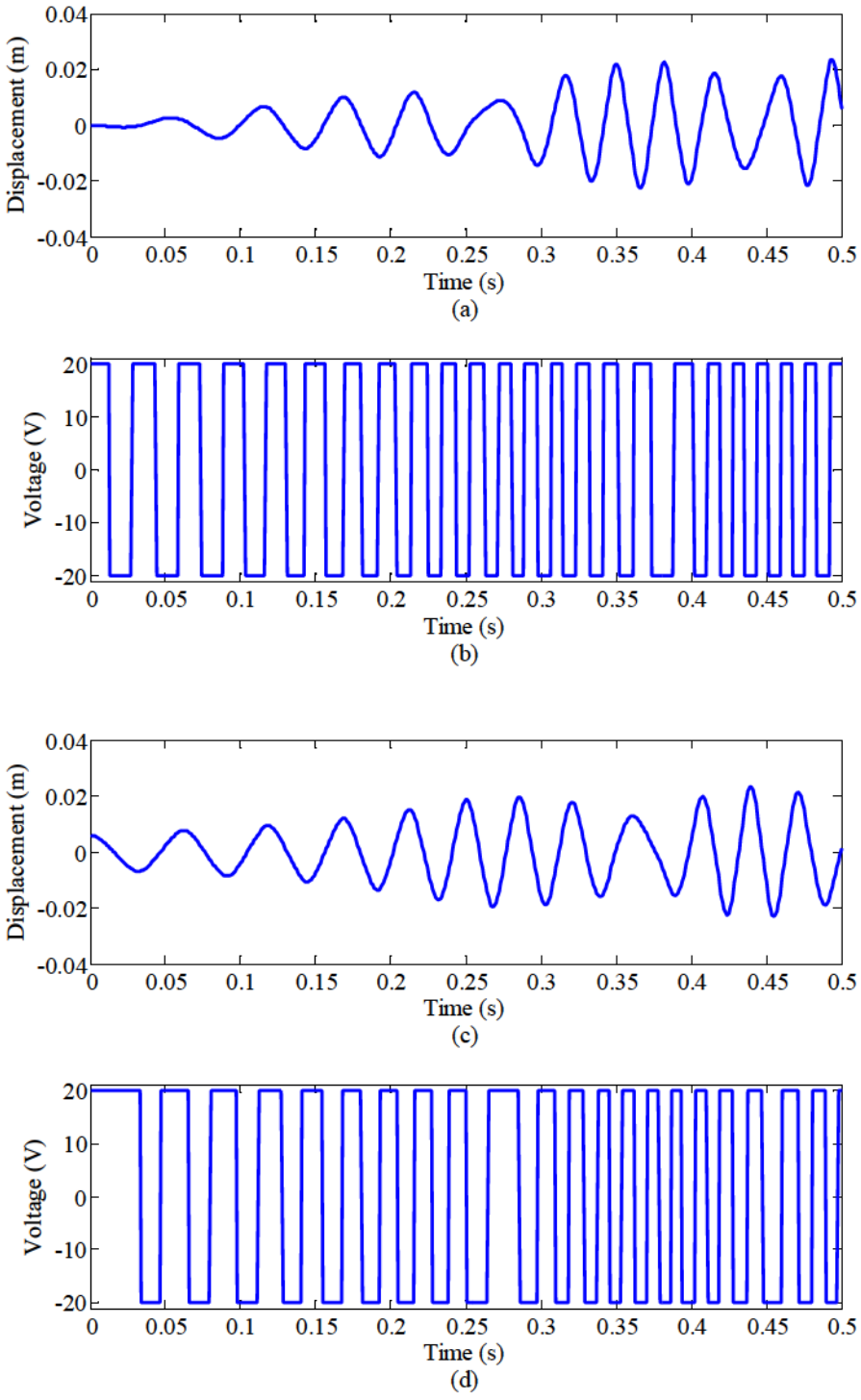

Figure 5.11 Simulation of direct SS control of a non-linear 2DOF system with 12 ms time delay (a) m_1 displacement response, (b) k_1 stiffness switching, (c) m_2 displacement response, and (d) k_2 stiffness switching

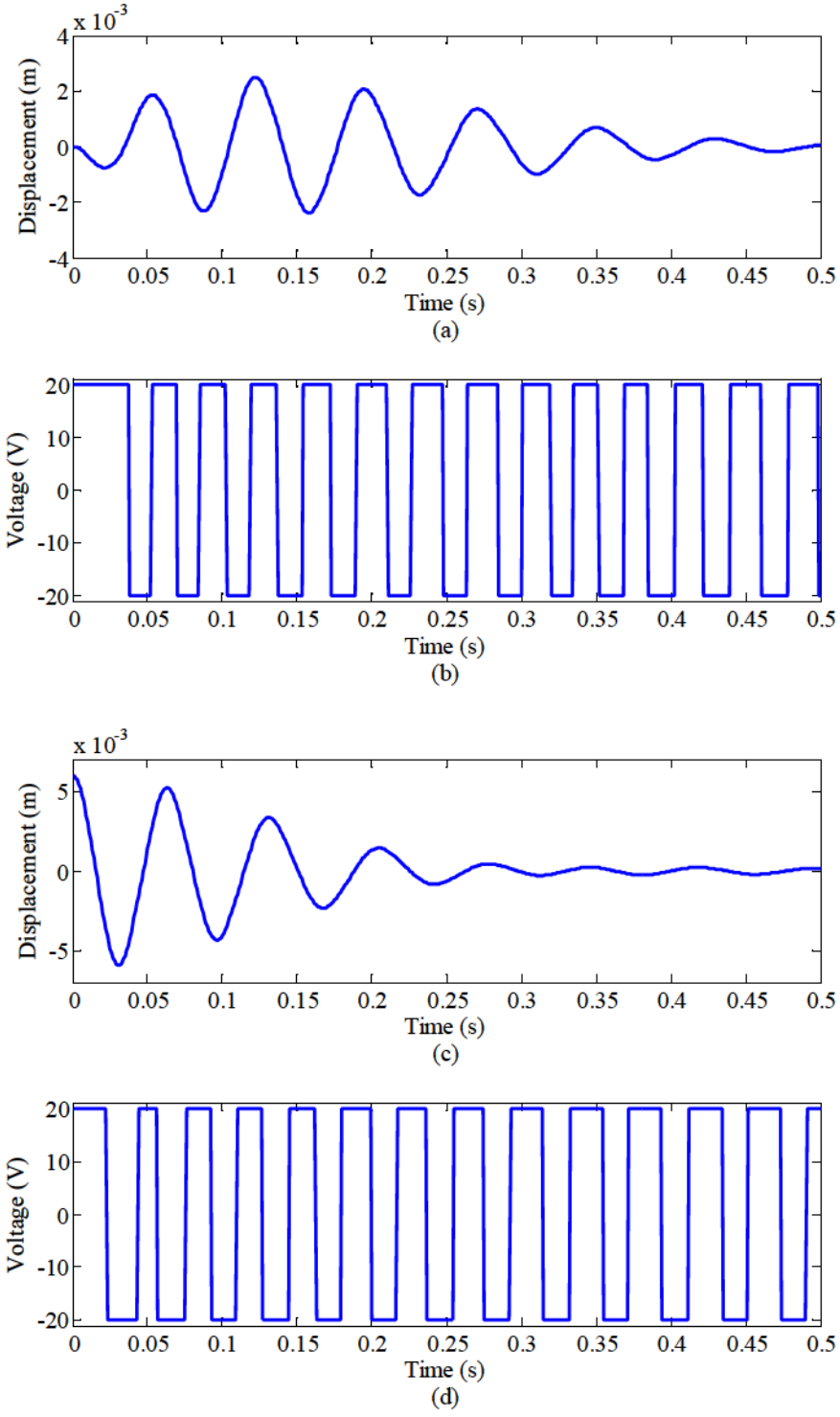

Figure 5.12 Simulation of QP delayed inverted SS control of a non-linear 2DOF system with 12 ms time delay (a) m_1 displacement response, (b) k_1 stiffness switching, (c) m_2 displacement response, and (d) k_2 stiffness switching

5.3.5 Delayed SS Control of an Asymmetrical 2DOF Systems

A series of simulations were conducted to investigate the delayed SS control strategies for an asymmetrical 2DOF system (e.g. different mass, stiffness, or damping properties). An asymmetrical system is a more generalized and a more realistic representation of real-world applications. Two sets of simulations are conducted. The first set is based on the linear 2DOF system. The second set is based on the non-linear 2DOF system.

For the first simulation, the system configuration parameters are listed in Table 5.3. The stiffness k_1 and k_2 values used in the modal system equations are calculated based on the average k_{low} and k_{high} values. The stiffness k_1 and k_2 were calculated to be 1500 N/m and 1000 N/m respectively. Using modal analysis, the natural frequencies were found to be ω_1 = 7.75 Hz and ω_2 = 11.89 Hz. The system asymmetry causes a larger variation in the natural frequencies. It is expected that the large variation in the natural frequencies will reduce the effectiveness of the delayed SS control. The average of the natural frequencies (9.82 Hz) was used to determine the average natural period (102 ms). The QP intentional delay was calculated to be 13 ms. For comparison, Figure 5.13 shows the direct SS control for the linear asymmetrical system without delay. Figure 5.14 shows the delayed QP inverted SS control for the system with delay. It is confirmed that the vibration suppression is poor compared to the system without time delay. For m_1, the vibration appears to be amplified at certain times. Overall, however, the vibrations are suppressed.

Table 5.3 Simulation parameters for the asymmetrical linear model

Parameters	Values
k_{1high}	2000 [N/m]
k_{1low}	1000 [N/m]
k_{2high}	1500 [N/m]
k_{2low}	500 [N/m]
c_1, c_2	0 [kg/s]
m_1	0.130 [kg]
m_2	0.260 [kg]
m_b	0.207 [kg]
l_t	0.446 [m]

Table 5.4 Simulation parameters for the asymmetrical non-linear model

Parameters	Values
EM set A for both systems	
Medium MB tension for system 1 Low MB tension for system 2	
D	80 [mm]
V_{1high}	20 [V]
V_{1low}	-20 [V]
V_{2high}	20 [V]
V_{2low}	-20 [V]
c_1, c_2	0 [kg/s]
m_1	0.130 [kg]
m_2	0.260 [kg]
m_b	0.207 [kg]
l_t	0.446 [m]

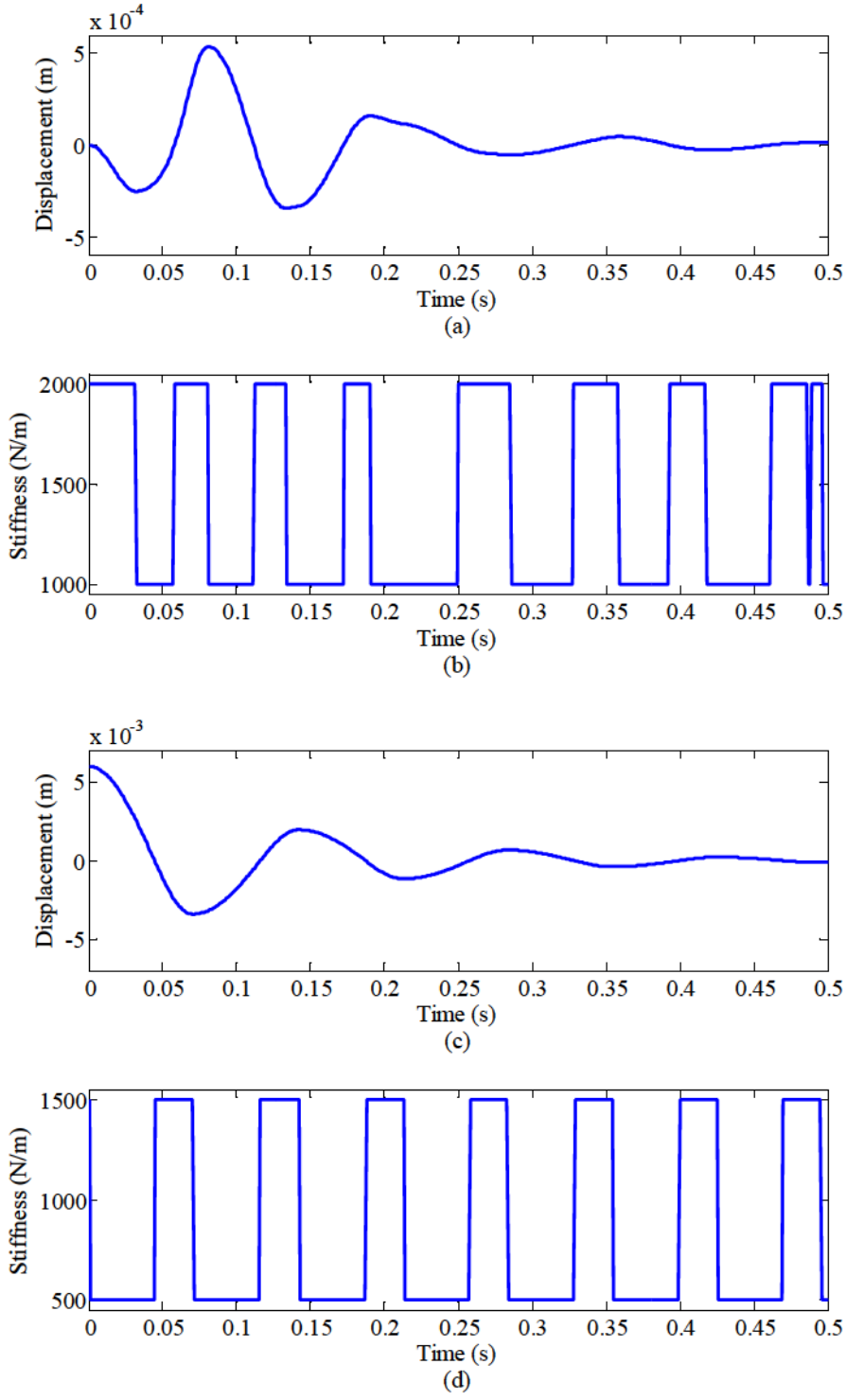

Figure 5.13 Simulation of direct SS control of a linear asymmetrical 2DOF system (a) m_1 displacement response, (b) k_1 stiffness switching, (c) m_2 displacement response, and (d) k_2 stiffness switching

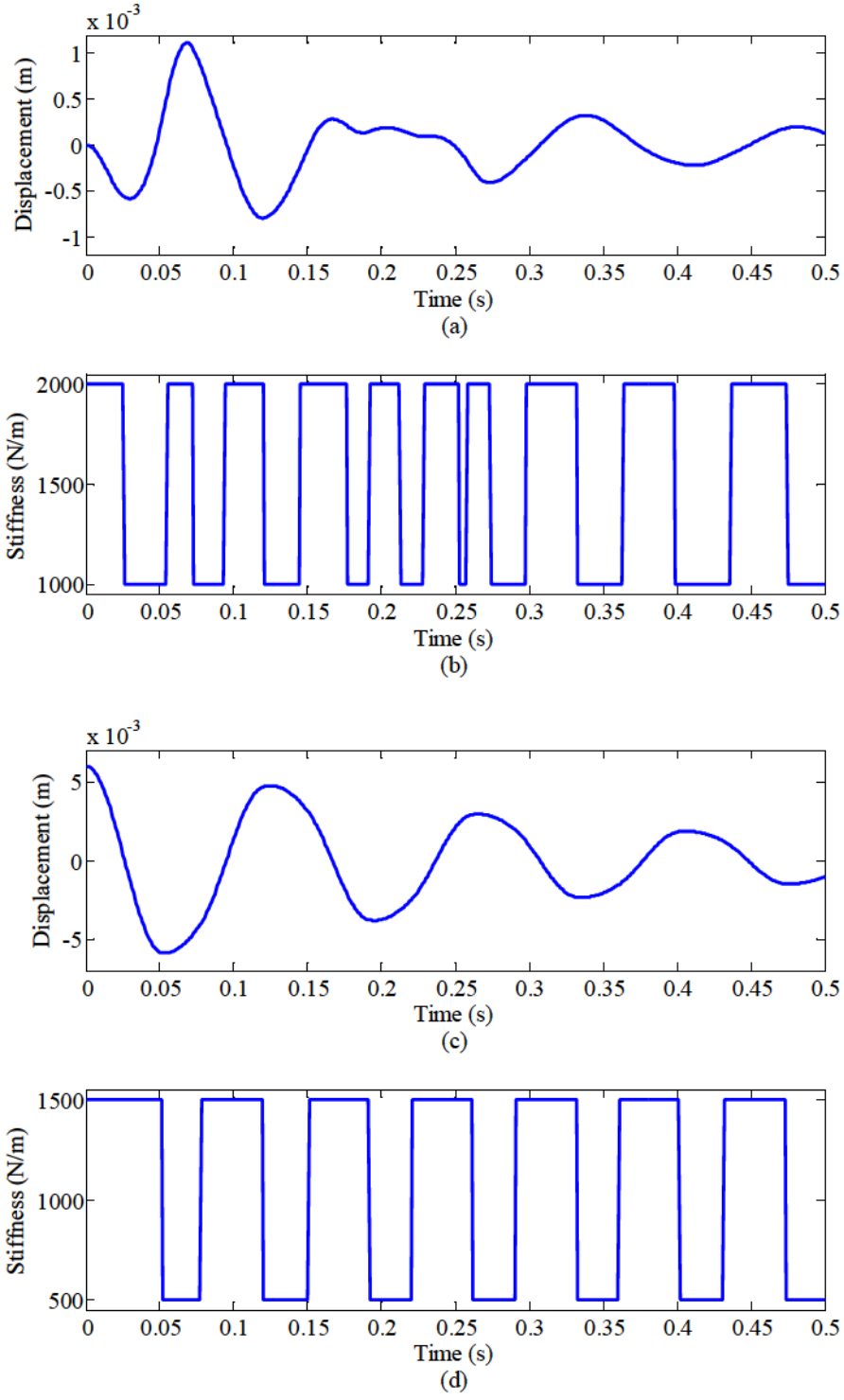

Figure 5.14 Simulation of QP delayed inverted SS control of a linear asymmetrical 2DOF system with 12 ms time delay (a) m_1 displacement response, (b) k_1 stiffness switching, (c) m_2 displacement response, and (d) k_2 stiffness switching

For the second simulation, the system configuration parameters are listed in Table 5.4. The QP delayed control strategy was selected as it minimizes the intentional delay value. First, the QP intentional delay was determined. The analytical high and low stiffness of the individual SDOF systems were calculated from equation (2.8) in Section 2.5.1. The min and max current used in these equations are -1.5 A and 1.5 A corresponding to -20 V and 20 V. The average of the high and low stiffness states were used in the calculation of the natural frequencies of the system. It can be seen that the two natural frequencies are not close (ω_1 = 6.48 Hz and ω_2 = 11.52 Hz). The average natural period was calculated to 111 ms and the QP intentional delay was calculated to be 16 ms. The calculated values are shown in Table 5.5.

Table 5.5 Calculating QP Intentional Delay

Stiffness States (N/m)	**Average Stiffness (N/m)**	**Modal Analysis (Hz)**	**Average Frequency/Period**	**QP Delay (ms)**
k_{1low} = 811.60	k_1 = 1410.20	ω_1 = 6.48	ω_{avg} = 9.00 Hz T_{avg} = 111 ms	16
k_{1high} = 2008.79				
k_{2low} = 79.67	k_2 = 678.01	ω_2 = 11.52		
k_{2high} = 1276.34				

For reference, Figure 5.15 shows the simulation results of the direct control of a non-linear asymmetrical 2DOF system without time delay. Figure 5.16 shows the simulations results of the QP delayed inverted SS control strategy for the non-linear asymmetrical 2DOF with time delay. System 2 vibrates at a lower frequency than system 1. This is expected as system 2 has a low MB tension and higher system mass. For the control without time delay, higher frequency means more stiffness switching and, thus, more amplitude attenuation. For the control with time delay, a higher frequency means larger errors and, thus, less effective control. The delayed SS control strategy is able to reduce the overall vibration of the system, however not very effectively.

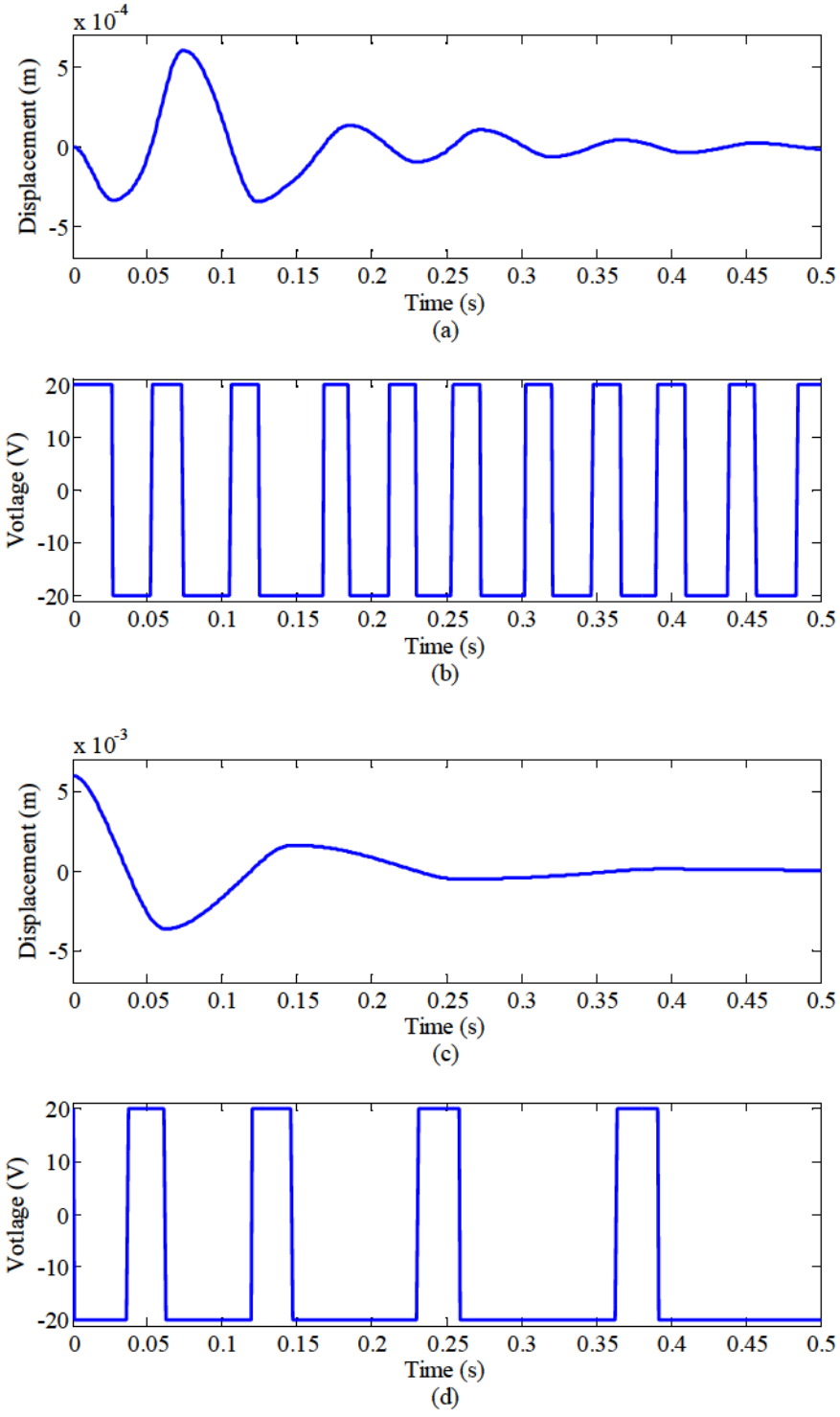

Figure 5.15 Simulation of direct SS control of a non-linear asymmetrical 2DOF system (a) m_1 displacement response, (b) k_1 stiffness switching, (c) m_2 displacement response, and (d) k_2 stiffness switching

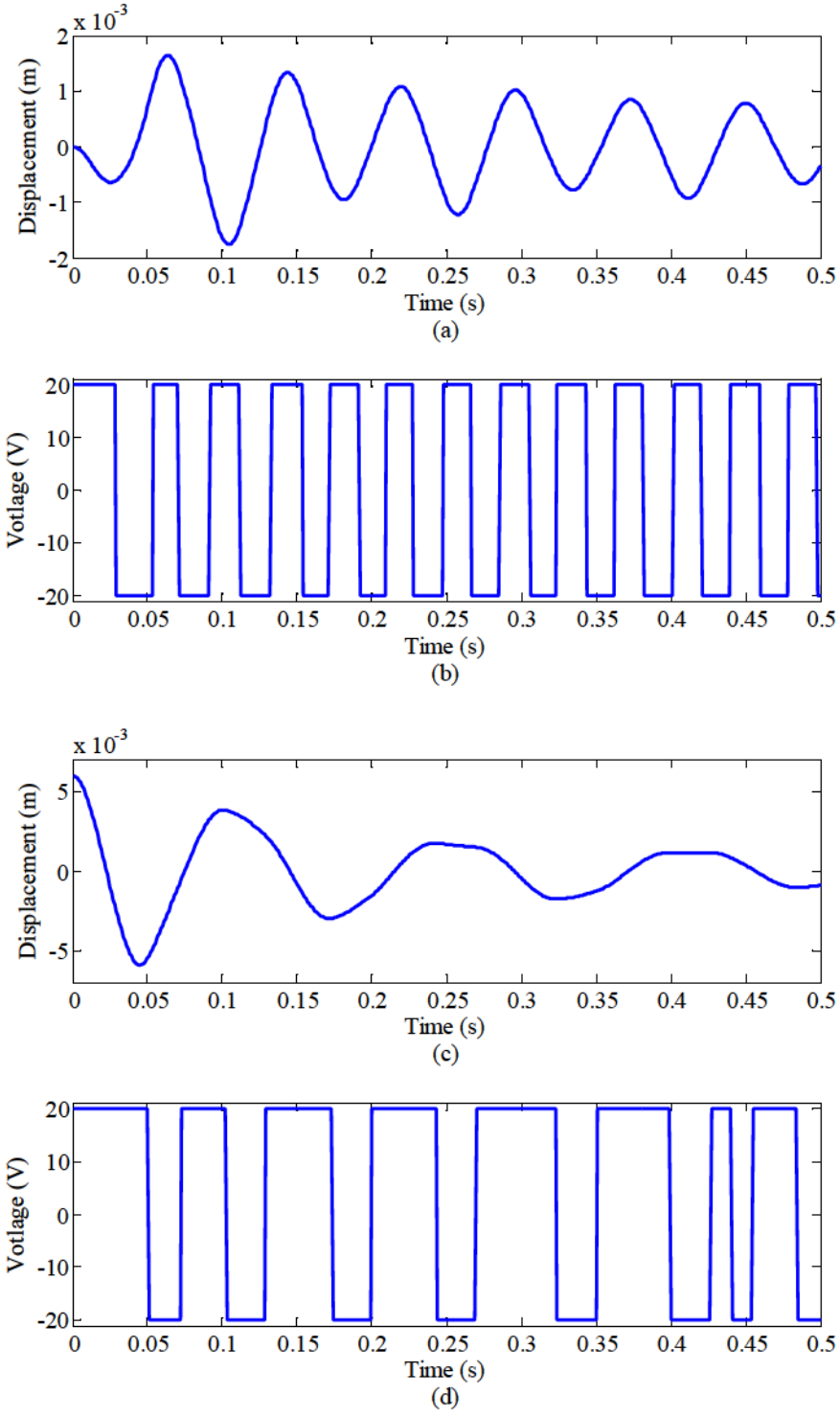

Figure 5.16 Simulation of QP delayed inverted SS control of a non-linear asymmetrical 2DOF system with 12 ms time delay (a) m_1 displacement response, (b) k_1 stiffness switching, (c) m_2 displacement response, and (d) k_2 stiffness switching

5.4 Conclusions

In this chapter, the SS control law was applied to a 2DOF system. The 2DOF system is made up of two SDOF systems (identical to the system presented in Chapter 2) coupled together by a beam. First, the 2DOF system schematic and FBD were presented and the equations of motion were derived for the modal analysis, in terms of the coordinates for the individual masses, and in state space form. Second, the SS control law and delayed SS control law was reintroduced for the 2DOF system. Essentially, each mass is controlled individually by the SS logic.

In addition, simulations were conducted based on the derived models. Simulations demonstrated that the SS control strategy was effective at reducing vibrations of both linear and non-linear 2DOF system. However, with the presence of a significant time delay, both linear and non-linear models showed instability. The delayed SS control strategies were considered for overcoming the inherent time delays in 2DOF systems. However, the challenge with this strategy lies in determining the intentional delay. It was found that for symmetrical systems (identical mass, stiffness, and damping characteristics), the system's natural frequencies were very close and the average period could be used for determining the intentional delays. Simulations of the delayed SS control on the linear and non-linear systems showed effective vibration suppression. The performance of the non-linear system was slightly weaker due to the variation in period as a function of the vibration amplitudes. Additionally, asymmetrical systems were considered for the delayed SS control. Simulations showed that a larger variation in the two natural frequencies of the system made the delayed SS control considerably less effective.

Theoretical analysis for the stability, damping, and mechanism of this system is required. Experimental work is also required to fully verify SS control for 2DOF systems. These areas are beyond the scope of this thesis. However, this chapter has presented the preliminary ground work for future research.

Chapter 6 – Conclusions & Future Works

6.1 Summary

In this thesis, the SS control strategy was investigated. First, the fundamental concepts of vibration control and the SS strategy were introduced. A brief literature survey of the SS control research and development was conducted.

Second, an SDOF experimental apparatus with a SS spring (electromagnetic spring) was constructed to test the SS strategy. The complete system dynamics and parameters of this apparatus were characterized through experimental identification. A non-linear analytical model for the dynamic forces and stiffness of the system was established. It was found that the combined stiffness could be modeled as cubic polynomials for different configurations of the MB tension, EM gap distance, and EM sets. For simplification, a linear model was also presented for small vibrations. The system damping and natural frequencies were identified for different configurations. The EM inductance and back EMF were also identified and investigated.

Third, the SS control strategy was studied in detail via theory and computer simulations. The simulations revealed the control mechanism of the SS strategy. It was found that vibration suppression was achieved through the dissipation of potential energy via stiffness reduction at the peaks of the mass displacements. The energy dissipation was found to be directly proportional to the stiffness variation. It was also found that vibration amplification was achieved through the inverted application of the SS control law. A mathematical relationship between the stiffness ratio and amplitude suppression was established through energy analysis. Additionally, simulations were conducted on the SS control with the effects of inherent time delays. The results show that the system is stable if the inherent delay was equivalent to a multiple of half of

the period and unstable if the delay was equivalent to an odd multiple of a quarter of the period. A novel method was presented to improve the performance and avoid instability due to time delays. This method involved introducing an intentional delay such that the SS control would be applied correctly either a multiple of half of a period or an odd multiple of one quarter of a period in the future. For the intentional delay making up the QP delayed control, the control was inverted. A series of simulations were conducted to validate and evaluate this method. Additionally, the effects of the EM dynamics were briefly explored. It was found that the EM inductance reduced the effectiveness of the SS control strategy.

Fourth, the SS control strategy was implemented in real-time using the experimental apparatus. The experimental studies validated the observations made with the simulation results. Additionally, it was found that the non-linearity of the system limited the performance of the delayed SS control methods at higher vibration amplitudes. It was also confirmed that the EM inductance limited the amount of current driving the EMs. This effectively limited the stiffness variation and therefore, severely limited the performance. This was the limitation of using EMs as the switchable stiffness spring. Different EM sets, different EM gap distances, and different MB tensions were investigated to further study the SS control. It was found that the stiffness variation was better if the natural period was high, the inductance was low, or the gap EM gap distance was small.

Fifth, preliminary investigations were conducted for the SS control strategy for a 2DOF system. The system equations were derived for the 2DOF system. A series of simulations were conducted based on a linear model. The simulations show that the SS control strategy is effective at suppressing the vibrations of a 2DOF system. Another series of simulations were conducted based on the non-linear dynamics force and stiffness models characterized in Chapter 2. The simulations show the SS control strategy is effective at suppressing the vibrations of a non-linear system. However, with the addition of an inherent system delay, the system was unbounded. The delayed SS control strategy was investigated through simulations. An average period (of the natural periods) was used to determine the intentional delay. The simulation results showed that the delayed SS control strategy is effective for linear and non-linear 2DOF systems that are symmetrical and have natural frequencies that are close together. For asymmetrical systems, the delayed SS control is not as effective, but still viable.

6.2 Main Contributions

The main contributions of this thesis are listed below.

(1) The non-linear and linear analytical dynamic force/stiffness models of the proposed system were characterized.
(2) The control, stability, and mechanism of the SS strategy were validated through simulations.
(3) A delayed SS control strategy to overcome inherent system time delays was developed and verified.
(4) The strengths and limitations of an experimental EM switchable stiffness spring were established.
(5) The delayed SS strategy was validated through real-time implementation.
(6) The SS control for 2DOF systems was validated through simulations. The delayed SS control strategy was validated for symmetrical 2DOF systems through simulations.

6.3 Future Works

Based on the work done in this thesis, the author expresses interest in viable routes for future research. The major areas for future work are listed as below.

(1) The system non-linearity causes the natural period to vary. As a result, the value of the intentional delay will vary as a function of the displacement. To improve the delayed SS control, it is suggested that a technique (fuzzy, adaptive, etc.) be implemented to update the intentional delay either based on the amplitude of vibration or its natural frequency.
(2) Different switchable stiffness springs should be considered (piezoelectric, MRE, low inductance EMs, etc.). Reducing the effect of EM inductance while maintaining the EM strength should increase the control performance dramatically. An optimal actuator should have large stiffness variation, fast switching times, no lag, and low energy cost.
(3) Implementing the SS control on 2DOF or MDOF systems may be beneficial to improve the range of applications for this method. A detailed analysis of the stability, energy dissipation mechanism, and coupling effect will be required. Figure 6.1 and Figure 6.2 show the CAD and photograph of a current 2DOF system constructed for the testing and

development of this work. This system is not ideal for testing due to its weak aluminum frame design. Vibration on such a system causes the frame to act as an additional degree of freedom. Therefore, a new 2DOF system is proposed in Figure 6.3 for the testing and implementation of the SS control strategies.

(4) Implementing the SS control strategy for base excitation. This will allow a more general and systematic way of comparing the performances.

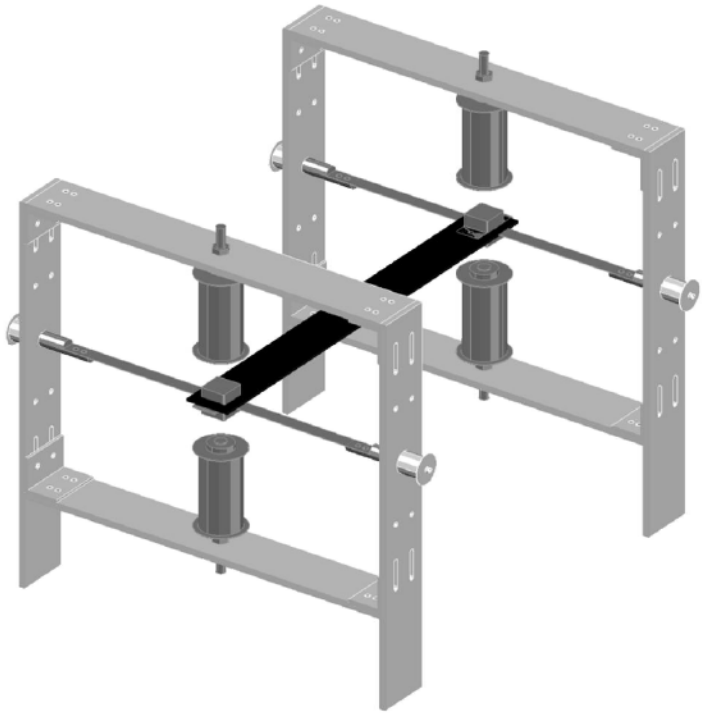

Figure 6.1 CAD of the current 2DOF system

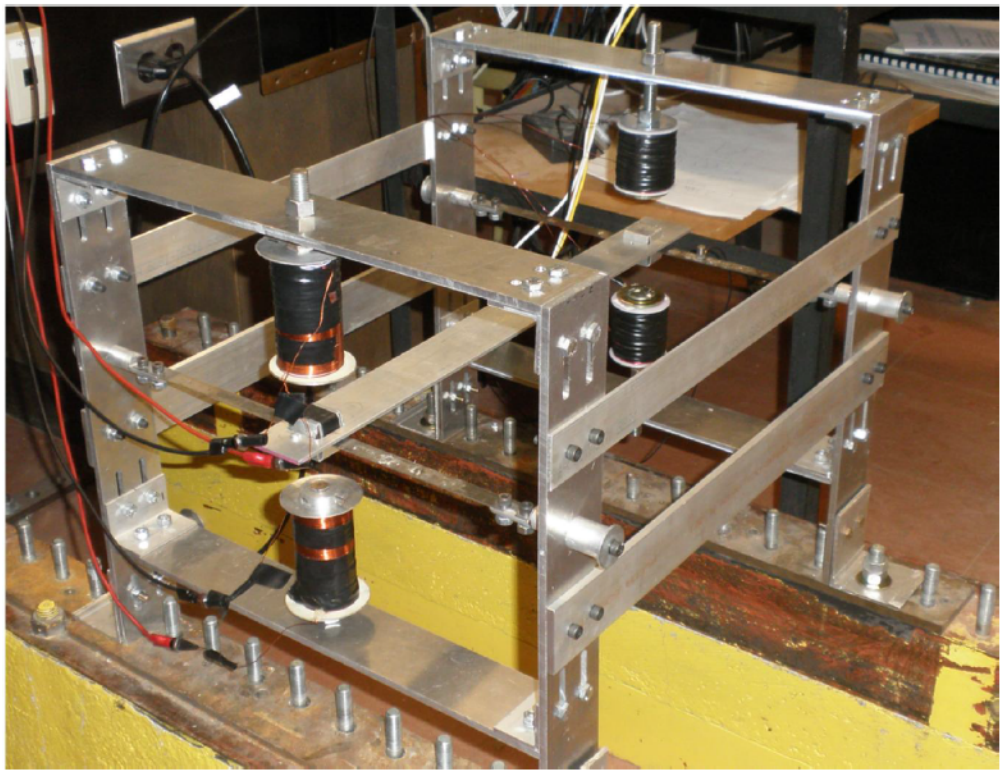

Figure 6.2 Photograph of the current 2DOF system

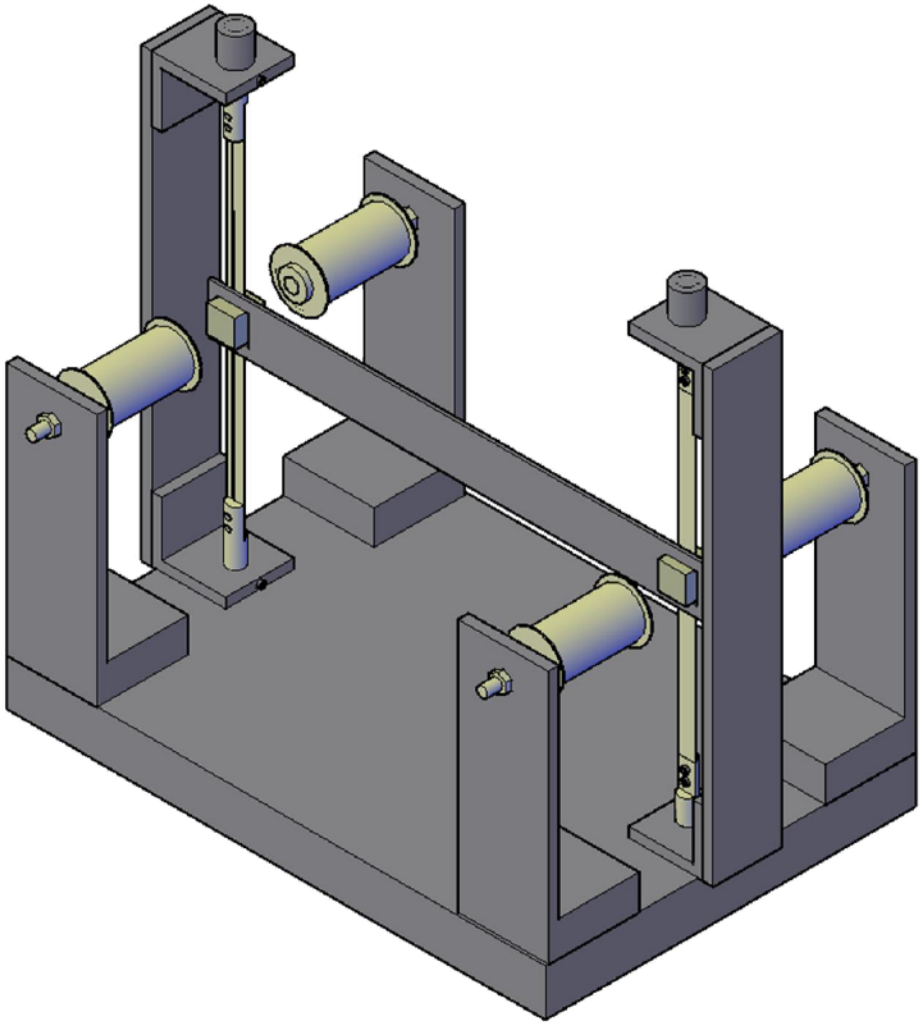

Figure 6.3 CAD of proposed 2DOF system

References

1. De Silva, C. W. (2000). Vibration: fundamentals and practice. Boca Raton, Florida: CRC Press.

2. Inman, D. J. (2008). Engineering Vibration. Upper Saddle River, New Jersey: Prentice-Hall.

3. Kwok, K. C. S., & Samali, B. (1995). Performance of tuned mass dampers under wind loads. *Engineering Structures*, *17*(9), 655-667.

4. Zhou, N. (2009). A Tunable High-Static-Low-Dynamic-Stiffness Isolator and Fuzzy-Neural Network Based Active Control Isolator. M.Sc. Thesis, Lakehead University.

5. Zhou, N., & Liu, K. (2010). A tunable high-static–low-dynamic stiffness vibration isolator. *Journal of Sound and Vibration*, *329*(9), 1254-1273.

6. Carrella, A. (2008). Passive vibration isolators with high-static-low-dynamic-stiffness. Ph.D. Thesis, University of Southampton, 2008.

7. Carrella, A., Brennan, M. J., Waters, T. P., & Shin, K. (2008). On the design of a high-static–low-dynamic stiffness isolator using linear mechanical springs and magnets. *Journal of Sound and Vibration*, *315*(3), 712-720.

8. Kovacic, I., Brennan, M. J., & Waters, T. P. (2008). A study of a nonlinear vibration isolator with a quasi-zero stiffness characteristic. *Journal of Sound and Vibration*, *315*(3), 700-711.

9. Fuller, C. C., Elliott, S., & Nelson, P. A. (1996). Active control of vibration.

10. Coppola, G., & Liu, K. (2010). Control of a unique active vibration isolator with a phase compensation technique and automatic on/off switching. *Journal of Sound and Vibration*, *329*(25), 5233-5248.

11. Coppola, N. (2010). On the control methodologies of a novel active vibration isolator. M.Sc. Thesis, Lakehead University.

12. Ji, X., & Wang, W. (2011). A Neural Fuzzy System for Vibration Control in Flexible Structures. *Intelligent Control & Automation (2153-0653)*, *2*(3).

13. Preumont, A. (1997). *Vibration control of active structures*. Amsterdam: Kluwer.

14. Leitmann, G. (1994). Semiactive control for vibration attenuation. *Journal of Intelligent Material Systems and Structures*, *5*(6), 841-846.

15. Liu, Y., Waters, T. P., & Brennan, M. J. (2005). A comparison of semi-active damping control strategies for vibration isolation of harmonic disturbances. *Journal of Sound and Vibration*, *280*(1), 21-39.

16. Ruddy, C., Ahearne, E., & Byrne, G. (2012). A review of magnetorheological elastomers: properties and applications. *Advanced Manufacturing Science (AMS) Research. http://www. ucd. ie/mecheng/ams/news_items/Cillian% 20Ruddy. pdf Accessed*, *20*.

17. Winthrop, M. F., Baker, W. P., & Cobb, R. G. (2005). A variable stiffness device selection and design tool for lightly damped structures. *Journal of Sound and Vibration*, *287*(4), 667-682.

18. De Vicente, J., Klingenberg, D. J., & Hidalgo-Alvarez, R. (2011). Magnetorheological fluids: a review. *Soft Matter*, *7*(8), 3701-3710.

19. Muhammad, A., Yao, X. L., & Deng, Z. C. (2006). Review of magnetorheological (MR) fluids and its applications in vibration control. *Journal of Marine Science and Application*, *5*(3), 17-29.

20. Song, G., Ma, N., & Li, H. N. (2006). Applications of shape memory alloys in civil structures. *Engineering Structures*, *28*(9), 1266-1274.

21. Clark, W. W. (2000). Vibration control with state-switched piezoelectric materials. *Journal of intelligent material systems and structures*, *11*(4), 263-271.

22. Clark, W. W. (1999, June). Semi-active vibration control with piezoelectric materials as variable-stiffness actuators. In *1999 Symposium on Smart Structures and Materials* (pp. 123-130). International Society for Optics and Photonics.

23. Onoda, J., Endot, T., Tamaoki, H., & Watanabe, N. (1991). Vibration suppression by variable-stiffness members. *AIAA journal*, *29*(6), 977-983.

24. Onoda, J., & Minesugi, K. (1996). Alternative control logic for type-II variable-stiffness system. *AIAA journal*, *34*(1), 207-209.

25. Onoda, J., Sanot, T., & Kamiyama, K. (1992). Active, passive, and semiactive vibration suppression by stiffness variation. *AIAA journal*, *30*(12), 2922-2929.

26. Jabbari, F., & Bobrow, J. E. (2002). Vibration suppression with resettable device. *Journal of Engineering Mechanics*, *128*(9), 916-924.

27. Ramaratnam, A., Jalili, N., & Grier, M. (2003). Piezoelectric vibration suppression of translational flexible beams using switched stiffness. In *Proceedings of 2003 international mechanical engineering congress and exposition (IMECE 2003-41217), Washington DC*.

28. Ramaratnam, A., & Jalili, N. (2006). A switched stiffness approach for structural vibration control: theory and real-time implementation. *Journal of Sound and Vibration*, *291*(1), 258-274.

29. Ramaratnam, A., & Jalili, N. (2006). A switched stiffness approach for structural vibration control: theory and real-time implementation. *Journal of Sound and Vibration*, *291*(1), 258-274.

30. Xian, B., de Queiroz, M. S., Dawson, D. M., & McIntyre, M. L. (2003, December). Output feedback variable structure-like control of nonlinear mechanical systems. In *Decision and Control, 2003. Proceedings. 42nd IEEE Conference on* (Vol. 1, pp. 368-373). IEEE.

31. Guerra, R., Iurian, C., & Acho, L. Velocity Observer for Mechanical Systems. *New Developments in Robotics, Automation and Control*, 111-120.

32. Cunefare, K. A., De Rosa, S., Sadegh, N., & Larson, G. (2000). State-switched absorber for semi-active structural control. *Journal of intelligent material systems and structures*, *11*(4), 300-310.

33. Cunefare, K. A. (2002). State-switched absorber for vibration control of point-excited beams. *Journal of Intelligent Material Systems and Structures*, *13*(2-3), 97-105.

34. Duerr, K., Tesfamariam, S., Wickramasinghe, V., & Grewal, A. (2013). Variable stiffness smart structure systems to mitigate seismic induced building damages. *Earthquake Engineering & Structural Dynamics*, *42*(2), 221-237.

35. Azadi, M., Behzadipour, S., & Faulkner, G. (2011). Performance analysis of a semi-active mount made by a new variable stiffness spring. *Journal of Sound and Vibration*, *330*(12), 2733-2746.

36. Chatterjee, S., & Malas, A. (2012). On the stiffness-switching methods for generating self-excited oscillations in simple mechanical systems. *Journal of Sound and Vibration*, *331*(8), 1742-1758.

37. Krylov, S., Gerson, Y., Nachmias, T., & Keren, U. (2010). Excitation of large-amplitude parametric resonance by the mechanical stiffness modulation of a microstructure. *Journal of Micromechanics and Microengineering*, *20*(1), 015041.

38. Ledezma-Ramirez, D.F. (2008). Shock isolation using switchable stiffness. PhD Thesis, University of Southampton.

39. Ledezma-Ramirez, D. F., Ferguson, N. S., & Brennan, M. J. (2011). Shock isolation using an isolator with switchable stiffness. *Journal of Sound and Vibration*, *330*(5), 868-882.

40. Ledezma-Ramirez, D. F., Ferguson, N. S., & Brennan, M. J. (2012). An experimental switchable stiffness device for shock isolation. *Journal of Sound and Vibration*, *331*(23), 4987-5001.

41. Ledezma-Ramirez, D. F., Ferguson, N. S., & Brennan, M. J. (2008). Energy dissipation using variable stiffness in a single-degree-of-freedom model. In, *EURODYN 2008, 7th European Conference on Structural Dynamics, Southampton, UK,07 - 09 Jul 2008.*

42. Ledezma-Ramirez, D., Ferguson, N., & Ledezma, F. J. E. (2014, January). Validation of a switchable stiffness system for shock isolation. In *Proceedings of Meetings on Acoustics* (Vol. 11, No. 1, p. 065002). Acoustical Society of America.

43. Meriam, J. L., & Kraige, L. G. (2012). *Engineering mechanics: dynamics* (Vol. 2). John Wiley & Sons.

44. Reitz, J. R., Milford, F. J., & Christy, R. W. (2008). *Foundations of electromagnetic theory*. Addison-Wesley Publishing Company.

45. Shigley, J. E., & Mischke, C. R. Mechanical engineering design, 2001.

46. Lin, C. E., & Jou, H. L. (1993). Force model identification for magnetic suspension systems via magnetic field measurement. *Instrumentation and Measurement, IEEE Transactions on*, *42*(3), 767-771.

47. Walters, F. H. (1991). *Sequential simplex optimization: a technique for improving quality and productivity in research, development, and manufacturing*. CRC.

48. Moliton, A. (2007). *Basic electromagnetism and materials*. Springer.

49. Hayt, W. H., & Buck, J. A. (2001). *Engineering electromagnetics* (Vol. 73104639). New York: McGraw-Hill.

50. Khalil, H. K., & Grizzle, J. W. (2002). *Nonlinear systems* (Vol. 3). Upper Saddle River: Prentice hall.

51. Nilsson, J. (1998). *Real-time control systems with delays* (Doctoral dissertation, Ph. D. dissertation, Department of Automatic Control, Lund Institute of Technology, Lund, Sweden).

52. Scherz, P. (2006). *Practical electronics for inventors*. McGraw-Hill, Inc..

53. Ewins, D. J. (1984). *Modal testing: theory and practice* (Vol. 79). Letchworth: Research studies press.

Appendix A

Applying Newton's second law to the body shown in Figure 5.2 yields the following equations of motion:

$$\sum F_x = m_t \ddot{x}_G = -F_{s1} - F_{s2} - F_{d1} - F_{d2} \tag{A1}$$

$$\sum M_G = I_G \ddot{\theta} = F_{s1} l_1 + F_{d1} l_1 - F_{s2} l_2 - F_{d2} l_2 \tag{A2}$$

In the above equations, the small motion assumption is made. It is desirable to transform these coordinates into x_1 and x_2. The following coordinate transformations are used

$$\begin{aligned} x_1 &= x_G - l_1 \sin\theta \\ x_2 &= x_G + l_2 \sin\theta \end{aligned} \tag{A3}$$

Using the small angle approximation $(\sin\theta \doteq \theta)$, the equations are linearized and simplify to

$$\begin{aligned} x_1 &= x_G - l_1\theta \\ x_2 &= x_G + l_2\theta \end{aligned} \tag{A4}$$

Solving equation (A4) for x and θ yields

$$\begin{aligned} x_G &= \frac{l_2}{l_t} x_1 + \frac{l_1}{l_t} x_2 \\ \theta &= -\frac{x_1}{l_t} + \frac{x_2}{l_t} \end{aligned} \tag{A5}$$

Differentiating equation (A5) twice yields

$$\ddot{x}_G = \frac{l_2}{l_t}\ddot{x}_1 + \frac{l_1}{l_t}\ddot{x}_2$$
$$\ddot{\theta} = -\frac{\ddot{x}_1}{l_t} + \frac{\ddot{x}_2}{l_t} \tag{A6}$$

Applying equation (A6) into the governing equations (A1) and (A2) eliminates x and θ and yields

$$\sum F_x = m_t\left(\frac{l_2}{l_t}\ddot{x}_1 + \frac{l_1}{l_t}\ddot{x}_2\right) = -F_{s1} - F_{s2} - F_{d1} - F_{d2} \tag{A7}$$

$$\sum M_G = I_G\left(-\frac{\ddot{x}_1}{l_t} + \frac{\ddot{x}_2}{l_t}\right) = F_{s1}l_1 + F_{d1}l_1 - F_{s2}l_2 - F_{d2}l_2 \tag{A8}$$

To simplify the process, let

$$\beta_1 = -F_{s1} - F_{s2} - F_{d1} - F_{d2}$$
$$\beta_2 = F_{s1}l_1 + F_{d1}l_1 - F_{s2}l_2 - F_{d2}l_2 \tag{A9}$$

Solving equations (A7) and (A8) yields

$$\ddot{x}_1 = \frac{\beta_1}{m_t} - \frac{l_1\beta_2}{I_G} \tag{A10}$$

$$\ddot{x}_2 = \frac{\beta_1}{m_t} - \frac{l_2\beta_2}{I_G} \tag{A11}$$

Reintroducing the equations yields the generalized equations of motion in terms of $\ddot{x}_1$ and $\ddot{x}_2$

$$\ddot{x}_1 = -\left(\frac{F_{s1} + F_{s2} + F_{d1} + F_{d2}}{m_t}\right) - \left(\frac{l_1\left(F_{s1}l_1 + F_{d1}l_1 - F_{s2}l_2 - F_{d2}l_2\right)}{I_G}\right) \tag{A12}$$

$$\ddot{x}_2 = -\left(\frac{F_{s1} + F_{s2} + F_{d1} + F_{d2}}{m_t}\right) + \left(\frac{l_2\left(F_{s1}l_1 + F_{d1}l_1 - F_{s2}l_2 - F_{d2}l_2\right)}{I_G}\right) \tag{A13}$$

Assuming that the damping is viscous and the spring force is linear, the forces are given as

$$\begin{aligned} F_{s1} &= k_1 x_1 \\ F_{s2} &= k_2 x_2 \\ F_{d1} &= c_1 \dot{x}_1 \\ F_{d2} &= c_2 \dot{x}_2 \end{aligned} \tag{A14}$$

Substituting equation (A14) into equations (A12) and (A13) yields the linear solution

$$\ddot{x}_1 = \dot{x}_1\left(-\frac{c_1}{m_t} - \frac{c_1 l_1^2}{I_G}\right) + \dot{x}_2\left(-\frac{c_2}{m_t} + \frac{c_2 l_1 l_2}{I_G}\right) + x_1\left(-\frac{k_1}{m_t} - \frac{k_1 l_1^2}{I_G}\right) + x_2\left(-\frac{k_2}{m_t} + \frac{k_2 l_1 l_2}{I_G}\right) \tag{A15}$$

$$\ddot{x}_2 = \dot{x}_1\left(-\frac{c_1}{m_t} + \frac{c_1 l_1 l_2}{I_G}\right) + \dot{x}_2\left(-\frac{c_2}{m_t} - \frac{c_2 l_2^2}{I_G}\right) + x_1\left(-\frac{k_1}{m_t} + \frac{k_1 l_1 l_2}{I_G}\right) + x_2\left(-\frac{k_2}{m_t} - \frac{k_2 l_2^2}{I_G}\right) \tag{A16}$$

These equations can be re written as

$$\begin{bmatrix} \ddot{x}_1 \\ \ddot{x}_2 \end{bmatrix} = \begin{bmatrix} -\frac{c_1}{m_t} - \frac{c_1 l_1^2}{I_G} & -\frac{c_2}{m_t} + \frac{c_2 l_1 l_2}{I_G} \\ -\frac{c_1}{m_t} + \frac{c_1 l_1 l_2}{I_G} & -\frac{c_2}{m_t} - \frac{c_2 l_2^2}{I_G} \end{bmatrix} \begin{bmatrix} \dot{x}_1 \\ \dot{x}_2 \end{bmatrix} + \begin{bmatrix} -\frac{k_1}{m_t} - \frac{k_1 l_1^2}{I_G} & -\frac{k_2}{m_t} + \frac{k_2 l_1 l_2}{I_G} \\ -\frac{k_1}{m_t} + \frac{k_1 l_1 l_2}{I_G} & -\frac{k_2}{m_t} - \frac{k_2 l_2^2}{I_G} \end{bmatrix} \begin{bmatrix} x_1 \\ x_2 \end{bmatrix} \tag{A17}$$